

**Morphology controlled Rare earth doped CeO₂
with 3D hierarchical structure and studying on their
photocatalytic properties**

PH. D. Thesis

2016

BIN XU

Department of Material Science

Kyushu Institute of Technology

Content

General Introduction

1. Brief introduction of photocatalytic materials.....	1
2. Brief introduction of cerium dioxide.....	4
3. Purpose of research.....	8
Reference.....	10

Chapter 1:

Synthesis of Morphology controlled CeO₂ with broom-like porous hierarchical structure and studying on catalytical properties.....

1. Introduction.....	15
2. Experiment section.....	16
2.1. Materials.....	16
2.2. Preparation.....	16
2.3. Characterization.....	17
3. Results and discussion.....	18
3.1 Morphology characterization.....	18
3.2 Structure analysis.....	22
3.3 UV-vis diffuse reflectance spectra and band gap energy.....	26
3.4 X-ray photoelectron spectroscopy characterization.....	30
3.5 H ₂ -TPR characterization.....	32

3.6 Mechanism for the fabrication of a porous broom-like CeO ₂ hierarchical architecture.....	34
4. Conclusions.....	35
References.....	36

Chapter 2:

Synthesis and Photocatalytic Performance of Yttrium-doped CeO₂ with a Porous

Broom-like Hierarchical Structure.....

1. Introduction.....	43
2. Experiment section.....	45
2.1. Materials.....	45
2.2. Preparation.....	45
2.3. Characterization.....	46
2.4. Photocatalytic Evaluations.....	47
3. Results and discussion.....	48
3.1. Morphology characterization.....	48
3.2. Structure analysis.....	51
3.3. X-ray photoelectron spectroscopy characterization.....	57
3.4. H ₂ -TPR characterization.....	62
3.5. O ₂ -TPD characterization.....	63
3.6. Photocatalytic activity for acetaldehyde decomposition.....	65
4. Conclusions.....	67

References.....	67
-----------------	----

Chapter 3:

Morphology Control and Photocatalytic Characterization of Yttrium-doped

Hedgehog-like CeO₂.....	72
---	-----------

1. Introduction.....	72
2. Experiment section.....	74
2.1. Materials.....	74
2.2. Preparation.....	74
2.3. Characterization.....	75
2.4. Photocatalytic Evaluations.....	76
3. Results and discussion.....	77
3.1. Structure analysis.....	77
3.2. Morphology characterization.....	82
3.3. UV-vis diffuse reflectance spectra and band gap energy.....	87
3.4. Photocatalytic activity for acetaldehyde decomposition.....	88
4. Conclusions.....	94
References.....	95

Chapter 4:

Synthesis and photocatalytic Characterization of Yttrium-doped CeO₂ with a

sphere structure.....	99
------------------------------	-----------

1. Introduction.....	100
2. Experiment section.....	101
2.1. Materials.....	101
2.2. Preparation.....	102
2.3. Characterization.....	102
2.4. Photocatalytic Evaluations.....	104
3. Results and discussion.....	104
3.1. Morphology characterization.....	104
3.2. Structure analysis.....	107
3.3. X-ray photoelectron spectroscopy characterization.....	111
3.4. Photocatalytic activity for acetaldehyde decomposition.....	115
4. Conclusions.....	116
References.....	117
General conclusions	121
List of publication	123
Acknowledgment.....	124

1. Brief introduction of photocatalytic materials

The 21st century is the century of rapid development of human society. Mankind created so much unprecedented material wealth and promoted the rapid development of human civilization forward. But at the same time there have been environmental pollution, ecological broken ring and a series of threatening human beings survival and development of the major issues[1~3]. Therefore, environmental pollution has become a global focus and solved without delay. Many countries in the world having environmental problems have a deeper understanding and put a lot of manpower, material and financial resources for controlling and prevention environmental pollution, and achieved fruitful results.

Photocatalytic degradation [2,4-5] as a new technology has been widespread concerned and is considered the most promising environmental pollution control technology. Using N-type semi-conductive material as a photocatalytic material and different excitation wavelengths, organic pollutants adsorbed on the catalyst surface ion could be depredated. Compared with other treatment technology, the advantages of semiconductor photocatalytic oxidation / characteristics can be attributed to the following characteristics: (a)generated by UV light[6]; (b)fast reaction speed; [7](c)environment friendly; [8](d)low reaction temperature; [9](e)non-toxic; [10](f)simple equipment and low cost.[11]

From the point of view of photochemistry, the semiconductor photocatalyst can initiate or accelerate specific reduction or oxidation reactions. When the semiconductor absorbs proper light and the consequent photoexcitation

of electron-hole pairs take place if the energy of the incident photons matches or exceeds the bandgap. The conduction band (CB) electrons (e^-) of semiconductor have a chemical potential of +0.5 to 1.5 V versus the normal hydrogen electrode (NHE)[12-14], hence they can act as reductants. The valence band (VB) holes (h^+) exhibit a strong oxidative potential of +1.0 to +3.5 V versus NHE[16-17]. Initially, the energy of incident photons is stored in the semiconductor by photoexcitation. Then it is converted into chemical form by a series of electronic processes and surface/interface reactions[18-20]. In general, the photocatalytic cycle is comprised of three parts shown in Figure 1. Firstly, illumination induces a transition of electrons from valence band to the conduction band, generating an equal number of vacant holes. Secondly, the excited electrons and holes migrate to the surface. Thirdly, they react with adsorbed electron donors and electron acceptors, respectively. However in the second step, a large proportion of electron-hole pairs recombine, dissipating the input energy in the form of heat or emitted light.

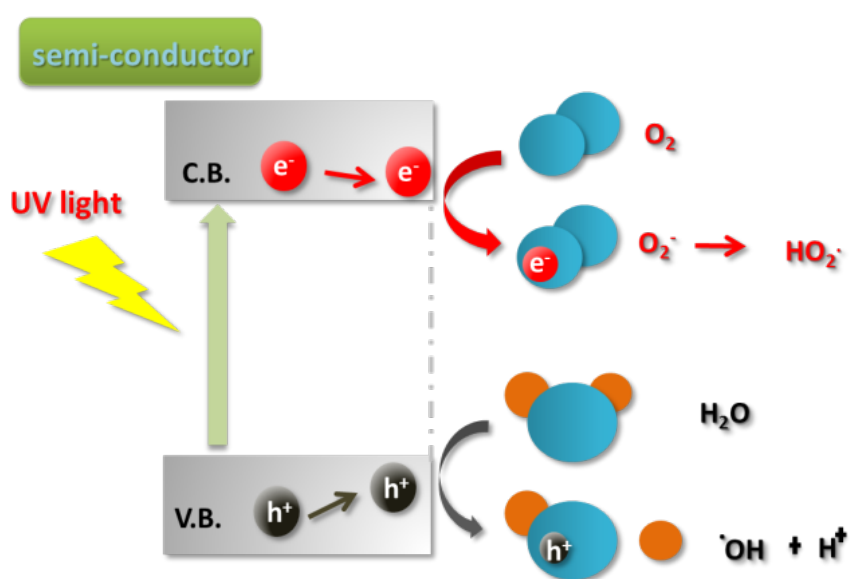
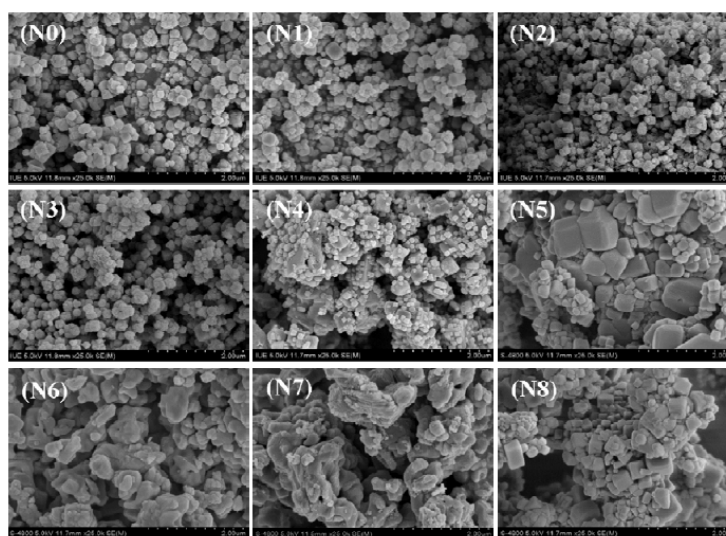


Fig.1 Schematic illustration of basic mechanism of a semiconductor photocatalytic process.

Since Fujishima and Honda reported that TiO₂ can be used to catalytically decomposed H₂O to produce hydrogen under light irradiation for the first time[22,23], many researchers and reports were focused on the study of TiO₂ photocatalysis such as enhancing the photocatalytic. Although TiO₂ were widely used as photocatalysis in practice, its application field is also restricted by its own characteristics. That is because the band gap value of TiO₂ is 3.2eV which is larger to absorb the visible light. And this has become a fatal flaw in the development of photocatalyst. As we all know 90% energy of sunlight are visible light. Various modification methods had appears, such as morphology controlled, elements doped, noble metal loaded, the addition of quantum dots, dyes on the surface and so on, moreover research is ongoing until now.

Simultaneously other kinds of semiconductor also had been developed and used as photocatalyst. Most of semiconductors are oxide (SrTiO₃and WO₃). Some research group using N modified SrTiO₃ and got better photocatalytic affect (Fig 2)[27].



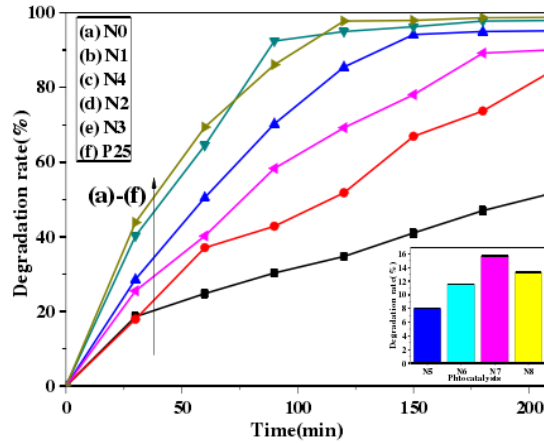


Fig.2 photocatalytic activity of SrTiO3 under different doped concentration of Nitrogen

But these oxides are facing the same problem that because of oxygen their CB position is almost fixed in a high level, so that the position of VB is very awkward. If VB locked in high position, light absorb region will blue shift to UV, if VB locked in low position, it exhibit low reduction ability.

2. Brief introduction of cerium dioxide

In china, there is rich rare-earth resource. These are many unpaired electrons in these rare-earth elements' 4f orbits. And these unpaired electrons can react with most of other elements to form multi-valence or multi-coordinate compound resulted in rare-earth showing super reaction activity[29-31]. Cerium dioxide, an important rare-earth oxide, has been extensively studied due to its significant fluorite-type structure, remarkable redox properties and prominent oxygen storage and release capacity (OSC) via facile conversion between Ce^{4+} and Ce^{3+} oxidation states. And this reaction process is the following equation:



The CeO₂ nanocrystal has a fluorite crystal structure with lattice constant $a = 5.41134$ Å and this structure consists of a face-centered cubic (fcc) unit cell of cations with anions occupying the octahedral interstitial sites. Fig. 3 displays the face-centered crystal cell of the CeO₂ structure, each cerium cation is coordinated by eight nearest-neighbor oxygen anions, while each oxygen anion is coordinated by four nearest-neighbor cerium cations[31-34]. So much more octahedral vacancies could be produced in this open structure which is conducive to transportation of electrons.

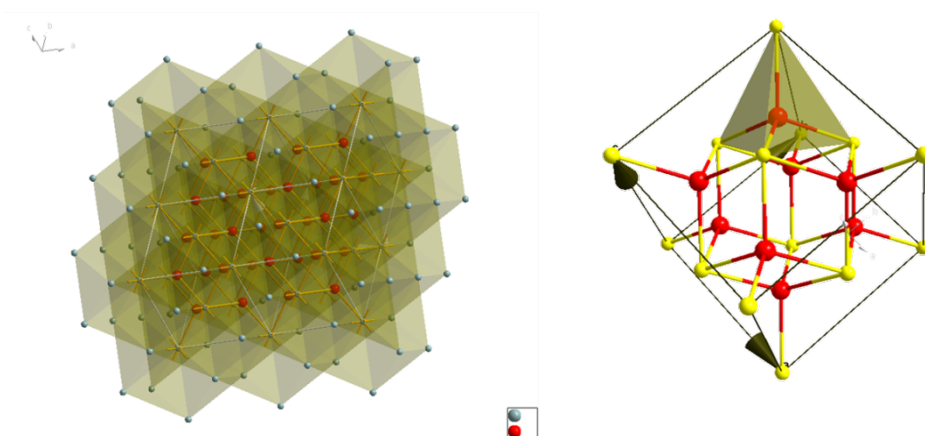


Fig. 3 fluorite-type structure of CeO₂

There are three low-index lattice planes on the surface of CeO₂ nanocrystals: (100), (110) and (111) [8]. As shown in Fig. 4, the stability of three planes is different. Based on density functional theory calculations, the stability follows the sequence: (111) > (110) > (100), while the activity follows the opposite order [10-11]. The energy required to form oxygen vacancies on the (111) surface is greater than those on the (110) and (100) surfaces, so the amount of oxygen vacancies on different planes is different. There are more oxygen vacancies on (110) and (100) planes, which are

favourable in catalytic reactions. Generally, different CeO_2 shapes can expose different lattice planes. Nano-particles usually consist of some octahedra or truncated octahedral shapes. Fig 5 shows they mainly expose the most stable (111) facets in order to minimize surface energy. While nanorods can be terminated by (110) and (100) planes, and nanocubes can expose (100) planes [12]. So there are also more oxygen vacancies on the surface of nanorods and nanocubes.

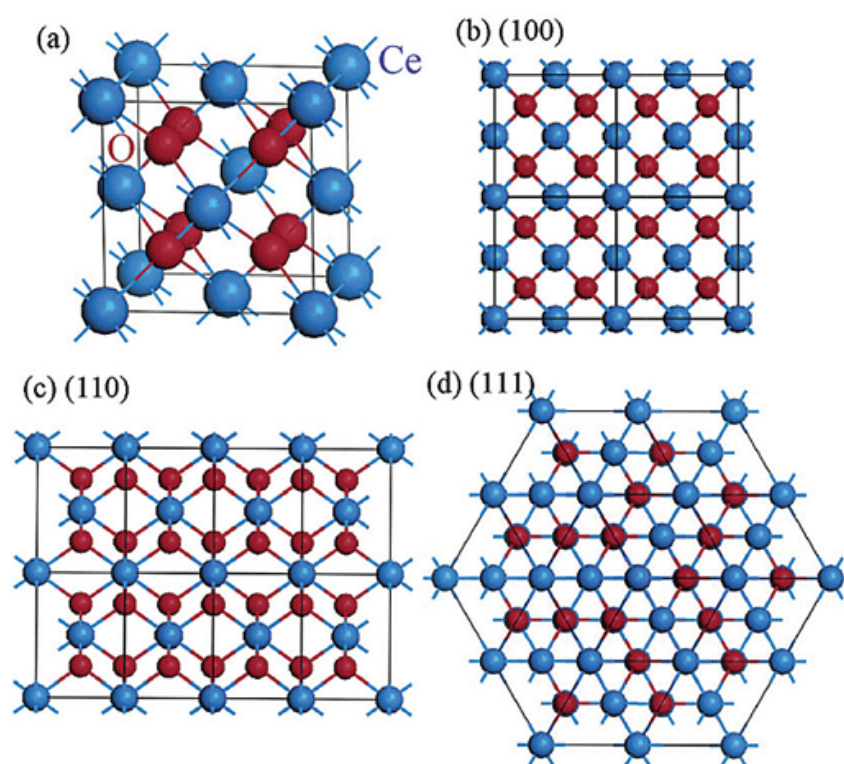


Fig. 4 (a) Face-centered crystal cell of the CeO_2 structure. (b–d) The (100) [or (200)], (110), and (111) planes of the CeO_2 structure

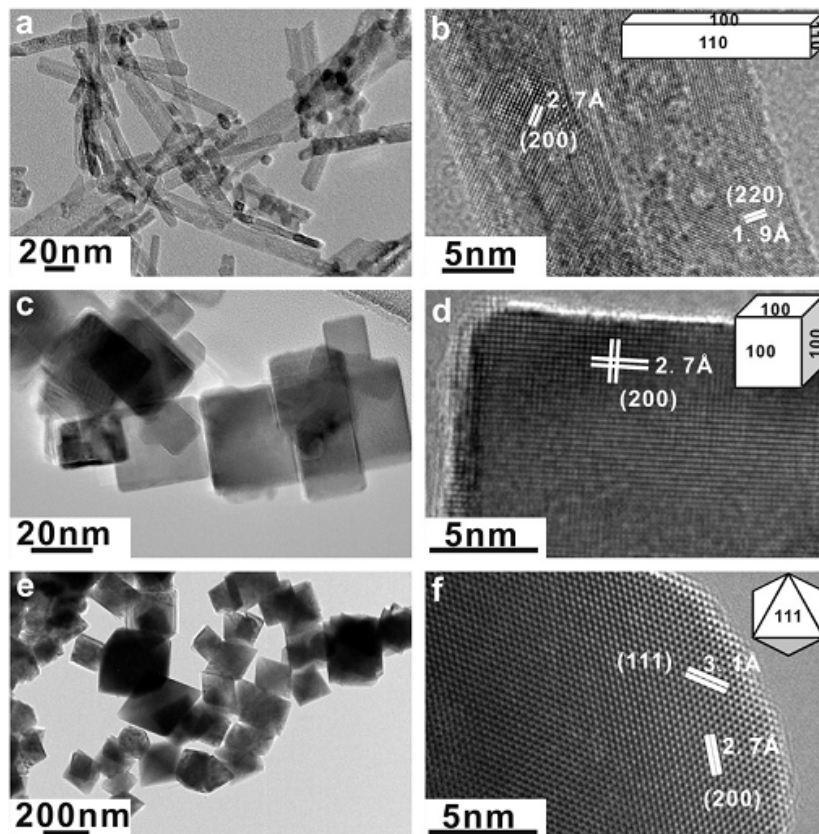


Fig. 5 Representative TEM and HRTEM images of CeO₂ nanocrystals prepared using the hydrothermal methods: (a and b) rods enclosed by the {110} and {100} crystal planes; (c and d) cubes enclosed by the {100} crystal planes; (e and f) octahedra enclosed by the {111} crystal planes;

Except of the exposed planes, oxygen vacancies can also be influenced by many other internal or external factors, such as the shapes, the doping elements, the temperature and others [13]. The formation of oxygen vacancies and other lattice defects are very important for oxygen anion mobility. As the number of vacancies increases, the movement of oxygen atoms becomes easier in the crystal, allowing the ceria to reduce and oxidize molecules or co-catalysts on its surface. The increased diffusion rate of oxygen in the lattice causes increased catalytic activity. So the catalytic activity of ceria is directly related to the number of oxygen vacancies in the crystal.

Ceria-based materials have been extensively utilized in many practical

applications such as polishing materials, solar cells, ultraviolet blocking materials and photocatalytic materials. Pure CeO₂, an n-type semiconductor, has a band gap (3.2eV) similar to those of other commonly utilized semiconductor-based photocatalysts such as TiO₂ [7] and possesses potential as a suitable photocatalyst. Recently, CeO₂ materials with different morphologies have been synthesized by various methods including thermal evaporation [8], coprecipitation [9], and the sol-gel technique [10]. Previous studies have indicated that excellent catalytical performance and easy functionalization of CeO₂ materials can be achieved by controlling their structural properties [11]. For instance, our group had successfully fabricated porous broom-like CeO₂ [12] and CeO₂ with an yttrium-doped hedgehog-like 3D hierarchical structure [13]. Compared with conventional nanowires, nanorods and nanocubes as well as nanoparticles with other shapes, newly constructed CeO₂ with a hierarchical architecture will acquire some special properties that single morphology CeO₂ does not possess [10, 14, 15]. Although some progress has been made in the fabrication of hierarchical architectures composed of 1D nanostructures, the methods usually need special templates through a complex experimental course. For example, Sam L. Mitchell et al. fabricated coral-like mesostructured CeO₂ using an amino acid as a template [16]. Zhong et al. reported the preparation of 3D flowerlike ceria at 180 °C with TBAB as a surfactant and EG as a solvent [17].

3. Purpose of research

The application of morphology and size-controlled, metal and metal oxide

composites and different ionic doping are the three most commonly utilized methods for enhancing the photocatalytic properties of CeO₂-based materials. The keypoint in these approaches is changing the oxygen vacancy concentrations of products, because oxygen vacancies can act as electron or hole capture centers and can trap the photogenerated electrons or holes excited by ultraviolet or visible light. Oxygen vacancies can also effectively restrain the recombination of electron-hole pairs, resulting in improvement of photocatalytic activities [18]. Application of more than two or all of the above methods to the preparation of a 3D hierarchical structure of CeO₂ with a high concentration of oxygen vacancies would be a huge challenge. To the best of our knowledge, there has been no report about CeO₂ with an yttrium-doped hierarchical structure obtained by facile controlled synthesis. So in my thesis, I will adopt the morphology controlled and doping methods to improve the photocatalytic performance of ceria-based materials. And this thesis consisting of four chapters is a summary of my major research work. An outline of each chapter is described below.

Chapter 1 :

In this study, three dimensional hierarchical porous broom-like ceria were fabricated for the first time. Through systematic experiments, the optimum experimental parameters were founded; meanwhile the mechanism for the fabrication of CeO₂ with porous broom-like hierarchical architecture has been deduced. CeO₂ with a porous broom-like has an advantage for catalytic activity attributed to its smaller crystal size and higher concentration oxygen vacancies.

Chapter 2:

In the study, In order to improve concentration of oxygen vacancies further, yttrium was used as a dopant in fabricating yttrium doped porous broom -like CeO₂. The relationship between different yttrium concentration and photocatalytic properties was discussed in detail. And the optimum doping concentration for products were found to be a mole ratio of Ce(NO₃)₃ and Y(NO₃)₃ of 1:0.1.

Chapter 3:

In the study, CeO₂ with yttrium-doped hedgehog-like hierarchical architectures was prepared successfully by a simple hydrothermal method. The optimum experimental conditions for synthesis of octahedral plus nanorod CeO₂ were found to be 0.47 mM Na₃PO₄ and 0.747 mmol Y(NO₃)₃ as original materials and reaction at 200 °C for 24 hours. The method of synthesis is effective and reproducible and can be further expanded to fabricate other rare-earth-doped morphology-controlled inorganic nanoparticle materials. Hedgehog-like yttrium-doped CeO₂ exhibits an advantage of photocatalytic activity. The trend for changes in photocatalytic activities was explained by the oxygen vacancies derived from changes in morphology and yttrium doping.

Chapter 4:

In this part, yttrium doped CeO₂ with a hollow sphere structure were fabricated successfully by a simple hydrothermal method with polystyrene

microsphere as soft template. Meanwhile, photocatalytic activities were compared between octahedral and sphere structure as well as with or without doped. And we find that yttrium doped cerium dioxide with sphere structure shows

Reference:

- [1] M. Fernandez-Garcia, A. Martinez-Arias, J. C. Hanson and J. A. Rodriguez, *Chem. Rev.*, 2004, 104, 4063–4104
- [2] C. T. Campbell and C. H. F. Peden, *Science*, 2005, 309, 713–714.
- [3] Z. L. Wang and X. D. Feng, *J. Phys. Chem. B*, 2003, 107, 13563–13566.
- [4] X. Xie, Y. Li, Z.-Q. Liu, M. Haruta and W. Shen, *Nature*, 2009, 458, 746–749.
- [5] X. Mou, B. Zhang, Y. Li, L. Yao, X. Wei, D. S. Su and W. Shen, *Angew. Chem., Int. Ed.*, 2012, 51, 2989–2993.
- [6] K. Zhou and Y. Li, *Angew. Chem., Int. Ed.*, 2012, 51, 602–613.
- [7] C. Sun, H. Li and L. Chen, *Energy Environ. Sci.*, 2012, 5, 8475–8505.
- [8] M. Nolan, *J. Mater. Chem.*, 2011, 21, 9160–9168.
- [9] D. C. Sayle, S. A. Maicaneanu and G. W. Watson, *J. Am. Chem. Soc.*, 2002, 124, 11429–11439.
- [10] Y. Chen, P. Hu, M.-H. Lee and H. Wang, *Surf. Sci.*, 2008, 602, 1736–1741.
- [11] T. X. T. Sayle, M. Cantoni, U. M. Bhatta, S. C. Parker, S. R. Hall, G. Möbus, M. Molinari, D. Reid, S. Seal and D. C. Sayle, *Chem. Mater.*, 2012, 24, 1811–1821.
- [12] H. X. Mai, L. D. Sun, Y. W. Zhang, R. Si, W. Feng, H. P. Zhang, H. C. Liu and C. H. Yan, *J. Phys. Chem. B*, 2005, 109, 24380–24385.

- [13] C. J. Weststrate, R. Westerstrom, E. Lundgren, A. Mikkelsen and J. N. Andersen, *J. Phys. Chem. C*, 2009, 113, 724–728.
- [14] P. G. Vekilov, *Cryst. Growth Des.*, 2010, 10, 5007–5019.
- [15] W. K. Burton and N. Cabrera, *Discuss. Faraday Soc.*, 1949, 5, 33–39.
- [16] J. Zhang, S. Ohara, M. Umetsu, T. Naka, Y. Hatakeyama and T. Adschiri, *Adv. Mater.*, 2007, 19, 203–206.
- [17] X. Wang, J. Zhuang, Q. Peng and Y. Li, *Nature*, 2005, 437, 121–124.
- [18] Y. Xia, P. Yang, Y. Sun, Y. Wu, B. Mayers, B. Gates, Y. Yin, F. Kim and H. Yan, *Adv. Mater.*, 2003, 15, 353–389.
- [19] H.-I. Chen and H.-Y. Chang, *Ceram. Int.*, 2005, 31, 795–802.
- [20] M. C. Cabús-Llauradó, Y. Cesteros, F. Medina, P. Salagre and J. E. Sueiras, *Microporous Mesoporous Mater.*, 2007, 100, 167–172.
- [21] H. X. Mai, L. D. Sun, Y. W. Zhang, R. Si, W. Feng, H. P. Zhang, H. C. Liu and C. H. Yan, *J. Phys. Chem. B*, 2005, 109, 24380–24385.
- [22] Q. Wu, F. Zhang, P. Xiao, H. S. Tao, X. Z. Wang, Z. Hu and Y. N. Lu, *J. Phys. Chem. C*, 2008, 112, 17076–17080.
- [23] W.-T. Chen, K.-B. Chen, M.-F. Wang, S.-F. Weng, C.-S. Lee and M. C. Lin, *Chem. Commun.*, 2010, 46, 3286–3288.
- [24] C. S. Pan, D. S. Zhang and L. Y. Shi, *J. Solid State Chem.*, 2008, 181, 1298–1306.
- [25] J. Zhang, S. Ohara, M. Umetsu, T. Naka, Y. Hatakeyama and T. Adschiri, *Adv. Mater.*, 2007, 19, 203–206.
- [26] S. W. Yang and L. Gao, *J. Am. Chem. Soc.*, 2006, 128, 9330–9331.

- [27] T. Y. Yu, J. Joo, Y. I. Park and T. Hyeon, *Angew. Chem., Int. Ed.*, 2005, 44, 7411–7414.
- [28] C. C. Tang, Y. Bando, B. D. Liu and D. Golberg, *Adv. Mater.*, 2005, 17, 3005–3009.
- [29] Z. G. Yan and C. H. Yan, *J. Mater. Chem.*, 2008, 18, 5046–5059.
- [30] D. S. Zhang, C. S. Pan, L. Y. Shi, L. Huang, J. H. Fang and H. X. Fu, *Microporous Mesoporous Mater.*, 2009, 117, 193–200.
- [31] M.-M. Titirici, M. Antonietti and A. Thomas, *Chem. Mater.*, 2006, 18, 3808–3812.
- [32] N. C. Strandwitz and G. D. Stucky, *Chem. Mater.*, 2009, 21, 4577–4582.
- [33] X. Lu, T. Zhai, H. Cui, J. Shi, S. Xie, Y. Huang, C. Liang and Y. Tong, *J. Mater. Chem.*, 2011, 21, 5569–5572.
- [34] C. Y. Cao, Z. M. Cui, C. Q. Chen, W. G. Song and W. Cai, *J. Phys. Chem. C*, 2010, 114, 9865–9870.
- [35] D. S. Zhang, H. X. Fu, L. Y. Shi, C. S. Pan, Q. Li, Y. L. Chu and W. J. Yu, *Inorg. Chem.*, 2007, 46, 2446–2451.

Chapter 1

Synthesis of Morphology controlled CeO₂ with broom-like porous hierarchical structure and studying on catalytical properties

1. Introduction:

Cerium is one of the most important rare earth elements due to its promising optical [1-4], magnetic [1, 5-7] and electrical [8-11] performance, which is attributed to cerium's 4f orbital having an unpaired electron [12-14], cerium's atomic magnetic distance being large, its electron energy level being extremely high, and the fact that cerium can react with most of the elements to form multi-valence and multi-coordination compounds [15]. As a significant rare earth oxide, ceria has attracted great attention due to its remarkable redox properties [16] and its oxygen storage and release capability (OSC) via facile conversion between Ce^{3+} and Ce^{4+} oxidation states [17]. It has been utilized in many practical applications such as polishing materials [18], solar cells [19], and ultraviolet blocking materials [20, 21].

Various methods, including thermal evaporation [22], coprecipitation [23], electrospinning (ESP) [24], and the sol-gel technique [25], have been widely utilized for the fabrication of CeO_2 with various morphologies. Recent research has revealed that excellent catalytical performance and easy functionalization of CeO_2 materials are influenced by their structural properties [26]. For instance, our team have successfully fabricated a sesame ball-like CeO_2 : a $Y^{3+}/P(St-AA)$ composite microsphere [27]. Compared with conventional one-dimensional (1D) nanowires, nanorods and nanocubes as well as nanoparticles with other shapes, CeO_2 with a newly constructed three-dimensional (3D) hierarchical architecture would acquire some special properties that CeO_2 with a single 1D morphology does not possess. Although some progress has been made in the fabrication of 3D hierarchical

architectures composed of a 1D nanostructure, the methods for fabrication usually need special templates through a complex experimental course. For example, Titrical et al. prepared a CeO₂ hollow sphere using carbon D-glucose as a template [28]. Leandro Gonza'lez-Rovira et al. used a porous alumina membrane as a template to synthesize CeO₂ nanotubes [29]. However, to the best of our knowledge, there has been no report about broom-like porous CeO₂ obtained by one-step controlled synthesis.

Herein, we report for the first time a facile and feasible approach to prepare broom-like porous CeO₂ by a simple template-free hydrothermal technique. The morphology of CeO₂ can be controlled by adjusting the reaction time, temperature and reactant concentration. Compared with traditional CeO₂ with a 1D morphology structure, catalytic activities of the target products were enhanced.

2. Experiment section

2.1 Materials

Dihydrate trisodium citrate (C₆H₅Na₃O₇·2H₂O), urea and cerium nitrate hexahydrate (Ce(NO₃)₃·6H₂O) were of analytical grade and used without any further purification. All of the above original materials were purchased from Wako Co., Ltd.

2.2 Preparation

A typical synthetic procedure is as follows. First, 5.88 g dihydrate trisodium citrate (C₆H₅Na₃O₇·2H₂O) (DTC) was dissolved in 80 ml deionized water with vigorous magnetic stirring at room temperature. Ten minutes later, 2.4 g urea was added to the solution. The homogeneous mixture was prepared for further use. At the

same time, 1.63 g cerium nitrate hexahydrate ($\text{Ce}(\text{NO}_3)_3 \cdot 6\text{H}_2\text{O}$) was dissolved in 20 ml deionized water with vigorous magnetic stirring at room temperature. Then the cerium nitrate aqueous solution was dropped into the above mixture step by step, and the mixture was stirred for 30 min until the solution changed to a faint yellow color. The mixed solution was then sealed in a 100 ml Teflon-lined autoclave and heated at 100, 120, 150, 180°C for 12, 24, 39, 48 hours, respectively. After cooling to room temperature naturally, a white precipitate was collected by centrifugation and washed with deionized water and ethanol respectively at least three times. Ceria was obtained by calcination of the as-prepared precursor in air at 500 °C for 4 h.

2.3 Characterizations

Morphology and size of the products were examined by an FE-SEM (Hitachi, S-4800, 15KV) and HR-TEM (FEI, Tecnai G2 F30 S-TWIN, 300KV). XRD patterns of the products were obtained on a Bruker-AXS X-ray equipped with graphite monochromator and CuK α radiation ($\lambda = 1.5406 \text{ \AA}$). The crystallite parameters and size were calculated by the Rietveld method (TOPAS 4.0). N₂ adsorption and desorption isotherms were recorded at 77 K using a Nova 4200e instrument. The samples were precisely weighted and degased at 373 K for 3 h. The specific surface area was calculated by the 5 points Brunauer-Emmit-Teller theory. Raman analysis (Renishaw, In via) was performed using a 532 nm excitation laser with 5 mW and an air-cooled CCD detector. Raman peak shifts were determined by fitting with the Lorentzian and Gaussian composite function. Absorption edge and band gap energy were investigated by using a UV-vis diffuse reflectance spectral (Varian, Cary 5000).

An x-ray photoelectron spectroscopy (XPS) experiment was carried on a Shimadzu KRATOS AXIS-NOVA system at room temperature under 10^{-9} pa using Al K α radiation and Au 4f peak (83.8 eV) reference. Temperature-programmed reduction (TPR) experiments were performed on FTNESORB-3010 using 10% H $_2$ in air as the analytic gas, with a flow of 50 cm 3 /min over a temperature range of 50-700 $^{\circ}$ C. A sample mass of ca. 500 mg was pretreated by calcinated at 200 $^{\circ}$ C for 1h and subsequently cooled to 100 $^{\circ}$ C under an Ar flow before being used. The consumption of H $_2$ was monitored by a thermal conductivity detector (TCD) operating at 60 $^{\circ}$ C and 80mA.

3. Results and discussion

3.1 Morphology characterization

The morphology of as-prepared CeO $_2$ (DTC:Ce=1.3:1 /120 $^{\circ}$ C) with different reaction times were investigated by the FE-SEM and HR-TEM. Fig.1.(a)-(d) show FE-SEM images of CeO $_2$ nanoparticles with a hierarchical structure and the formation course of the broom-like porous CeO $_2$. Fig.1.(a) shows the morphology of individual flower-like CeO $_2$ at 12h with diameters of almost 5 μ m and with each petal thickness being approximately 50 nm. The inset image (Fig. 4) displays clear lattice fringes with interplanar spacing of 0.32 nm that were assigned to the CeO $_2$ (111) crystal plane. Fig.1.(b)-(d) show that morphology transformed with increase in reaction time. The shape changed to a broom-like shape with an average diameter of 4 μ m. Numerous nanorods are connected at one end and diverge at the other end to form a broom-like hierarchical architecture. The nanorods have uniform diameters of 200 nm and lengths

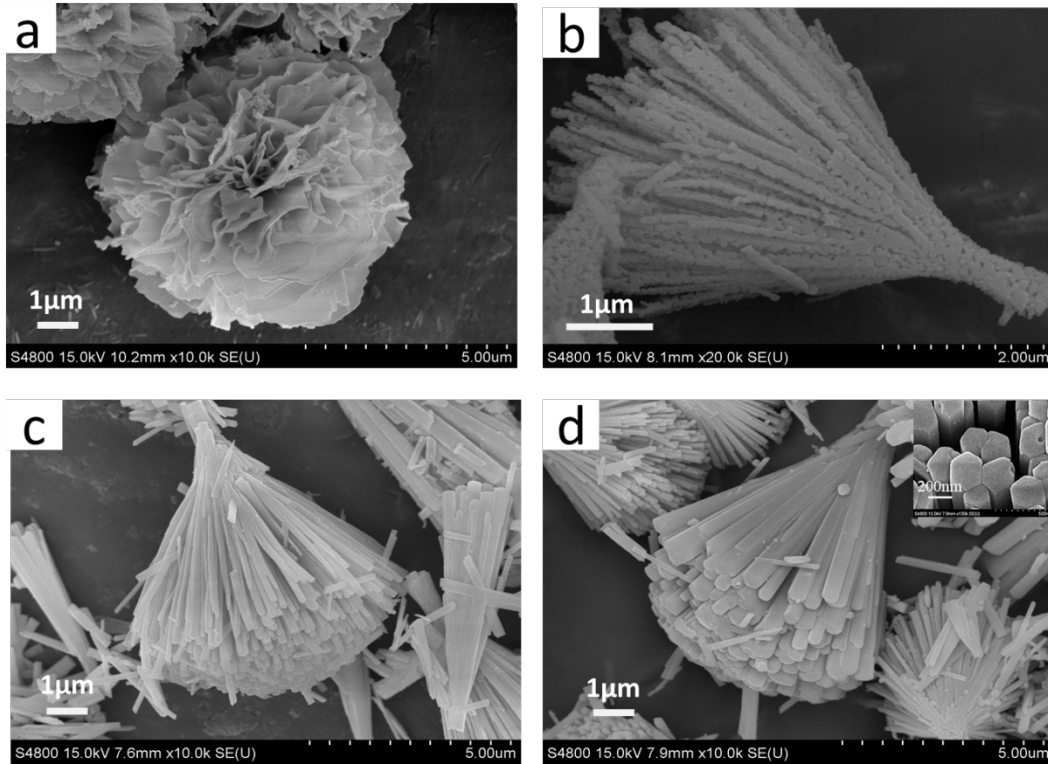


Fig.1: FE-SEM images of as-fabricated samples (DTC:Ce=1.3:1 /120°C) with different reaction times:(a) 12 hours, (b) 24 hours, (c) 39 hours, and (d) 48 hours.

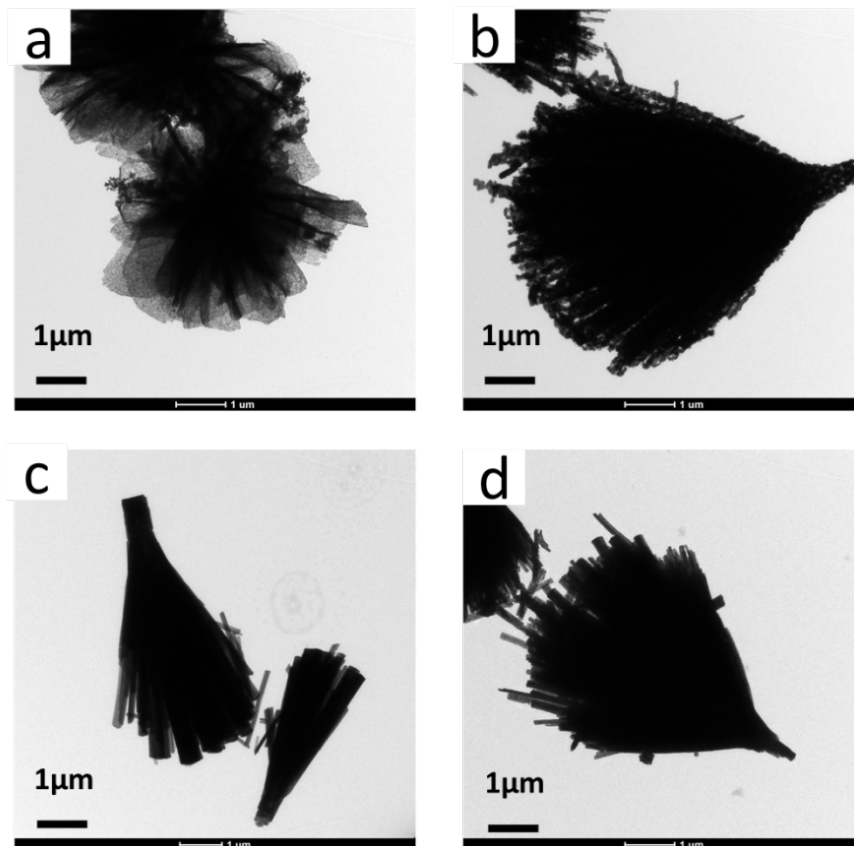


Fig 2: TEM images of as-fabricated samples at different reaction times: (a)12 hours, (b) 24 hours, (c) 39 hours, and (d) 48 hours.

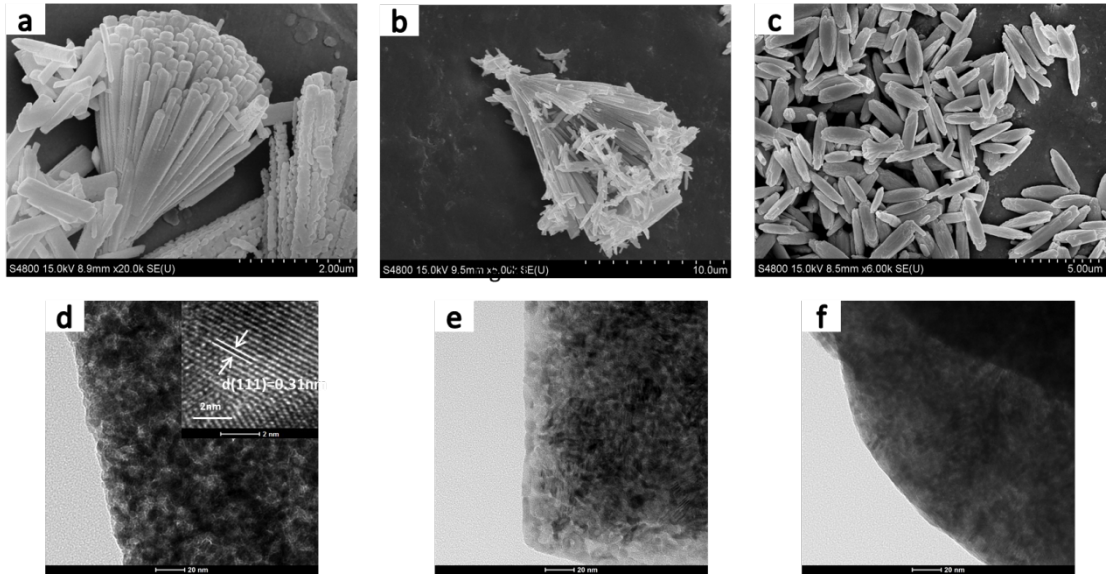


Fig.3:FE-SEM images of as-fabricated samples: (a) DTC:Ce=1:1 /120°C/24 hours, (b) DTC:Ce=1.9:1 /120°C/24 hours, and (c) DTC:Ce=13:1 / 180°C/ 24 hours.

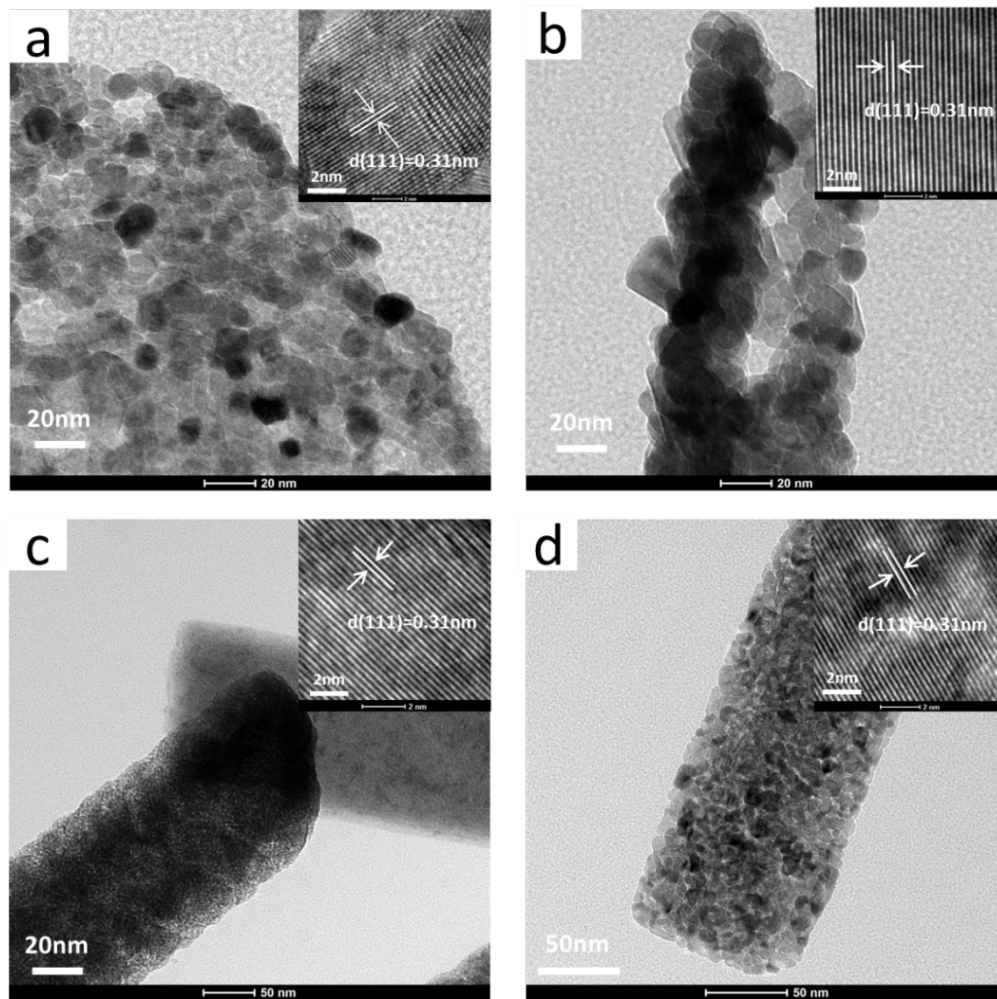


Fig.4: HR-TEM images of as-fabricated samples (DTC:Ce=1.3:1 /120°C) with different reaction times:(a) 12 hours, (b) 24 hours, (c) 39 hours, and (d) 48 hours.

of 4 μm . In addition, smoothness of the surfaces of nanorods was improved by the increasing time. Fig.4.(b) shows an HR-TEM image of an as-fabricated sample at 24 hours. The smallest unit of morphology is ceria nanoparticles of about 10 nm in diameter. Nanoparticles aggregate with orientation to form a porous nanorod with an internal diameter of 20 nm. The interplanar spacing of 0.32 nm is equal to the bulk CeO_2 (111), indicating that the crystal lattice does not expand or contract, although the morphology changed to a porous broom-like structure. Compared with the image in Fig. 1 (b) and Fig.4 (b), the rod surface has become much smoother and the particle size decreased to 5 nm obviously. At the same time, a porous structure still exists with internal size of pores remaining unchanged (Fig 1(c) and Fig. 4(c)). Fig. 1(d) shows a broom-like hierarchical architecture with a glossy surface after reaction for 48 hours. However, a porous structure is no longer observed. The nanorod morphology can be clearly observed in the inset image of Fig. 4(d). CeO_2 nanoparticles spontaneously assembled to become a hexagonal-prisms nanorods aggregate structure. This transformation course is discussed in the section on the fabrication mechanism.

Fig.3 (a)-(b) image show the morphology remains the broom-like accompany by varying molar concentration of sodium citrate and cerium nitrate from 1:1 to 1.9:1. The results indicate the stoichiometry has no influence to the morphology controlled. Fig. 3(c) image shows that hierarchical structure has transformed into the Spindle-like along with the reaction temperature increasing. Fig.3 (d)-(f) show the TEM images of as-fabricated samples. From the images we can find that approximate 10nm nanoparticles composed of various morphologies CeO_2 although the experiment

parameters have changed. Clear CeO₂ (111) lattice fringes with the interplanar spacing of 0.32 nm can be detected from the inset graph Fig.3(d).

3.2 Structure analysis

Fig. 5(a)-(b) shows XRD patterns of CeO₂ prepared under different experimental conditions. Characteristic peaks at 28.5, 33.0 47.4 and 56.3 2 θ are attributed to pure cerium oxide with a cubic fluorite structure (JCPDS No. 34-0394) and are assigned to the crystal planes (111), (200), (220) and (311), respectively. The sharp diffraction peaks from both samples suggest a high degree of crystallinity of the fabricated CeO₂ nanocrystal, and no impurity peaks appeared, indicating that reaction time, temperature and mole ratio of original materials have no effect on CeO₂ crystalline phase purity. The relative intensity between characteristic peaks at 28.5, 33.0 47.4 and 56.3 2 θ does not change clearly, suggesting that there is no preferred orientation or that crystal orientation growth did not occur. However, the strongest diffraction peak at 28.5 (111) shows clear changes in intensity and peak shape with increase in reaction time (see the Fig. 5(a)). Compared with other reaction times, the full width at half maximum (FWHM) value reaches the maximum at 39 hours, indicating that the smallest particle size of the product was obtained at that time according to the Scherrer equation. This phenomena did not been observed in other diffraction lines changed with reaction temperature and original materials stoichiometry (Fig. 5(b) and Fig. 5(c)), indicating that reaction time have a strong effect on the morphology and particle size of products. This result is consistent with Rietveld refinement results and with the FE-SEM and HR-TEM observations.

Rietveld refinements were also carried out according to the diffraction lines by varying parameters [30] such as background, unit cell, and isotropic thermal parameters and could obtain the results such as crystal lattice value, grain size, atom position and occupancy. Fig. 5(d) demonstrated the difference in product (mole ratio DTC: Ce=1.3:1 and reaction at 120 °C for 39 h) between the calculated value and measured data by the TOPAS 4.0. The calculated lattice parameter (a) is approximately 0.542 nm and the average grain size is 4.5 nm ($R_{wp}=2.36\%$). R_{wp} value was below five percent, indicating that the calculated value is correct and credible. Although the as-fabricated sample has the same space group with bulk CeO₂ (Space Group: Fm-3m (No.225)), lattice parameter (a) shows small changes compared with the standard value (0.541nm). The expansion of lattice parameter (a) indicated the reduction of Ce⁴⁺ to Ce³⁺[31, 32]. The inset graph shows the true structure according to the results of calculation. Each cerium atom is surrounded by eight oxygen atoms and shows a standard MO₈ type structure (FCC). The synthesized samples have similar structure under different experimental conditions, although the morphologies of the products have changed obviously. The calculated grain sizes and lattice parameters of as-fabricated products are summarized in Table 1.

Raman spectroscopy is considered to be a very facile and nonvolatile technique for characterization of ceria nanoparticles. In this study, we also investigated the oxygen vacancies of the prepared CeO₂ by Raman technology. Fig.6.(a)~(c) show the recorded Raman spectra of the as-prepared products under different experimental

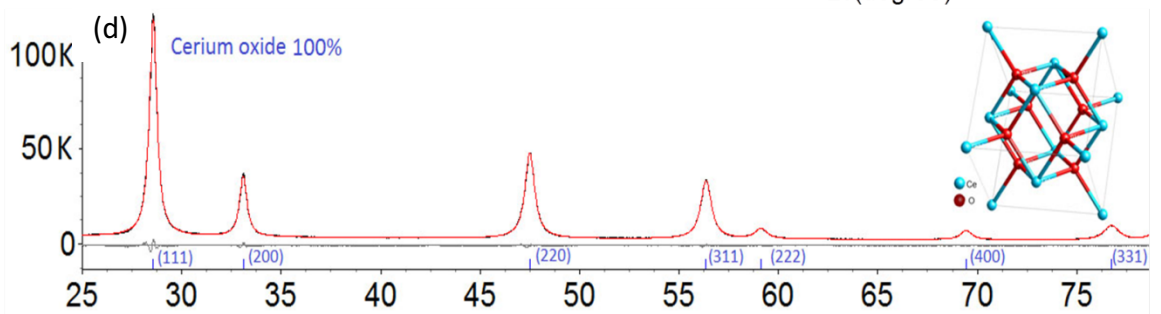
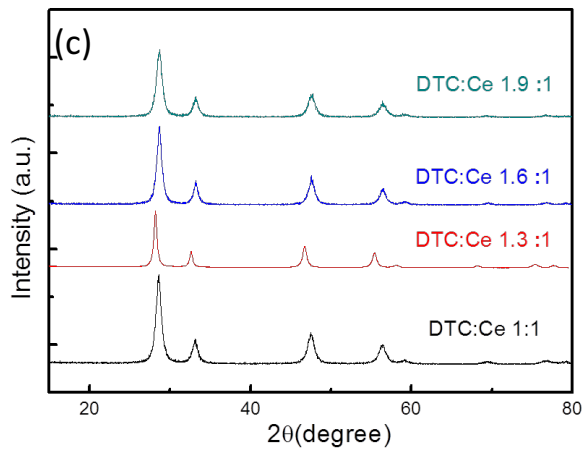
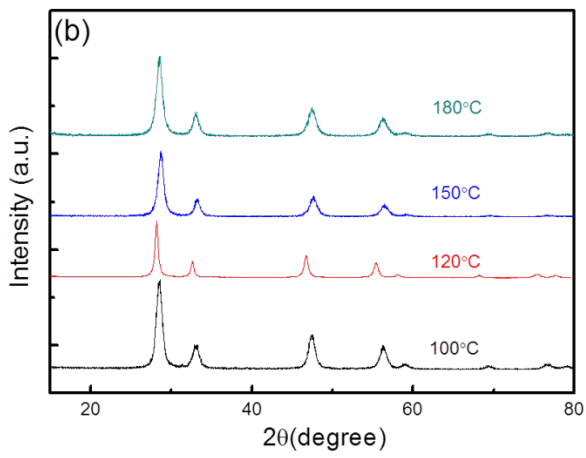
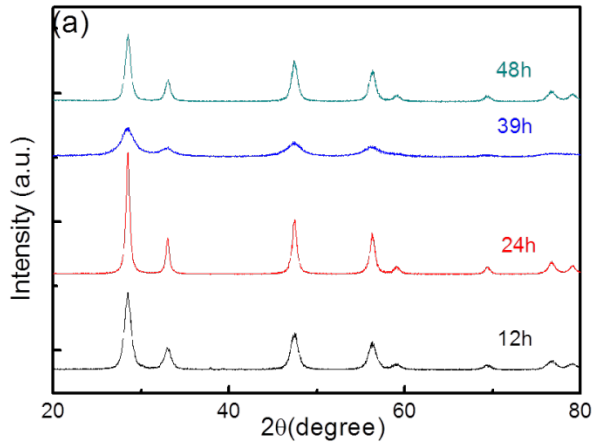


Fig.5: XRD patterns of as-fabricated samples: (a) (DTC:Ce=1.3:1 /120°C) different reaction times, (b) (DTC:Ce=1.3:1 /24h) different reaction temperatures,(c) with different molar ratios of original materials and (d) Rietveld refinement spectra.

conditions. A typical Raman shift at $\sim 460\text{ cm}^{-1}$ and a relatively weak shift at $\sim 600\text{ cm}^{-1}$ can be detected. The shift at $\sim 460\text{ cm}^{-1}$ can be assigned to F2g vibration of the fluorite-type structure and it can be considered as the symmetric stretching mode of oxygen atoms around cerium ions [33], and the molecule retains its tetrahedral symmetry throughout. Except for the strongest peak, a weak and less prominent band near $\sim 600\text{ cm}^{-1}$ can be founded which are assigned to the defect spaces which include oxygen vacancies[34, 35]. According to previous reports [36, 37] that not all cerium ions show Ce^{4+} chemical valence in the lattice and small cerium ions show Ce^{3+} tervalence [17]. In order to maintain the particles in an electrically neutral state, the lattice oxygen would escape from the structure and finally result in the formation of intrinsic oxygen vacancies. Many studies have shown that the presence of oxygen vacancies has a significant role in promoting adsorption and activation of O_2 , which may lead to improvement of the photocatalytic activity [17,32]. The integral area ratios of oxygen vacancy peak (R_D) and F2g are summarized in Table 1. The value of $R_D/\text{F2g}$ rapidly increased at first, reached a maximum at 39 hours, and then decreased with further increase in reaction time. CeO_2 with a porous broom-like hierarchical architecture exhibits the highest value. The reason is that the basic unit of the target products is CeO_2 nanoparticles with diameters of 5 nm. As a consequence, this structure has a larger specific surface area (see Table 1) and higher oxygen vacancy concentration attribute to quantum size effect, and more activity oxygen exists on

higher specific surface area [38]. Fig. 3(b) shows the Raman shifts and relativity intensity values of different reaction temperatures. The value of the integral area ratio of R_D and F2g would increase with increase in hydrothermal temperature, although the F2g and R_D shift were still at $\sim 460\text{ cm}^{-1}$ and 600 cm^{-1} , respectively, indicating that a high temperature is beneficial for the formation of intrinsic oxygen vacancies. However, an entirely different phenomenon was observed from Fig. S5. The values ($R_D/F2g$) of as-fabricated samples with different original materials mole ratios were very similar, which may be due to morphologies did not change significantly and always maintains the bloom-like hierarchical structure.

3.3 UV-vis diffuse reflectance spectra and band gap energy

The UV-vis diffuse reflectance spectra of as-fabricated samples of different reaction times are shown in Fig. 7(a). The optical band gap energy (E_g) can be calculated from the plot between $E = 1240/\lambda(\text{nm})$ [39-41], where λ is the wavelength corresponding to the absorption edge, and $[F(R)hv]^{1/2}$ [42, 43] as shown in Fig. 7 (b). Traditional bulk CeO_2 has absorption at $\sim 380\text{ nm}$ and band gap energy at 3.20 eV , which originate from the charge transfer between O_{2p} and Ce_{4f} states in O^{2-} and Ce^{4+} [41, 44]. The absorption of products has a distinct shift to the visible region compared with CeO_2 with a traditional 1D morphology structure. Subtle differences in band gap between various morphologies of broom-like ceria were detected from the plot of K-M curves. Fig. 7(b) shows the calculated energy gap value of samples 12h, 24h, 39h and 48h and their E_g values are 2.97 eV , 3.06 eV , 2.86 eV and 3.04 eV , respectively.

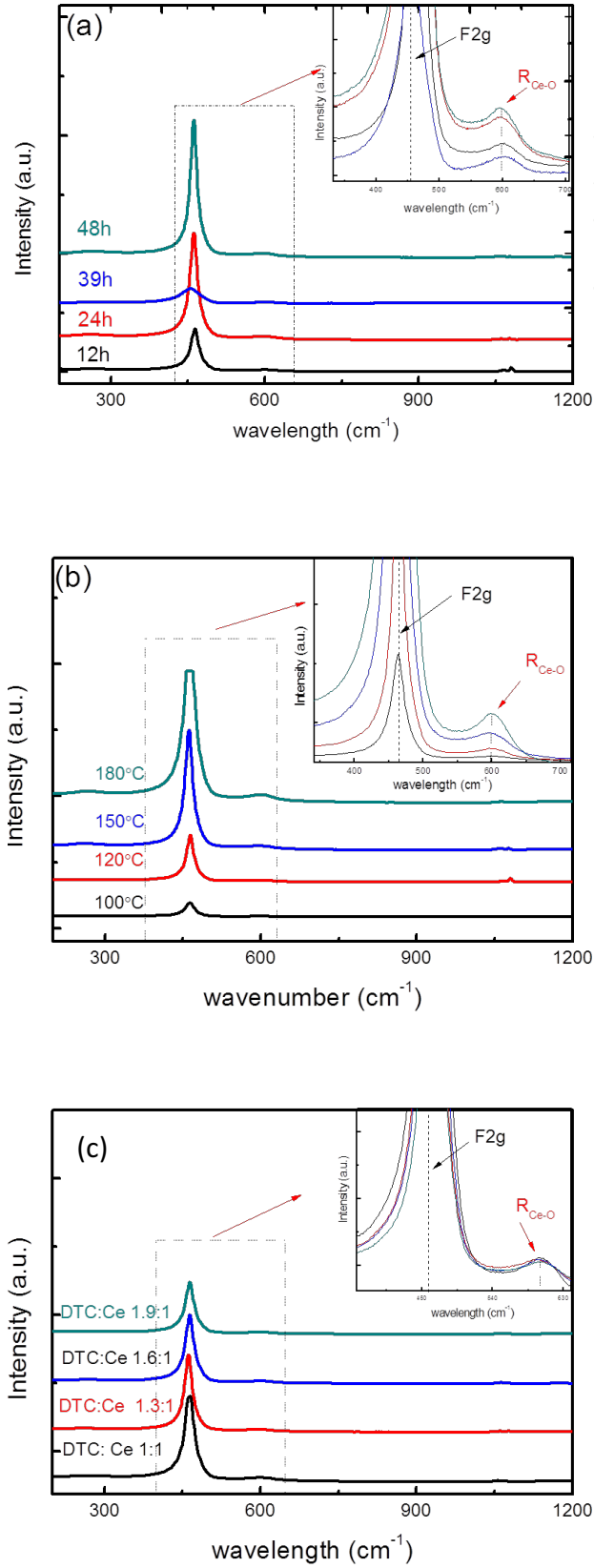


Fig.6: Raman spectra of as-fabricated samples: (a) (DTC:Ce=1.3:1 /120°C) different reaction times, (b) (DTC:Ce=1.3:1 /24h) different reaction temperatures and (c) with different molar ratios of original materials.

Obviously, the as-fabricated sample for 39 h possess lower energy gap, indicating that CeO₂ with a porous broom-like hierarchical structure can photogenerate more hole-electron pairs under visible-light irradiation. And the different band gap between the samples for 39h and 24h may attribute to oxygen vacancy[45-47]. Sample for 39h possesses higher concentration of oxygen vacancy than 24h (see the table 1) and shows the red shift of band gap although they have similar broom-like morphology. Fig 8(a)-(b) and Fig 9(a)-(b) show UV-vis diffuse reflectance spectra and band gaps of as-fabricated samples under the conditions of different reaction temperatures and different mole ratios of the original materials, respectively. Compared with other reaction temperatures, the absorbance edge of the product fabricated at 120 °C shows a blue shift according to Fig 8(a), which attribute to only broom-like morphology CeO₂ obtained at 120 °C. The shape of product is flower-like structure when reaction temperature is below 120 °C, as well as only shuttle-like structure CeO₂ can be detected when the temperature exceeded 120 °C. The samples have similar band gap values (~3.0 eV) although the mole ratios of original materials have changed (see Fig 9(a)~(b)). Therefore, the change in absorbance edge or band gap value may be caused by the change in morphology. These results are consistent with the results of Raman analysis, and this optical property is very important for good photocatalytic performance.

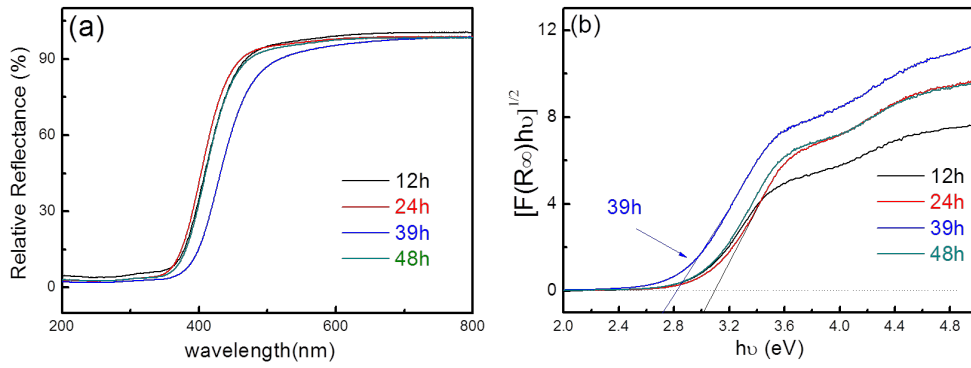


Fig.7: (a) UV-vis diffuse reflectance spectra and (b) band gaps of samples (DTC:Ce=1.3:1 / 120°C) with different reaction times.

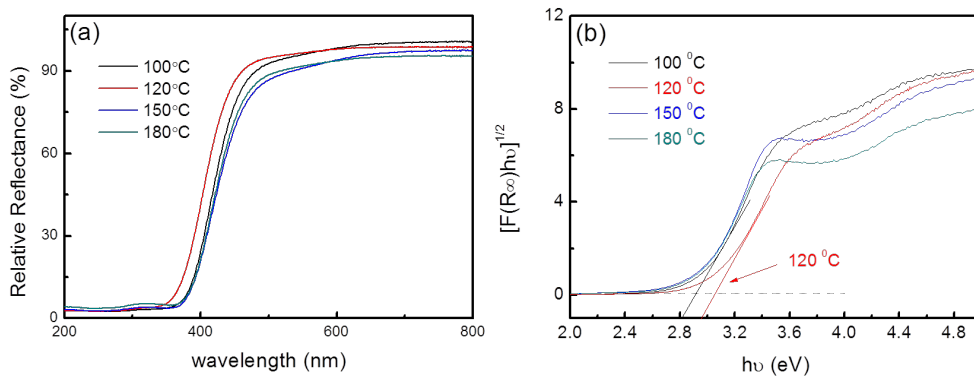


Fig 8: (a) UV-vis diffuse reflectance spectra and (b) band gaps of samples (DTC:Ce=1.3:1 / 24h) with different reaction temperatures.

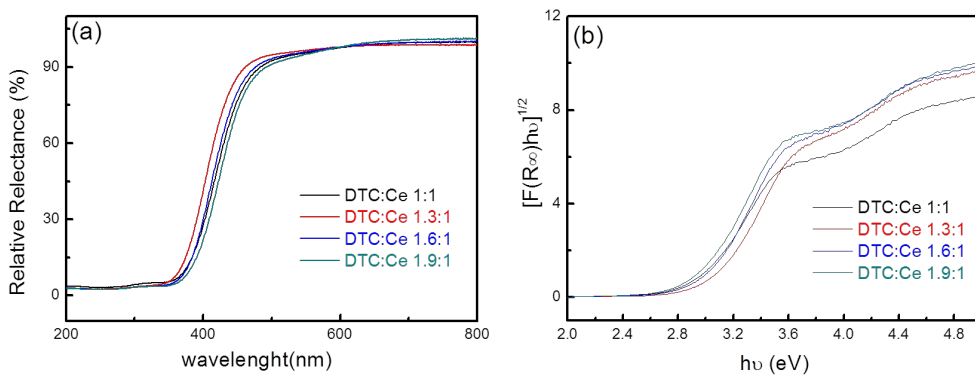


Fig 9: (a) UV-vis diffuse reflectance spectra and (b) band gaps of samples under 120°C for 24 hours with different molar ratios of original materials.

3.4 X-ray photoelectron spectroscopy characterization

Fig. 10(a) shows Ce 3d electron core level XPS spectra for as-fabricated samples and the change in the Ce 3d_{3/2} and Ce 3d_{5/2} components depending on the Ce³⁺ and Ce⁴⁺ oxidation states. Five pairs of doublets, (u, v), (u₁, v₁), (u₂, v₂), (u₃, v₃) and (u₀, v₀), can be decomposed from the origin region, where u and v come from Ce 3d_{3/2} and Ce 3d_{5/2} states, respectively. We observed that (u, v), (u₂, v₂) and (u₃, v₃), which were attributed to Ce 3d⁹ 4f² O 2p⁴, Ce 3d⁹ 4f¹ O 2p⁵ and Ce 3d⁹ 4f⁰ O 2p⁶ final states, respectively, all belonged to the Ce⁴⁺ oxidation state. The two pairs doublets as (u₁, v₁) and (u₀, v₀) originated from the Ce 3d⁹ 4f¹ O 2p⁴ and Ce 3d⁹ 4f¹ O 2p⁵ final state, respectively, which correspond to the Ce³⁺ oxidation state. The relative amount of cerium in the trivalent oxidation state can be calculated from equation (1)[48]:

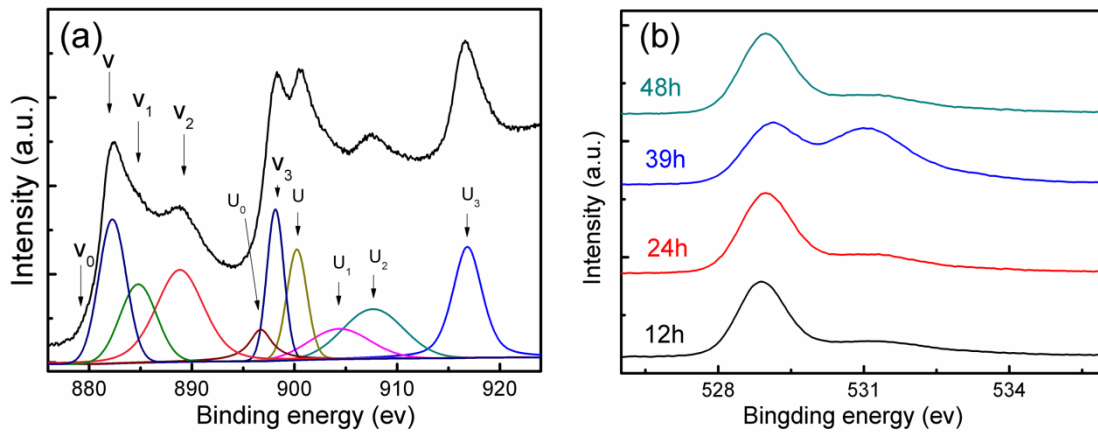


Fig.10: (a) Ce 3d core level XPS spectra of as-fabricated samples (DTC:Ce=1.3:1, 120°C, 39h) and (b) O1s core level XPS spectra of as-fabricated samples (DTC:Ce=1.3:1 /120°C) with different reaction times.

Samples (DTC:Ce=1.3:1 120 °C under different time)	Lattice parameters a (Å)	Calculated grain size (nm)	Particle size (nm)	Area R _D /Area F _{2g} (%)	S _{BET} (m ² /g)
12h	5.413	4.51	~10	9.21	35.6
24h	5.417	4.60	~10	9.46	46.9
39h	5.423	4.50	~5	9.67	166.1
48h	5.415	5.52	~10	9.24	30.4

Table. 1: Relevant data of as-fabricated samples used in the work.

Sample/different reaction time(h)	[Ce ³⁺]/[Ce ³⁺ +Ce ⁴⁺] %	[O _{sur}]/[O _{sur} +O _{lat}] %
12	14.3	34.8
24	18.7	31.7
39	22.5	50.7
48	15.7	35.9

Table 2 : calculated [Ce³⁺] and [O_{sur}] concentration of as-fabricated samples (DTC:Ce=1.3:1, 120°C) from the XPS spectrum.

$$\frac{[\text{Ce}^{3+}]}{[\text{Ce}^{3+}+\text{Ce}^{4+}]} = \frac{\text{area}(V_0, V_1, U_0, U_1)}{\text{total area}} \quad (1)$$

Results for oxidation states are summarized in the table 2. The fitting data demonstrated that the as-fabricated samples for different reaction time exhibits variation of $[\text{Ce}^{3+}]$ concentration. Sample 39h possesses about 22.5% of the cerium ions in the +3 state and this value is higher than the other samples.

Fig. 10(b) shows O 1s electron core level XPS spectra for as-fabricated samples with different reaction times. One peak around 529.0eV with a shoulder around 531.1 eV can be clearly seen, and they can be attributed to lattice oxygen (O_{lat}) and surface active oxygen (O_{sur}), respectively. After deconvolution and multiple-peak separation, we could obtain the surface ratio from the equation (2):

$$\frac{[\text{O}_{\text{sur}}]}{[\text{O}_{\text{sur}}+\text{O}_{\text{lat}}]} = \frac{\text{area}(\text{O}_{\text{sur}})}{\text{total area}} \quad (2)$$

Results for surface active oxygen are summarized in the table S1. Value of surface ratio for sample 39 hours is approximately 50.7% and this value is higher than others. The $[\text{Ce}^{3+}]$ and $[\text{O}_{\text{sur}}]$ concentration value of sample 39h indicating that CeO_2 with a porous broom-like structure should have higher surface active oxygen concentration and should have higher catalytic activity [49]. This result is well consistent with the H_2 -TPR characterization and Raman analysis.

3.5 H_2 -TPR characterization

Temperature-programmed reduction (TPR) in a flow of hydrogen up to 700 °C was used to characterize the catalysts and probe redox properties. Fig. 11(a) and (b) show the H_2 -TPR traces of as-fabricated samples under the condition of different reaction times and temperatures. The TPR trace of samples fabricated with different

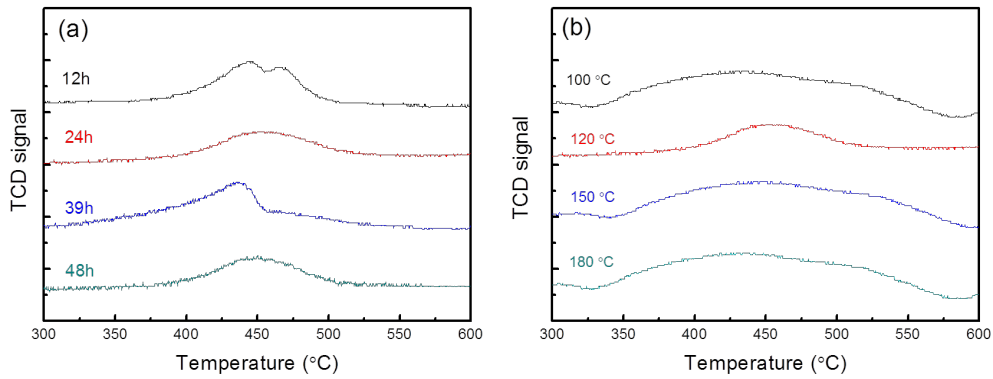
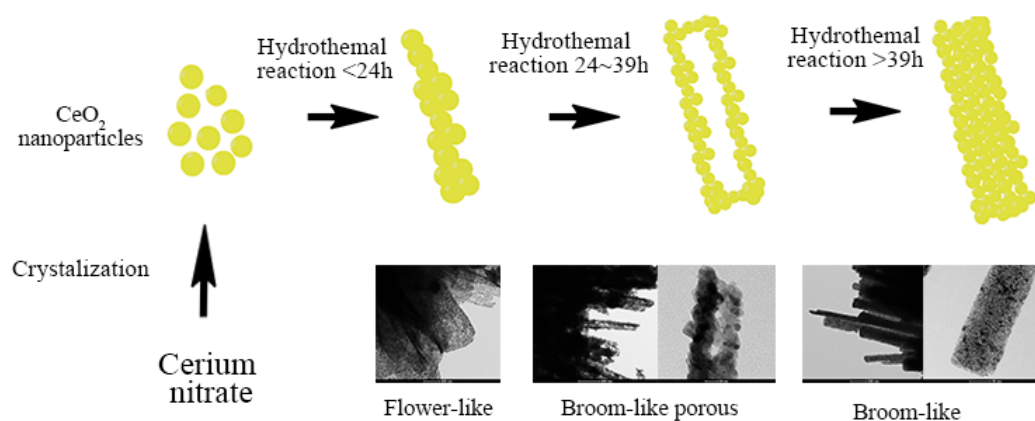


Fig.11: H₂-TPR profiles of as-fabricated samples: (a) (DTC:Ce=1.3:1 /120°C) different reaction times and (b) (DTC:Ce=1.3:1 /24h) different reaction temperatures.

times at 120 °C(Fig. 6(a)) indicated a reduction behavior at around 450 °C, which is attributed to the reduction of surface-capping oxygen of ceria [50]. The relatively moderate shift (~20 °C) of the main reduction peak to low temperature (ca. 430 °C), relative to the profile of other samples, implies that the reducibility of sample fabricated after reaction for 39 hours has been considerably enhanced. The catalytic activity of CeO₂ depended strongly on the morphology and crystal size [51], therefore CeO₂ with a porous broom-like hierarchical structure and crystal size of about 5 nm would lead to the reducibility enhance. The TPR trace of samples fabricated at different temperatures for 24h (Fig. 6(b)) shows a similar reduction peak at around at 450 °C, which is attributed to similar particle sizes although the morphology of products changed from flower-like and broom-like to shuttle-like. Although the morphology of products changed from flower-like and broom-like to shuttle-like with increasing reaction temperature, the particle size value of each product is very close (average particle size. 10 nm). Consequently a broad reduction peak around at 450 °C can be detected.

3.6 Mechanism for the fabrication of a porous broom-like CeO₂ hierarchical architecture

Results of systematic experiments showed that the reaction time and reaction temperature, as the key parameters, play a vital role in the fabrication of CeO₂ with a broom-like porous hierarchical architecture. Based on the results of electron microscopy, we propose a new mechanism for the formation of broom-like porous CeO₂. The mechanism is an Ostwald ripening process [52-54] coupled with crystal growth as schematically illustrated in Scheme 1.



Scheme 1: Schematic illustration of the Ostwald ripening process of the porous broom-like CeO₂.

At first, numerous nanocrystals form in the solution via crystallization. As the reaction process progresses, these nanocrystals self-assemble orientationally as nanorods with the aid of sodium citrate. Because of this kind of selected adsorption can effectively reduce the surface energy through increase specific surface area. When the reaction time was less than 24 hours, the nanorods coalesced together in a divergent form. This kind of coalescent resulted in the formation of flower-shaped

morphology owing to the large interspaces between aggregated nanorods. As the Ostwald ripening process progresses, many nanocrystals are formed and self-assembled on the nanorod surface. The outer nanoparticles become larger, while the inner nanoparticles become smaller and finally they disappear due to the crystal concentration difference between the outer and inner parts of the nanorod [35]. Then a nanorod with a porous structure is formed. At the same time, the interspaces between the rods gradually shrink, and the rods become close to each other. A broom-like porous structure is formed at this stage. When the reaction time was 24 hours, the quantity of outer large particles was much more than inner small particles, the average particle size reached about 10 nm. And when the reaction time was 39 hours, more new small particles will growth on rod surface which resulted in the average particle size decreased again. That's the reason the sample 24h and 39h present differential properties although they possess similar A broom-like porous structure. With further increase in the reaction time, the particles become large enough to completely fill the formed porous structure. Therefore, with a long reaction time, only a broom-like structure without a porous morphology could be obtained.

4. Conclusions

In summary, a broom-like porous CeO₂ hierarchical architecture was successfully prepared by a simple hydrothermal method. The Ostwald ripening theory could explain the morphology evolution process. The optimum reaction time and temperature for the synthesis of porous broom-like CeO₂ was found to be 39 hours and 120 °C, respectively. This method for synthesis is effective and reproducible and

can be further expanded to fabricate other morphology-controlled inorganic nanoparticles. The results of H₂-TPR, XPS, Raman and BET analyses demonstrated the CeO₂ with a porous broom-like has an advantage for catalytic activity. Consequently, the as-synthesized broom-like porous CeO₂ is a promising material for practical application in photocatalytic materials and SOFCs as well as other new environment-friendly materials.

References

- [1] M. Taguchi, S. Takami, T. Naka, T. Adschiri, *Crystal Growth & Design*, 9 (2009) 5297-5303.
- [2] G.I.N. Waterhouse, J.B. Metson, H. Idriss, D. Sun-Waterhouse, *Chemistry of Materials*, 20 (2008) 1183-1190.
- [3] X. Xu, Z. Saghi, G. Yang, R.J. Hand, G. Möbus, *Crystal Growth & Design*, 8 (2008) 1102-1105.
- [4] N. Wetchakun, S. Chaiwichain, B. Inceesungvorn, K. Pingmuang, S. Phanichphant, A.I. Minett, J. Chen, *ACS Applied Materials & Interfaces*, 4 (2012) 3718-3723.
- [5] S.-Y. Chen, K.-W. Fong, T.-T. Peng, C.-L. Dong, A. Gloter, D.-C. Yan, C.-L. Chen, H.-J. Lin, C.-T. Chen, *The Journal of Physical Chemistry C*, 116 (2012) 26570-26576.
- [6] K.V. Hoecke, J.T.K. Quik, J. Mankiewicz-Boczek, K.A.C.D. Schamphelaere, A. Elsaesser, P.V.d. Meeren, C. Barnes, G. McKerr, C.V. Howard, D.V.D. Meent, K. Rydzyński, K.A. Dawson, A. Salvati, A. Lesniak, I. Lynch, G. Silversmit, B.D. Samber, L. Vincze, C.R. Janssen, *Environmental Science & Technology*, 43 (2009)

4537-4546.

[7] C. Ma, D. Wang, W. Xue, B. Dou, H. Wang, Z. Hao, *Environmental Science & Technology*, 45 (2011) 3628-3634.

[8] Z.L. Wang, X. Feng, *The Journal of Physical Chemistry B*, 107 (2003) 13563-13566.

[9] X.D. Zhou, W. Huebner, H.U. Anderson, *Chemistry of Materials*, 15 (2002) 378-382.

[10] P. Bera, A. Gayen, M.S. Hegde, N.P. Lalla, L. Spadaro, F. Frusteri, F. Arena, *The Journal of Physical Chemistry B*, 107 (2003) 6122-6130.

[11] S. Kim, J.S. Lee, C. Mitterbauer, Q.M. Ramasse, M.C. Sarahan, N.D. Browning, H.J. Park, *Chemistry of Materials*, 21 (2009) 1182-1186.

[12] V. Matolín, L. Sedláček, I. Matolínová, F. Šutara, T. Skála, B. Šmíd, J. Libra, V. Nežasil, K.C. Prince, *The Journal of Physical Chemistry C*, 112 (2008) 3751-3758.

[13] F. Yang, Y. Choi, S. Agnoli, P. Liu, D. Stacchiola, J. Hrbek, J.A. Rodriguez, *The Journal of Physical Chemistry C*, 115 (2011) 23062-23066.

[14] B.M. Reddy, A. Khan, Y. Yamada, T. Kobayashi, S. Loricant, J.-C. Volta, *Langmuir*, 19 (2003) 3025-3030.

[15] J.P.Y. Tan, H.R. Tan, C. Boothroyd, Y.L. Foo, C.B. He, M. Lin, *The Journal of Physical Chemistry C*, 115 (2011) 3544-3551.

[16] K. Zhou, Z. Yang, S. Yang, *Chemistry of Materials*, 19 (2007) 1215-1217.

[17] H. Imagawa, A. Suda, K. Yamamura, S. Sun, *The Journal of Physical Chemistry C*, 115 (2011) 1740-1745.

- [18] L. Yan, R. Yu, J. Chen, X. Xing, *Crystal Growth & Design*, 8 (2008) 1474-1477.
- [19] R.K. Pati, I.C. Lee, K.J. Gaskell, S.H. Ehrman, *Langmuir*, 25 (2008) 67-70.
- [20] Z.-L. Wang, G.-R. Li, Y.-N. Ou, Z.-P. Feng, D.-L. Qu, Y.-X. Tong, *The Journal of Physical Chemistry C*, 115 (2010) 351-356.
- [21] Z. Wang, Z. Quan, J. Lin, *Inorganic Chemistry*, 46 (2007) 5237-5242.
- [22] C. Paun, O.V. Safonova, J. Szlachetko, P.M. Abdala, M. Nachtegaal, J. Sa, E. Kleymenov, A. Cervellino, F. Krumeich, J.A. van Bokhoven, *The Journal of Physical Chemistry C*, 116 (2012) 7312-7317.
- [23] M. Jobbágy, F. Mariño, B. Schönbrod, G. Baronetti, M. Laborde, *Chemistry of Materials*, 18 (2006) 1945-1950.
- [24] L. Xu, H. Song, B. Dong, Y. Wang, J. Chen, X. Bai, *Inorganic Chemistry*, 49 (2010) 10590-10597.
- [25] H. Xiao, Z. Ai, L. Zhang, *The Journal of Physical Chemistry C*, 113 (2009) 16625-16630.
- [26] F. Dvořák, O. Stetsovych, M. Steger, E. Cherradi, I. Matolínová, N. Tsud, M. Škoda, T. Skála, J. Mysliveček, V. Matolín, *The Journal of Physical Chemistry C*, 115 (2011) 7496-7503.
- [27] Q. Zhang, B. Xu, S. Yuan, M. Zhang, T. Ohno, *Materials Letters*, 121 (2014) 109-112.
- [28] M.-M. Titirici, M. Antonietti, A. Thomas, *Chemistry of Materials*, 18 (2006) 3808-3812.
- [29] L. González-Rovira, J.M. Sánchez-Amaya, M. López-Haro, E. del Rio, A.B.

- Hungría, P. Midgley, J.J. Calvino, S. Bernal, F.J. Botana, *Nano Letters*, 9 (2009) 1395-1400.
- [30] J. Ciston, R. Si, J.A. Rodriguez, J.C. Hanson, A. Martínez-Arias, M. Fernandez-García, Y. Zhu, *The Journal of Physical Chemistry C*, 115 (2011) 13851-13859.
- [31] F. Zhang, S.-W. Chan, J.E. Spanier, E. Apak, Q. Jin, R.D. Robinson, I.P. Herman, *Cerium oxide nanoparticles: Size-selective formation and structure analysis*, *Applied Physics Letters*, 80 (2002) 127.
- [32] X.D. Zhou, W. Huebner, *Applied Physics Letters*, 79 (2001) 3512.
- [33] H. Li, A. Petz, H. Yan, J.C. Nie, S.n. Kunsági-Máté, *The Journal of Physical Chemistry C*, 115 (2011) 1480-1483.
- [34] Z.D. Dohčević-Mitrovi, M. Grujić-Brojčin, M. Šćepanović, Z.V. Popović, S. Bošković, B. Matović, M. Zinkevich, F. Aldinger, *Condensed Matter*, 18 (2006) S2061-S2068.
- [35] K.C.H. J. R. McBride, B. D. Poindexter, and W. H. Weber, *Journal of Applied Physics*, 76 (1994) 2435.
- [36] Y. Lee, G. He, A.J. Akey, R. Si, M. Flytzani-Stephanopoulos, I.P. Herman, *Journal of the American Chemical Society*, 133 (2011) 12952-12955.
- [37] S. Chang, M. Li, Q. Hua, L. Zhang, Y. Ma, B. Ye, W. Huang, *Journal of Catalysis*, 293 (2012) 195-204.
- [38] H. Rotter, M.V. Landau, M. Carrera, D. Goldfarb, M. Herskowitz, *Applied Catalysis B: Environmental*, 47 (2004) 111-126.

- [39] P. Ji, J. Zhang, F. Chen, M. Anpo, *The Journal of Physical Chemistry C*, 112 (2008) 17809-17813.
- [40] J. Li, G. Lu, H. Li, Y. Wang, Y. Guo, Y. Guo, *Journal of Colloid and Interface Science*, 360 (2011) 93-99.
- [41] S. Guo, H. Arwin, S.N. Jacobsen, K. Jarrendahl, U. Helmersson, *Journal of Applied Physics*, 77 (1995) 5369-5376.
- [42] Y. Park, S.K. Kim, D. Pradhan, Y. Sohn, *Chemical Engineering Journal*, 250 (2014) 25-34.
- [43] C. Karunakaran, P. Gomathisankar, *ACS Sustainable Chemistry & Engineering*, 1 (2013) 1555-1563.
- [44] J. Wang, D.N. Tafen, J.P. Lewis, Z. Hong, A. Manivannan, M. Zhi, M. Li, N. Wu, *Journal of the American Chemical Society*, 131 (2009) 12290-12297.
- [45] B. Choudhury, A. Choudhury, *Materials Chemistry and Physics*, 131 (2012) 666-671.
- [46] P. Patsalas, S. Logothetidis, C. Metaxa, *Applied Physics Letters*, 81 (2002) 466.
- [47] B. Tatar, E.D. Sam, K. Kutlu, M. Ürgen, *Journal of Materials Science*, 43 (2008) 5102-5108.
- [48] Y.V.f. Holger Borchert, Vasiliy V.Kaichev, Igor P.Prosvirin, *J.phys. chem.B*, 109 (2005) 5728-5738.
- [49] L. Ma, D. Wang, J. Li, B. Bai, L. Fu, Y. Li, *Applied Catalysis B: Environmental*, 148-149 (2014) 36-43.
- [50] N. Imanaka, T. Masui, K. Minami, K. Koyabu, *Chemistry of Materials*, 17 (2005)

6511-6513.

[51] H. Zhu, Z. Qin, W. Shan, W. Shen, J. Wang, *Journal of Catalysis*, 225 (2004) 267-277.

[52] P.X. Huang, F. Wu, B.L. Zhu, X.P. Gao, H.Y. Zhu, T.Y. Yan, W.P. Huang, S.H. Wu, D.Y. Song, *The Journal of Physical Chemistry B*, 109 (2005) 19169-19174.

[53] M. Lin, Z.Y. Fu, H.R. Tan, J.P.Y. Tan, S.C. Ng, E. Teo, *Crystal Growth & Design*, 12 (2012) 3296-3303.

[54] G. Chen, C. Xu, X. Song, S. Xu, Y. Ding, S. Sun, *Crystal Growth & Design*, 8 (2008) 4449-4453.

Chapter 2

Synthesis and Photocatalytic Performance of Yttrium-doped CeO₂ with a Porous Broom-like Hierarchical Structure

1. Introduction

Cerium dioxide, an important rare-earth oxide, has been extensively studied due to its significant fluorite-type structure, remarkable redox properties [1-3] and prominent oxygen storage and release capacity (OSC) via facile conversion between Ce^{4+} and Ce^{3+} oxidation states [2]. Ceria-based materials have been extensively utilized in many practical applications such as polishing materials [3], solar cells [4], ultraviolet blocking materials [5, 6] and photocatalytic materials. Pure CeO_2 , an n-type semiconductor, has a band gap (3.2eV) similar to those of other commonly utilized semiconductor-based photocatalysts such as TiO_2 [7] and possesses potential as a suitable photocatalyst. Recently, CeO_2 materials with different morphologies have been synthesized by various methods including thermal evaporation [8], coprecipitation [9], and the sol-gel technique [10]. Previous studies have indicated that excellent catalytical performance and easy functionalization of CeO_2 materials can be achieved by controlling their structural properties [11]. For instance, our group had successfully fabricated porous broom-like CeO_2 [12] and CeO_2 with an yttrium-doped hedgehog-like 3D hierarchical structure [13]. Compared with conventional nanowires, nanorods and nanocubes as well as nanoparticles with other shapes, newly constructed CeO_2 with a hierarchical architecture will acquire some special properties that single morphology CeO_2 does not possess [10, 14, 15]. Although some progress has been made in the fabrication of hierarchical architectures composed of 1D nanostructures, the methods usually need special templates through a complex experimental course. For example, Sam L. Mitchell et al. fabricated

coral-like mesostructured CeO₂ using an amino acid as a template [16]. Zhong et al. reported the preparation of 3D flowerlike ceria at 180 °C with TBAB as a surfactant and EG as a solvent [17].

The application of morphology and size-controlled, metal and metal oxide composites and different ionic doping are the three most commonly utilized methods for enhancing the photocatalytic properties of CeO₂-based materials. The keypoint in these approaches is changing the oxygen vacancy concentrations of products, because oxygen vacancies can act as electron or hole capture centers and can trap the photogenerated electrons or holes excited by ultraviolet or visible light. Oxygen vacancies can also effectively restrain the recombination of electron-hole pairs, resulting in improvement of photocatalytic activities [18]. Application of more than two or all of the above methods to the preparation of a 3D hierarchical structure of CeO₂ with a high concentration of oxygen vacancies would be a huge challenge. To the best of our knowledge, there has been no report about CeO₂ with an yttrium-doped hierarchical structure obtained by facile controlled synthesis.

Herein, we report for the first time a facile and feasible approach to prepare porous CeO₂ with a yttrium-doped broom-like hierarchical structure by a simple template-free hydrothermal technique using the simple inorganic salts Ce(NO₃)₃, Y(NO₃)₃ and the morphology-decorated agent dihydrate trisodium citrate(C₆H₅Na₃O₇·2H₂O) as original materials. Changes in the concentration of oxygen vacancies, active oxygen species on the crystal surface and tervalence cerium in the lattice, caused by variation in the amount of the yttrium dopant, are discussed in

detail in this article. Meanwhile, the corresponding photocatalytic performance was characterized by TPR, TPD and photocatalytic decomposition of acetaldehyde exhaustively.

2. Experiment section

2.1 Materials

Dihydrate trisodium citrate ($C_6H_5Na_3O_7 \cdot 2H_2O$), urea, cerium nitrate hexahydrate ($Ce(NO_3)_3 \cdot 6H_2O$) and yttrium nitrate hexahydrate ($Y(NO_3)_3 \cdot 6H_2O$) were of analytical grade and used without any further purification. All of the above original materials were purchased from Wako Co., Ltd.

2.2 Preparation

A typical synthetic procedure is as follows, and the optimal synthesis conditions were described in our first part [12]. First, 5.88 g dihydrate trisodium citrate ($C_6H_5Na_3O_7 \cdot 2H_2O$) was dissolved in 80 ml deionized water with vigorous magnetic stirring at room temperature. Ten minutes later, 2.4 g urea was added to the solution. The homogeneous mixture was prepared for further use. At the same time, 1.63 g cerium nitrate hexahydrate ($Ce(NO_3)_3 \cdot 6H_2O$) and 0.072 g, 0.144 g, 0.288 g, 0.432 g or 0.575 g yttrium nitrate hexahydrate were dissolved in 20 ml deionized water with vigorous magnetic stirring at room temperature. Then each of these cerium and yttrium nitrate aqueous solutions was dropped into the above mixture at 1 ml/min, and the mixture was stirred for 30 min until the solution changed to a faint yellow

color. The mixed solution was then sealed in a 100 ml Teflon-lined autoclave and heated at 120 °C for 39 hours. After cooling to room temperature naturally, a white precipitate was collected by centrifugation and washed with deionized water and ethanol respectively at least three times. Yttrium-doped ceria was obtained by calcination of the as-prepared precursor in air at 500 °C for 4 h.

2.3 Characterizations

Morphology and size of the products were observed by an FE-SEM (Hitachi, S-4800, 15KV) and element and distribution HR-TEM (FEI, Tecnai G2 F30 S-TWIN, 300KV). XRD patterns of the products were obtained on a Bruker-AXS X-ray equipped with graphite monochromator and CuK α radiation ($\lambda=1.5406 \text{ \AA}$). The crystallite parameters and size were calculated by the Rietveld method (TOPAS 4.0). Raman analysis (Renishaw, In via) was performed using a 532 nm excitation laser with 5 mW and an air-cooled CCD detector. Raman peak shifts were determined by fitting with the Lorentzian and Gaussian composite function. An x-ray photoelectron spectroscopy (XPS) experiment was carried on a Shimadzu KRATOS AXIS-NOVA system at room temperature under 10^{-9} pa using Al K α radiation and C 1s peak (83.8 eV) reference. Hydrogen temperature-programmed reduction (H $_2$ -TPR) and oxygen temperature-programmed decomposition (O $_2$ -TPD) experiments were performed on FTNESORB-3010. In each of the experiments, 500 mg was pretreated by calcination at 200 °C for 1 hour and was subsequently cooled to 100 °C under an Ar flow before being used. For the H $_2$ -TPR experiment, the reduction process was carried out from

room temperature to 900 °C under a flow of 10% H₂ /Ar with 50 cm³/min. For the O₂-TPR experiment, the adsorption of O₂ was carried out in a flow of 10% O₂/ He for 1 hour, followed by purging by He for 30 min for removal of residual oxygen. The consumption of H₂ or O₂ was continuously monitored by a thermal conductivity detector (TCD) operating at 60 °C and 80 mA.

2.4 Photocatalytic Evaluations.

UV lighter using black light (UVP, XX-15BLB) can be used in order to remove possible organic materials adsorbed on the surface of samples more than one week before evaluation of photocatalytic activity. The photocatalytic activity of as-fabricated samples was assessed by ability for decomposition of acetaldehyde. And the analytic instruments are show in the Fig 1. Ten milligrams of powder was spread on the bottom of a glass dish, and the glass dish was placed in a Tedlar bag (AS ONE Co. Ltd.). Five hundred ppm of acetaldehyde was injected into the bag together with 125 cm³ of artificial air. Then the bag, which was fabricated above, was put into a dark place at room temperature for 2 hours for the purpose of reaching an adsorption equilibrium A light-emitting diode (LED; Epitex, L365), which emitted light at wavelengths of ca. 365 nm, was used as a light source, and its intensity was controlled at 0.9 mW cm⁻². The reaction equilibrium is showed at formular 1. The concentration of generated CO₂ as s function of irradiation time was monitored by a gas chromatography (Shimadzu GC-8A, FID detector) equipped with a Porapak N-packed column and a methanizer (GL Science, MT-221).

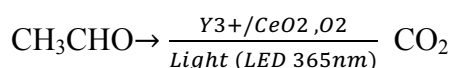
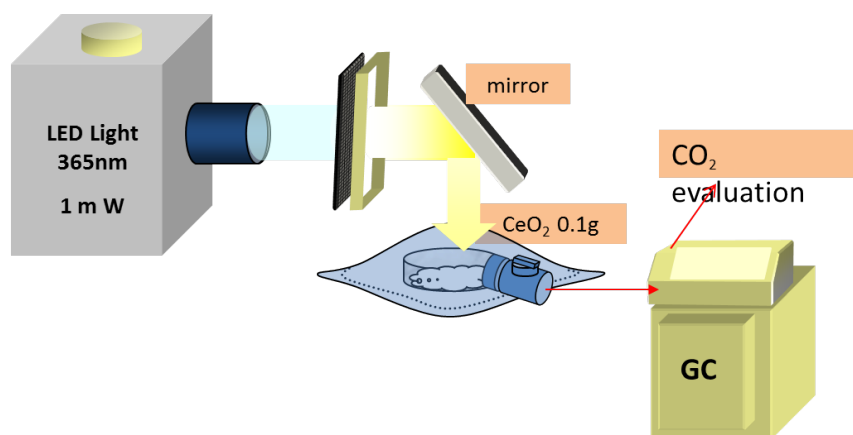


Fig 1: Photocatalytic measurement instrument Schematic diagram

3. Results and discussion

3.1 Morphology characterization

The morphology of as-prepared CeO_2 with different yttrium-doped concentrations was investigated by using an FE-SEM (Fig. 2) and HR-TEM (Fig. 4). Fig. 2a shows broom-like morphology CeO_2 without yttrium doping. Numerous nanorods of approximately 10 μm in length and with an average diameter of 500 nm are connected at one end and diverge at the other end to form a broom-like hierarchical architecture. Fig. 4a shows that numerous inhomogeneous ceria nanoparticles with an average range of 20 nm in diameters have loosely accumulated to form a porous broom-like morphology. Evidently, the size of these particles is inhomogeneous, and the maximum particle size may reach 40 nm while the smallest diameter is only about 10 nm. The corresponding elemental maps of products show that only Ce and O are obviously detected and well distributed throughout the individual nanorods (Fig. 3). Furthermore, the d lattice spacing calculated from the

inset image of Fig. 2a is 0.313 nm, indicating that these nanoparticles mainly expose (111) planes of a cubic fluorite structure of CeO_2 .

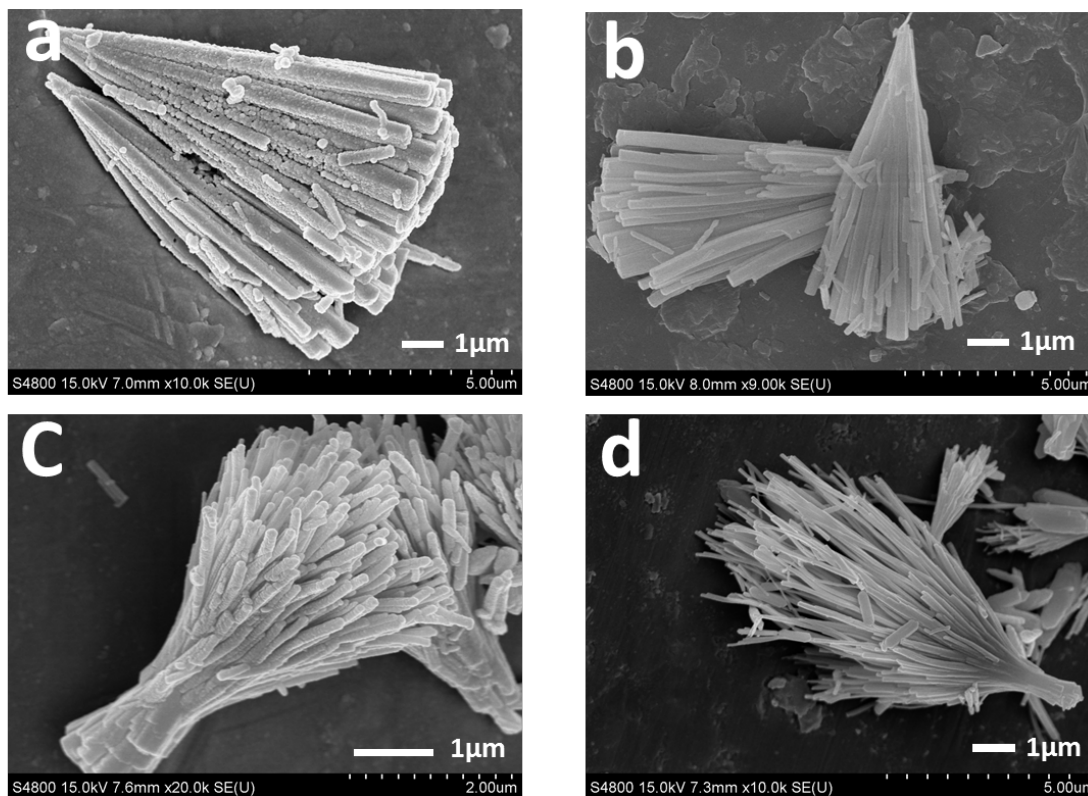


Fig. 2: FESEM images of as-fabricated samples with different mole ratios of $\text{Ce}(\text{NO}_3)_3 \cdot 6\text{H}_2\text{O} : \text{Y}(\text{NO}_3)_3 \cdot 6\text{H}_2\text{O}$: (a) 1:0, (b) 1:0.1, (c) 1:0.2 and (d) 1:0.4.

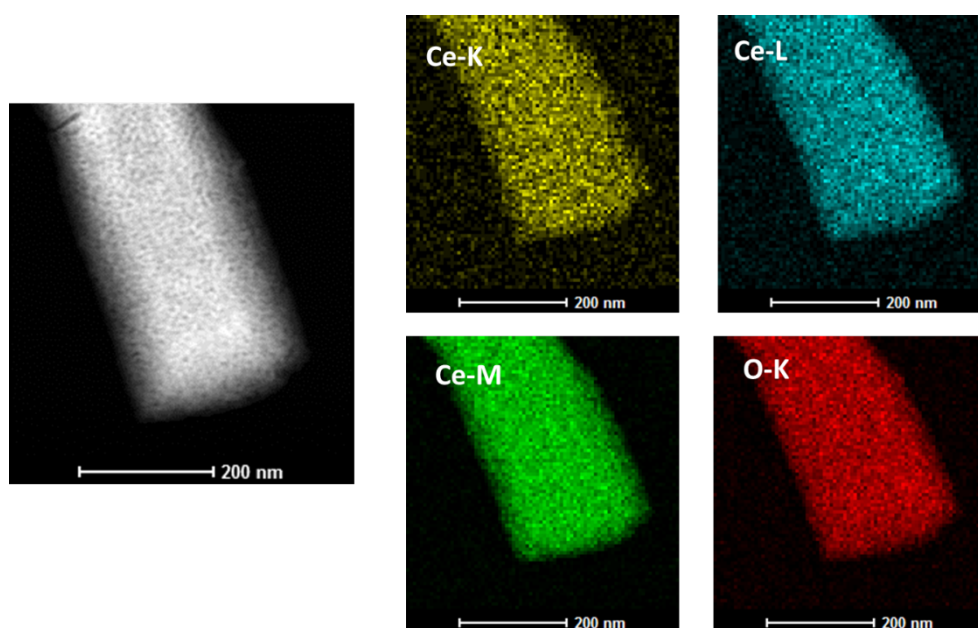


Fig. 3: HAADF image and distribution of element maps of Ce-K (yellow), Ce-L (skyblue), Ce-M (green), and O-K (red) before doping.

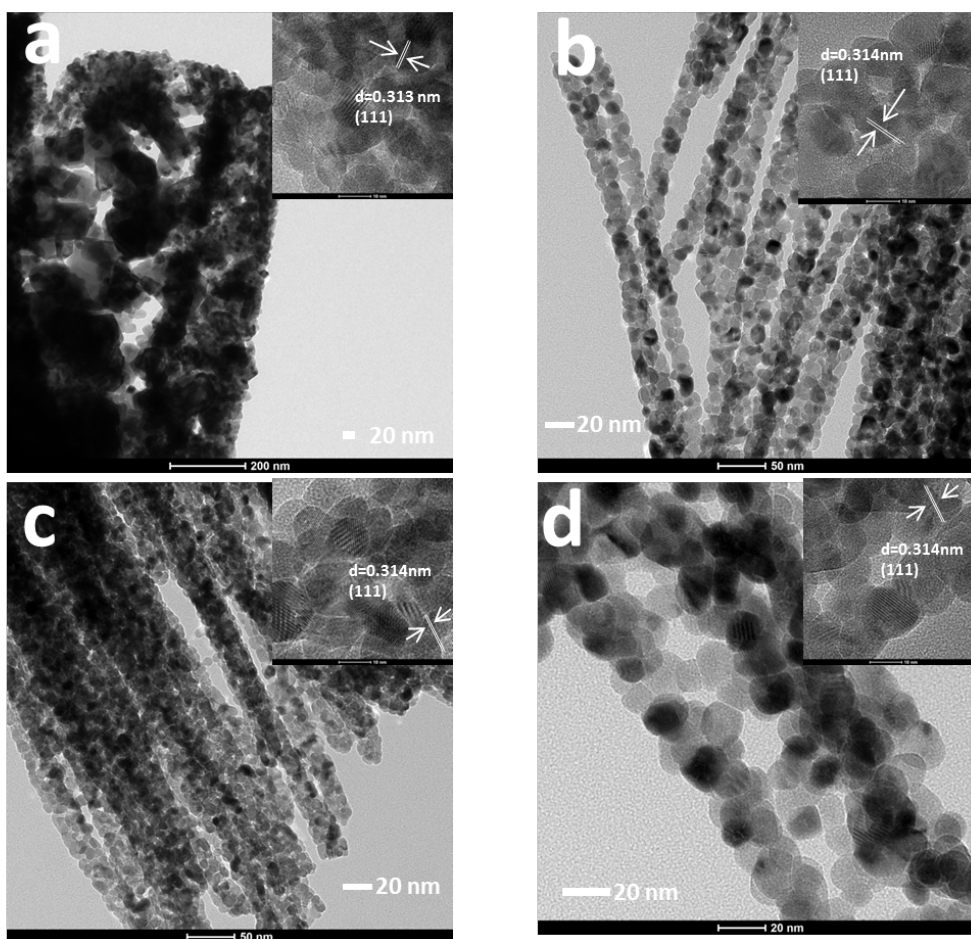


Fig. 4: HRTEM images of as-fabricated samples with different mole ratios of $\text{Ce}(\text{NO}_3)_3 \cdot 6\text{H}_2\text{O}$: $\text{Y}(\text{NO}_3)_3 \cdot 6\text{H}_2\text{O}$: (a) 1:0, (b) 1:0.1, (c) 1:0.2 and (d) 1:0.4.

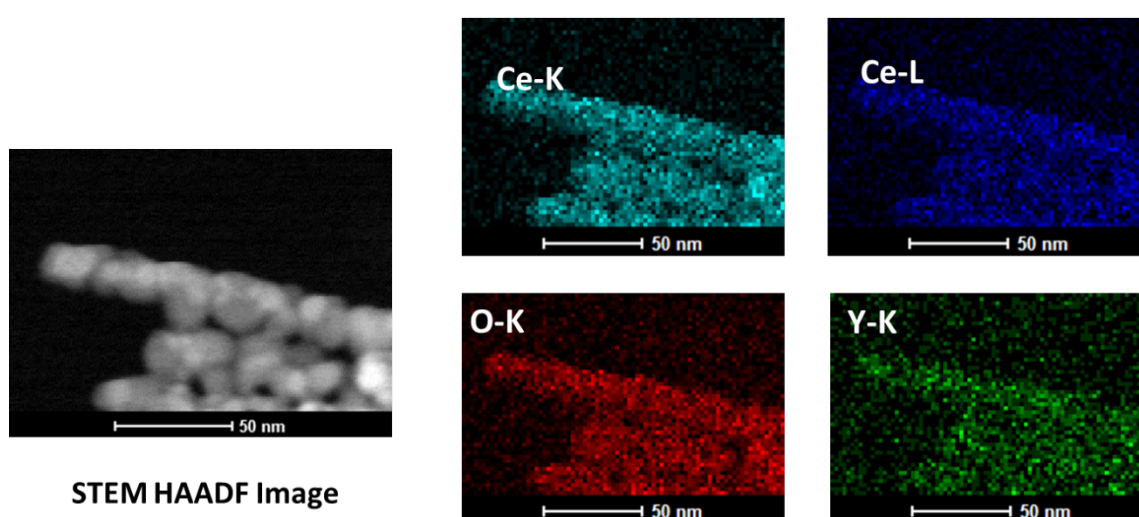


Fig. 5: HAADF image and distribution of element maps of Ce-K (skyblue), Ce-L (blue), O-K (red), and Y-K (green) after doping.

Fig. 2b~2d show broom-like morphology of CeO₂ with yttrium doping. After doping, the morphology of the products does not change remarkably and the broom-like shape is maintained. Only changes in the surface smooth degree, averaged diameter, and length of the nanorods can be observed. With an increase in the amount of the yttrium dopant, the surface smooth degree of nanorods was obviously improved. At the same time, the length of the rods increased correspondingly. In contrast, the average diameter of the nanorods decreased greatly from 500 nm to 200 nm. Similar phenomena can be seen in the Fig. 4b~4d. Numerous yttrium-doped ceria nanoparticles loosely accumulated to form a porous broom-like morphology. However, unlike before doping, the particles sizes after doping are uniform and the average diameter is about 10 nm. As can be seen in the respective inset images, although the particles still mainly expose a (111) lattice plane of the FCC structure, the internal spacing distance increased to 0.314 nm. Fig. 5 shows corresponding elemental maps of products after yttrium doping. Not only cerium and oxygen but also yttrium are observed together, and all of these elements are well distributed throughout individual nanorods. Elemental distribution and internal spacing distance changing suggest that yttrium has entered the lattice structure of CeO₂ and that doping is successful.

3.2 Structure characterization

X-ray diffractometer (XRD) analysis was carried out to investigate the crystal phase and purity of samples obtained with different yttrium-doped concentrations.

Typical XRD patterns are shown in Fig. 6a. All of the diffraction lines could be

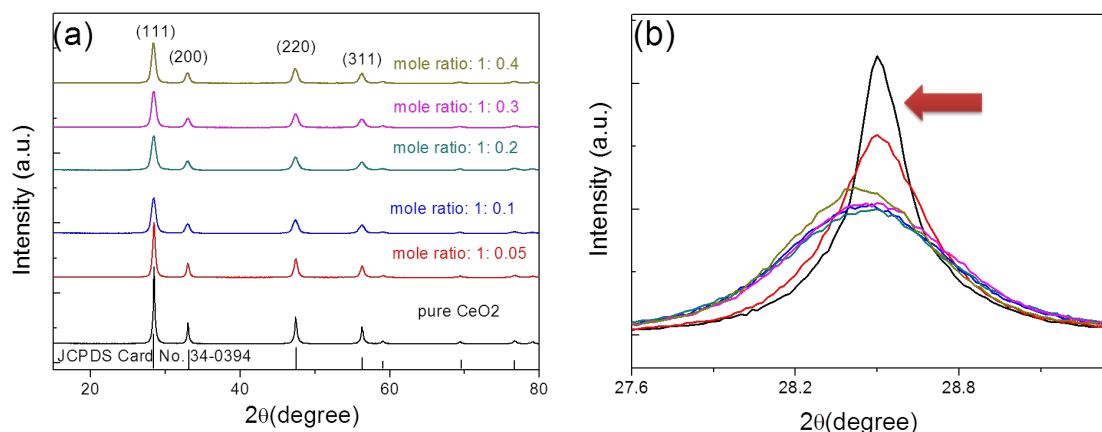


Fig. 6: XRD pattern of as-fabricated samples with different mole ratios of $\text{Ce}(\text{NO}_3)_3 \cdot 6\text{H}_2\text{O} : \text{Y}(\text{NO}_3)_3 \cdot 6\text{H}_2\text{O}$: (a) whole range and (b) elaborated XRD pattern of the highest peak (111).

indexed to the phase of ceria with a cubic fluorite structure (Space group: Fm-3m (225)), being in good agreement with the standard data reported in JCPDS card (No. 34-0394). The sharp diffraction peaks from all samples suggest a high degree of crystallinity of fabricated samples, and no impurity peaks appeared, indicating that the concentration of the dopant has no effect on crystalline phase purity of the products. The relative intensity between characteristic peaks at about 28.5, 33.0 47.4 and 56.3 2θ does not change clearly, which assigned to the crystal planes (111), (200), (220) and (311) respectively, suggesting that there is no preferred orientation or orientation crystal growth. The elaborated XRD pattern of the highest peak (Fig. 6b) reveals that, compared with pure ceria, the highest peak position (111) of the products exhibited an obvious shift to a lower angle after yttrium doping and reached about 28.41° (2θ), indicating that crystal lattice has expanded conspicuously due to the entry of yttrium into the crystal structure. At the same time the value of full width at half maximum (FWHM) located at 28.45° became larger, demonstrating that crystal size of samples

doped by yttrium decreased.

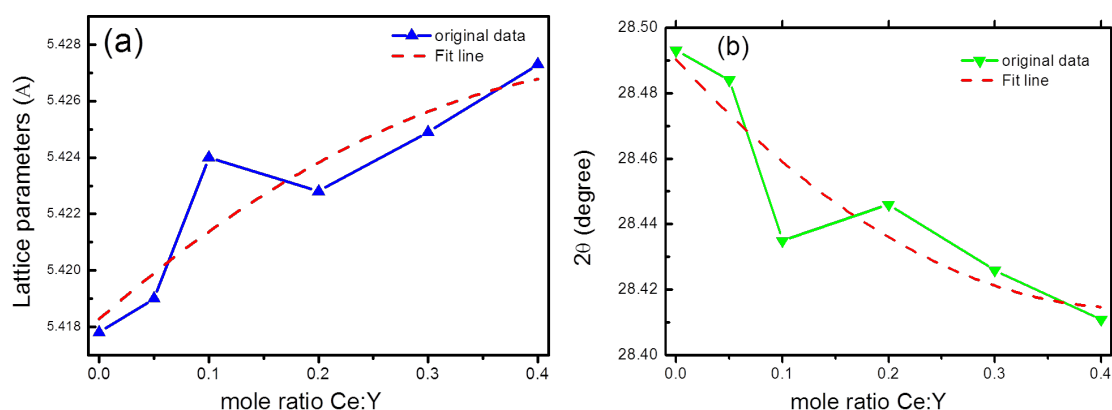


Fig. 7: Rietveld refined data for (a) lattice parameters and (b) highest peak position as function of a dopant mole ratio.

Rietveld refinements were also carried out according to the diffraction lines by varying parameters in order to investigate the actual doping quantity and location (Fig. 8). As is well known, in the cubic fluorite structure of cerium dioxide, each cerium is arranged in the face-centered cubic surrounded by eight oxygen elements. Meanwhile, oxygen elements occupied all of the tetrahedral positions and each oxygen element has four ligancy of cerium cations. Therefore, more oxygen vacancies would consequently emerge after yttrium enters the crystal lattice. When the amount of the dopant was changed without changing the other experimental conditions, there were significant changes in the lattice parameters. The lattice parameter value (a) changed from 5.4190 to 5.4273 Å (see the Table 1). It can be clearly seen that the lattice parameter value (a) after doping is larger than the bulk CeO₂ lattice parameter value $a=5.4178$ Å even though the space group is still Fm-3m before and after doping. This indicates that yttrium has partially substituted cerium ions and has been introduced into the interior lattice, maintaining the ceria cubic fluorite structure instead of forming Y₂O₃-CeO₂ composite. In addition, a linear relationship could be drawn

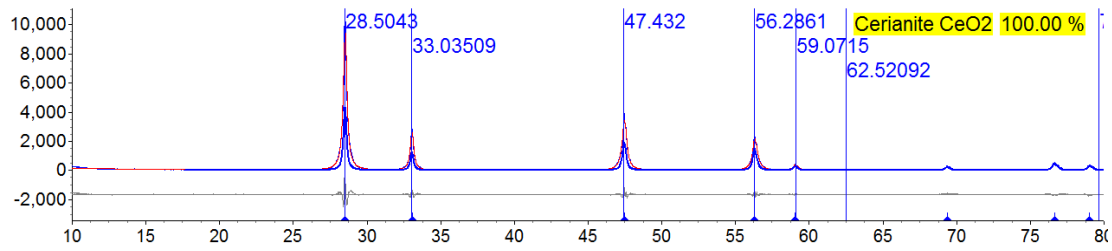


Fig. 8: Rietveld refined curve of products.

between the lattice value, (111) crystal plane peak position and amount of doping (see Fig. 7a and 7b). Lattice parameters clearly increased and the highest peak position decreased notably accompanied by an increasing amount of the dopant and finally reached a relative equilibrium. In other words, the amount of dopant plays a definitive role in determining ceria lattice parameters. Yttrium enters the crystal lattice and cerium ions of the crystal lattice are substituted by yttrium. Consequently, the crystal lattice would expand due to an increase in oxygen vacancy concentration with an increase in yttrium content, attributed to the fact that the ionic radius of yttrium is larger than that of cerium (1.019 and 0.97 Å, respectively). Particle sizes (D) of as-fabricated samples were also obtained by Whole Pattern Profile fitting instead of single peak refinement (Scherrer's formula). D values are randomly distributed about 10 nm after doping. The D value after doping is smaller than before doping (40 nm), and calculated results are extremely consistent with HR-TEM observations. A comparison of our results with those of previous studies [8, 19, 20] led to the following conclusion. Although changes in particle size resulted in crystal lattice expansion [21,22] or contraction of CeO₂, the effects would become weaker after yttrium doping. The type and concentration of dopant play the role in the governing the lattice expansion or contraction of crystal parameters.

Raman technology is considered to be a very efficient and nondestructive technique for characterization of ceria nanoparticles and their derivatives. Raman spectra of as-fabricated samples under various experimental conditions are shown in Fig. 9(a).

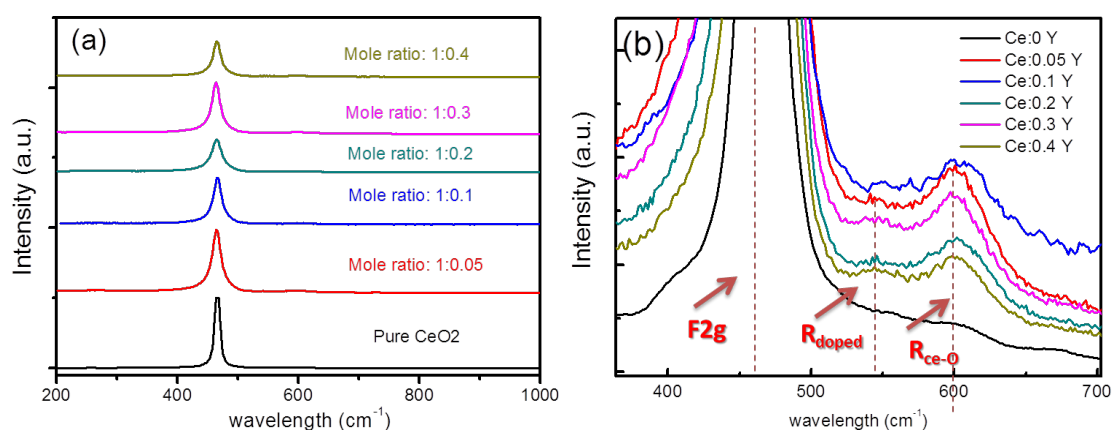


Fig. 9: Raman spectra of as-fabricated samples with different mole ratios of $\text{Ce}(\text{NO}_3)_3 \cdot 6\text{H}_2\text{O} : \text{Y}(\text{NO}_3)_3 \cdot 6\text{H}_2\text{O}$: (a) whole range and (b) elaborated Raman shift.

A strong Raman shift at $\sim 460 \text{ cm}^{-1}$ and a relatively weak shift at $\sim 600 \text{ cm}^{-1}$ can be detected. The shift at $\sim 460 \text{ cm}^{-1}$ can be assigned to F2g vibration of the fluorite-type structure and it can be considered as the symmetric stretching mode of oxygen atoms around cerium ions, and the molecule retains its tetrahedral symmetry throughout. Based on the results of previous studies [23,24] and our own studies [12,13], a weak and less prominent band near $\sim 600 \text{ cm}^{-1}$ can be attributed to a nondegenerate longitudinal optical mode caused by a local Ce-O ($R_{\text{Ce-O}}$) bond symmetry stretch [25,26]. According to the results of previous studied showing that not all cerium ions show Ce^{4+} chemical valence in the lattice, small cerium ions show Ce^{3+} tervalence [27,28]. In order to maintain the particles in an electrically neutral state, the lattice oxygen would escape from the structure and finally result in the formation of intrinsic

oxygen vacancies. A new and weak Raman shift at $\sim 530 \text{ cm}^{-1}$, which cannot be detected in Raman spectra of pure CeO_2 , can be seen in Fig. 9 (b). It is attributed to extrinsic oxygen vacancies caused by doping (R_{dopant}). As a dopant, yttrium enters the cubic fluorite lattice of CeO_2 , and cerium is substituted by yttrium. In order to maintain electronic neutrality, doping cations showing different valence states with Ce^{4+} and part of the oxygen would also escape from the lattice to form extrinsic oxygen vacancies. The relativity intensities of Raman shifts of F2g , R_{dopant} and $R_{\text{Ce-O}}$ can be calculated from equation (1) [29]:

$$\frac{\text{Oxygen vacancies}}{F2g} = \frac{(A_{\text{era}R_{\text{Ce-O}}} + A_{\text{era}R_{\text{dopant}}})}{A_{\text{era}F2g}} \quad (1)$$

Samples/ different mole ratio	Lattice parameters (a)	Calculated grain size (nm)	R_{wp}	Particles size (nm)	Area _{Oxygen vacancies} /Area _{F2g} (%)
Pure CeO2	5.4178	4.50	5.86	~10	6.8
1 : 0.05	5.4190	4.6	5.26	~10	10.9
1 : 0.1	5.4240	4.52	5.76	~10	11.2
1 : 0.2	5.4228	4.54	5.05	~10	10.2
1 : 0.3	5.4249	4.6	4.87	~10	10.5
1 : 0.4	5.4273	4.63	5.62	~10	10.3

PS: $\text{Area}_{\text{Oxygen vacancies}} / \text{Area}_{F2g} (\%) = (\text{Area}_{R_{\text{doped}}} + \text{Area}_{R_{\text{Ce-O}}}) / \text{Area}_{F2g} (\%)$

Table.1: Rietveld refined data from XRD patterns and oxygen vacancy value calculated by Raman spectra.

The values are shown in Table 1, It can be seen that the value of oxygen vacancies rapidly increased at first compared with pure CeO_2 after yttrium doping. When the mole ratio of Ce:Y reached 1:0.1, the value of oxygen vacancies reached a

maximum 11.2%. Finally, the value decreased and reached an approximate balance with further increase in the dopant content. The trend for change in the value can be attributed to the amount of the dopant. At the beginning, yttrium was introduced into bulk CeO₂, and more extrinsic oxygen vacancies were obtained except intrinsic oxygen vacancies. Therefore, the value of oxygen vacancies rapidly increased. When an excessive amount of the dopants was added, the oxygen vacancy concentration increased and eventually reached a steady plateau level in order to maintain electron neutrality of the system. These results of Raman analysis are consistent with the results of XPS O_{1s} analysis and activity evaluation.

3.3 X-ray photoelectron spectroscopy characterization

XPS characterization was applied to determine the CeO₂ nanoparticles before and after yttrium doping. Wide scanning XPS spectra of the product is illustrated in Fig. 7. The elements Ce, O, and C can be detected from Fig. 10(a), and they are assigned to Ce3d, O1s and C1s binding energies, respectively. Not only above elements but also yttrium element can be detected from the spectra, and it is assigned to Y3d binding energy, indicating that doping was successful (Fig. 10(b)). The elaborated Y3d XPS spectra of the products after doping are shown in Fig. 11. After deconvolution and separation, two peaks located at 156.1ev and 158.2ev, assigned to Y3d_{5/2} binding energy, can be founded from XPS profiles (Fig. 11(a)). Fig. 11(b) shows, after calculated these two peaks area, peak intensity and area persistent enhanced accompanied with increasing concentration dopant, indicating that more

yttrium enters into the lattice of ceria with increasing dopant concentration. This result is in agreement with the results of XRD and Raman analysis.

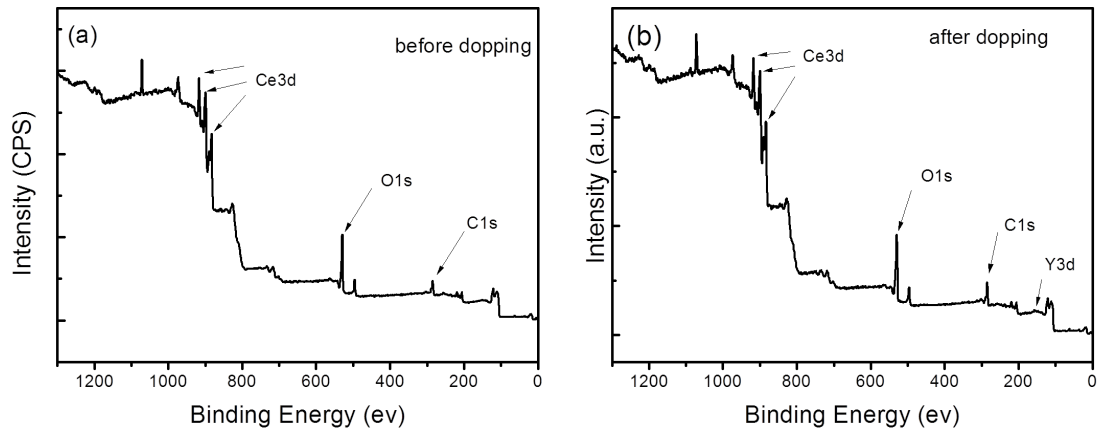


Fig. 10: Wide scanning XPS spectra of products (a) before doping and (b) after doping.

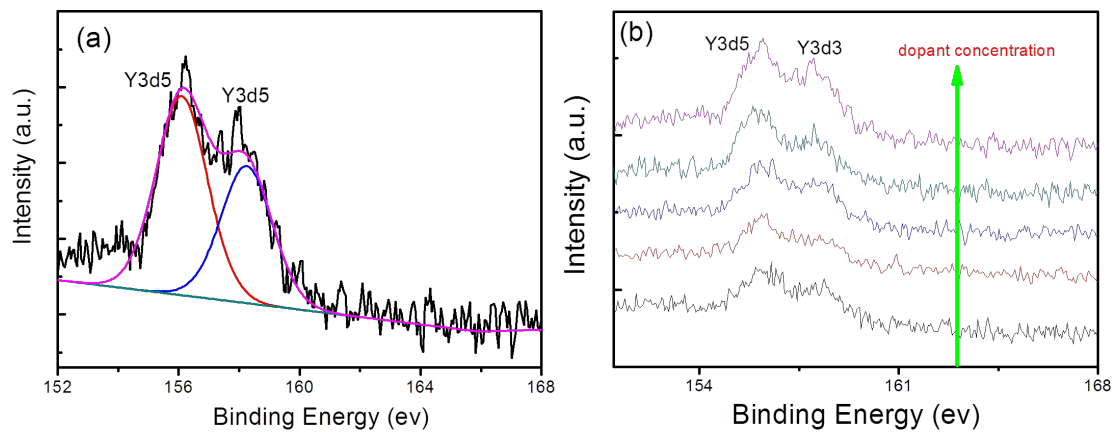


Fig. 11: High-resolution XPS spectra of Y3d (a) separated peak curve and (b) different mole ratio products.

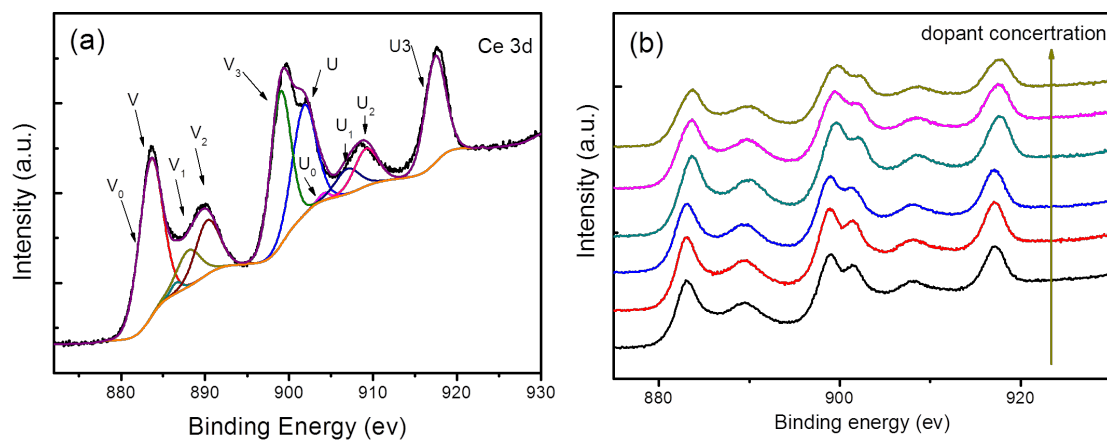


Fig. 12: High-resolution XPS spectra of Ce3d (a) separated peak curve and (b) different mole ratio products.

Fig. 12 shows Ce 3d electron core level XPS spectra for as-fabricated samples and the changes in Ce 3d_{3/2} and Ce 3d_{5/2} components depending on the Ce³⁺ and Ce⁴⁺ oxidation states. Five pairs of doublets, (u, v), (u₁, v₁), (u₂, v₂), (u₃, v₃) and (u₀, v₀), can be decomposed from the origin region, where u and v come from Ce 3d_{3/2} and Ce 3d_{5/2} states, respectively. We observed that (u, v), (u₂, v₂) and (u₃, v₃), which were attributed to Ce 3d₉ 4f₂ O 2p₄, Ce 3d₉ 4f₁ O 2p₅ and Ce 3d₉ 4f₀ O 2p₆ final states, respectively, all belonged to the Ce⁴⁺ oxidation state. The two pairs doublets as (u₁, v₁) and (u₀, v₀) originated from the Ce 3d₉ 4f₁ O 2p₄ and Ce 3d₉ 4f₁ O 2p₅ final states, respectively, which correspond to the Ce³⁺ oxidation state (Fig. 9(a)). The relative amount of cerium in the trivalent oxidation state can be calculated from equation (2)[30]:

$$\frac{[\text{Ce}^{3+}]}{[\text{Ce}^{3+}+\text{Ce}^{4+}]} = \frac{\text{area}(V_0, V_1, U_0, U_1)}{\text{total area}}. \quad (2)$$

Results for oxidation states are summarized in Table 2. The fitting data demonstrated that the as-fabricated samples for different dopants (Fig. 12(b)) exhibit variation of [Ce³⁺] concentration. The [Ce³⁺] concentration after doping was larger than that without doping, and when the mole ratio value reached 1:0.1, the [Ce³⁺] concentration reached a peak value of 29.76%. Then the [Ce³⁺] concentration decreased and finally reached an approximate balance.

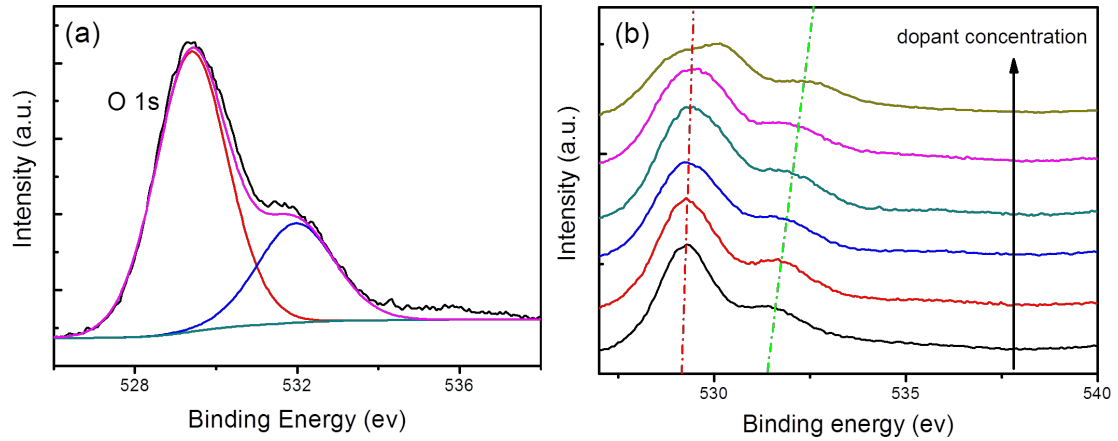


Fig. 13: High-resolution XPS spectra of O1s (a) separated peak curve and (b) different mole ratio products.

Fig. 13 shows O1s electron core level XPS spectra. One peak around 529.0 eV with a shoulder around 531.5 eV can be clearly seen from Fig. 13(a), and they can be attributed to lattice oxygen (O_{lat}) and surface active oxygen (O_{sur}), respectively [29,31]. Fig. 13(b) clearly demonstrates that the O_{lat} and O_{sur} binding energy obviously shifted to a high energy after yttrium doping, while the effects on O_{lat} and O_{sur} are different. The O_{sur} 's binding energy value shows a change of 1.2 eV from 531.3 eV to 532.5 eV with the increase in the amount of dopant. However, the O_{lat} 's binding energy value shows a change of 0.2 eV only from 529.33 eV to 529.53 eV. Therefore, doping of yttrium mainly affects the ceria's surface oxygen binding energy, improving the surface oxygen binding energy and enhancing the activity of surface oxygen [32]. After deconvolution and multiple-peak separation, we could obtain the surface oxygen ratio from the equation (3):

$$\frac{[O_{sur}]}{[O_{sur}+O_{lat}]} = \frac{\text{area}(O_{sur})}{\text{total area}} \quad (3)$$

Sample/different mole ratio of Ce and Y	[Ce ³⁺]/[Ce ³⁺ +Ce ⁴⁺] %	[O _{sur}]/[O _{sur} +O _{lat}] %
Pure CeO ₂	19.0	40.5
1: 0.05	25.38	52.8
1: 0.1	29.76	55.8
1: 0.2	23.43	52.76
1: 0.3	24.00	53.59
1: 0.4	23.86	53.97

$$\frac{[\text{Ce}^{3+}]}{[\text{Ce}^{3+} + \text{Ce}^{4+}]} = \frac{\text{area}(V_0, V_1, U_0, U_1)}{\text{total area}} \quad \frac{[\text{O}_{\text{sur}}]}{[\text{O}_{\text{sur}} + \text{O}_{\text{lat}}]} = \frac{\text{area}(\text{O}_{\text{sur}})}{\text{total area}}$$

Table.2: Calculated [Ce³⁺] and [O_{sur}] concentrations of as-fabricated samples from the XPS spectrum.

Results for surface active oxygen are summarized in Table 2. A trend similar to that for the variation of [Ce³⁺] concentration can be seen. The [O_{sur}] concentration after doping is larger than that without doping, and the maximum value of surface oxygen ratio is approximately 55.8% when the mole ratio value is 1:0.1. This value is higher than the others. In the following process, the [O_{sur}] concentration would reach an approximate equilibrium, although the amount of yttrium is increasing.

The [Ce³⁺] and [O_{sur}] concentrations value of the products can directly reflect the amount and active of oxygen vacancies and suggest that yttrium-doped CeO₂ with a porous broom-like structure should have higher catalytic activity [49]. This result is well consistent with the results of H₂-TPR, O₂-TPD characterization and Raman analysis.

3.4 H₂-TPR characterization

Hydrogen temperature-programmed reduction (H₂-TPR) in a flow of hydrogen up to 900 °C was used to characterize the catalysts and probe redox properties. Fig. 11 shows H₂-TPR traces of as-fabricated samples before and after doping. In the temperature range of 50-900 °C, pure CeO₂ shows two notable reduction peaks at about 440 °C and 766 °C, respectively. The lower temperature reduction peak could be attributed to reduction of surface active oxygen of ceria, while the peak at a higher temperature could be assigned to reduction of lattice oxygen of ceria [33-34, 39].

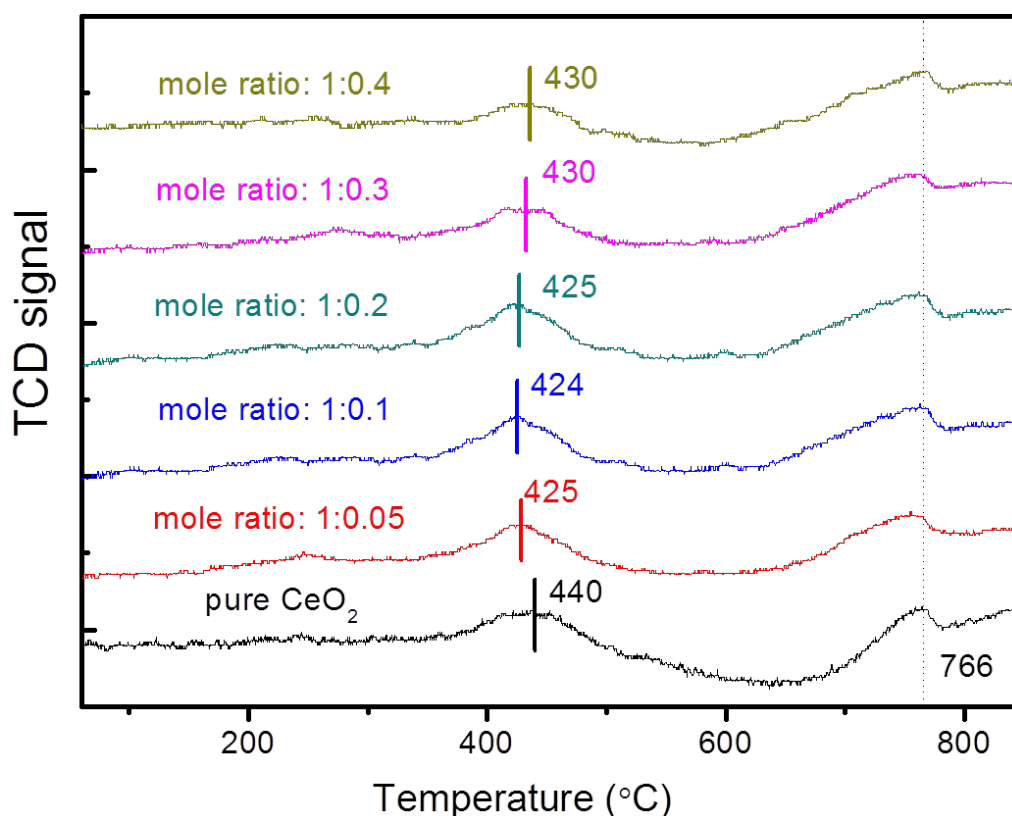


Fig. 14: H₂-TPR profiles of as-fabricated samples with different mole ratios of Ce(NO₃)₃·6H₂O:Y(NO₃)₃·6H₂O.

The relatively moderate shift (~10 °C) of the main reduction peak after yttrium doping to a low temperature (ca. 425 °C), relative to the profile of pure ceria, implies

that the reducibility of the sample fabricated have been considerably enhanced, because the surface active oxygen reducibility is improved after yttrium doping. A trend for enhancement of reduction ability accompanied by variation of yttrium doping concentration can be clearly seen in the H₂-TPR profiles. First, the reduction peak shifts to a low temperature from 425 to 424 °C with increase in the concentration of the dopant at a low mole ratio (below 1:0.1). When the mole ratio is 1:0.1, the reduction temperature is lowest (424 °C). With further increase in the concentration of the dopant (up to mole ratio 1:0.1), the reduction peak draw back slightly to 430 °C. Despite increase in reduction temperature, this value is still lower than that of pure ceria (440 °C). However, the reduction peak positions of lattice oxygen of ceria do not show a significant difference before and after doping and are located stably at about 766 °C, indicating that yttrium doping mainly affected the surface oxygen active species rather than lattice oxygen. These phenomena suggest that yttrium-doped ceria with a porous broom-like structure has predominant catalytic properties, attributing to a certain amount of yttrium would increase the concentration of surface active oxygen and promote surface active oxygen reducibility.

3.5 O₂-TPD characterization

According to previous reports, surface active oxygen species such as O₂⁻ and O⁻ desorbed around 250 °C, whereas lattice oxygen from CeO₂ desorbs at a relatively higher temperature [35,36,39]. Fig. 15 shows O₂-TPD profiles before and after

yttrium doping CeO_2 with a porous broom-like hierarchical structure. The oxygen desorption peak of pure ceria with a porous broom-like hierarchical structure located

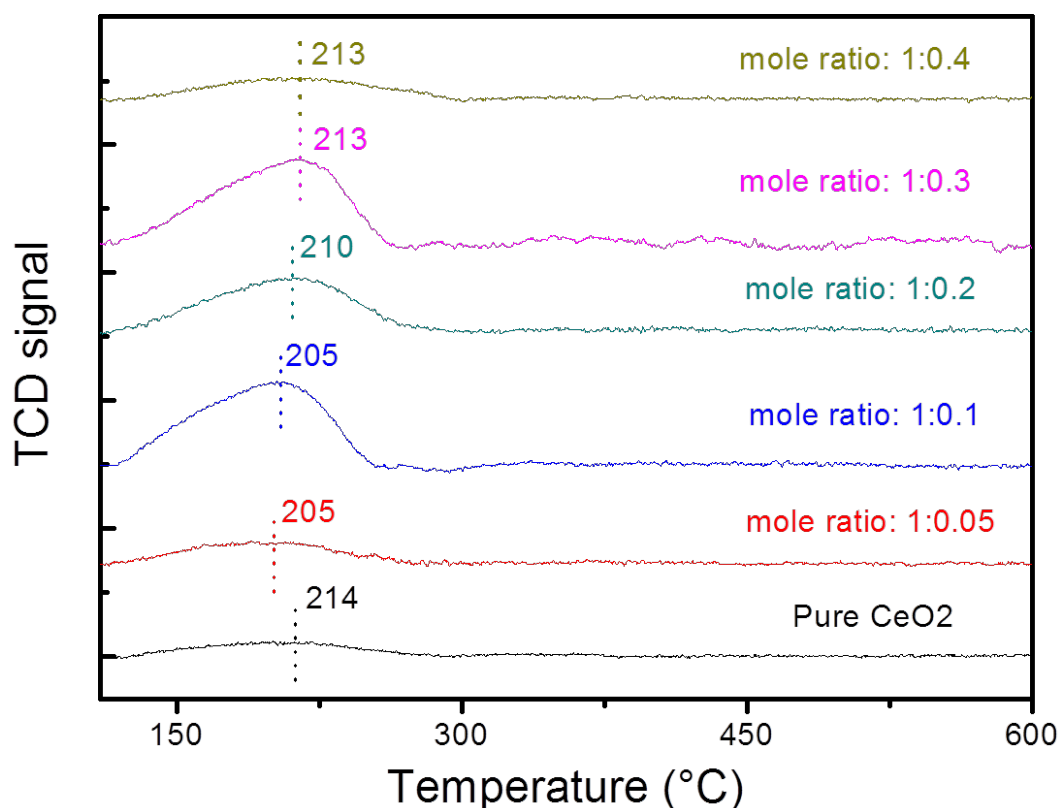


Fig. 15: O_2 -TPD profiles of as-fabricated samples with different mole ratios of $\text{Ce}(\text{NO}_3)_3 \cdot 6\text{H}_2\text{O} : \text{Y}(\text{NO}_3)_3 \cdot 6\text{H}_2\text{O}$.

at about 214 °C, assigned to surface oxygen species, is lower than that of traditional CeO_2 with a 1D or 2D structure [37-39]. After yttrium doping, oxygen desorption peak shifted to a lower temperature. When the mole ratios were 1:0.05 and 1:0.1, respectively, the oxygen desorption peak was located at around 205 °C and achieved the lowest desorption temperature. In addition, on the basis of the O_2 -TPD peak area, the total oxygen desorption amount reached a maximum when mole ratio was 1:0.1. With a further increase in the concentration of yttrium, the oxygen desorption peak decreased to 213 °C. Meanwhile, the total oxygen desorption amount decreased and

finally reached an approximate balance. All results indicated that the activity and amount of surface active oxygen species are influenced by the dopant and morphology. Doping of a low concentration of yttrium is effective for improving the activity and amount of surface oxygen distinctly, resulting in an improvement in the catalytic performance. However, excessive concentration of yttrium doping is not effective for improving the activity and amount of surface oxygen and will restrict enhancement of the catalytic properties of the products.

3.6 Photocatalytic activity for acetaldehyde decomposition

The photocatalytic activities of as-fabricated products were evaluated by measuring CO₂ evolution from the photocatalytic decomposition of acetaldehyde.

Fig. 16 shows the time course of CO₂ liberation of samples with different of dopant concentrations. Compared with pure CeO₂, photocatalytic activities were enhanced after yttrium doped. When dopant concentration is low (mole ratio <1:0.1), the as-fabricated samples show an increasing CO₂ liberation rate as in the case of pure CeO₂. When mole ratio was 1:0.1, the CO₂ liberation rate reached a maximum value. Meanwhile the yield amount of CO₂ achieved about 100 ppm. This value is three times concentration of CO₂ liberation pure ceria. Further increasing concentration of dopant (mole ratio >1:0.1), the CO₂ liberation rate decreased. This phenomenon demonstrates that a certain content dopant is beneficial for enhancement of photocatalytic activities. According to above discussion, more surface active oxygen and oxygen vacancy exist on the surface of the broom-like ceria with porous structure.

The surface oxygen vacancy can interact strongly with activity oxygen molecules to form O_2^- [40,41]. O_2^- is an efficient electron capture, which can easily trap

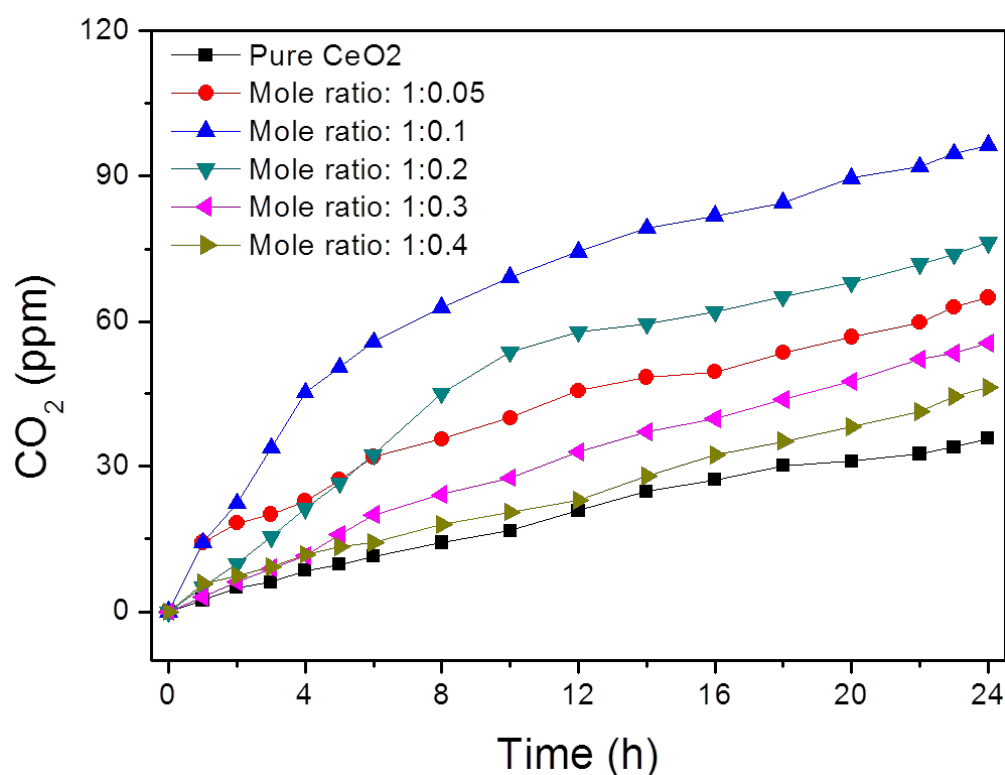


Fig. 16: Time course of CO₂ liberation from acetaldehyde decomposition of as-fabricated samples.

photo-generated electrons to restrict the recombination of photogenerated electrons and holes. The formation of O_2^- is considered to be very important for photocatalytic decomposition of acetaldehyde. Herein, more surface oxygen and oxygen vacancy give the rise to the formation of O_2^- , resulting in the improvement of photocatalytic activity of products. Therefore oxygen vacancies and surface active oxygen species after doped play the predominant role in governing the trend of photocatalytic activities.

4. Conclusion

In summary, CeO₂ with an yttrium-doped porous broom-like hierarchical architecture was successfully prepared by a simple hydrothermal method. The method of synthetic is effective and reproducible and can be expanded to fabrication of other rare-earth-doped morphology-controlled inorganic nanoparticle materials. The optimum doping concentration for products were found to be a mole ratio of Ce(NO₃)₃ and Y(NO₃)₃ of 1:0.1. High-resolution TEM showed that yttrium-doped CeO₂ with a broom-like shape is comprised of many small particles with a crystallite size of 10 nm and porous construction can be discovered among the small particles. The present work showed that porous broom-like yttrium-doped CeO₂ exhibits an advantage of photocatalytic activity. The results of photocatalytic activity evaluation were consistent with the results of Raman, XPS, XRD and SEM analyses. The trend for changes in photocatalytic activity was explained by the oxygen vacancies and surface active oxygen species derived from changing yttrium doping. Consequently, yttrium-doped porous broom-like hierarchical CeO₂ is a promising material for practical applications in catalytic materials as well as other novel environmental friendly materials.

References:

- [1] K. Zhou, Z. Yang, S. Yang, Chemistry of Materials 19 (2007) 1215-1217.
- [2] H. Imagawa, A. Suda, K. Yamamura, S. Sun, The Journal of Physical Chemistry C 115 (2011) 1740-1745.

- [3] L. Yan, R. Yu, J. Chen, X. Xing, *Crystal Growth & Design* 8 (2008) 1474-1477.
- [4] R.K. Pati, I.C. Lee, K.J. Gaskell, S.H. Ehrman, *Langmuir* 25 (2008) 67-70.
- [5] Z.-L. Wang, G.-R. Li, Y.-N. Ou, Z.-P. Feng, D.-L. Qu, Y.-X. Tong, *The Journal of Physical Chemistry C* 115 (2010) 351-356.
- [6] Z. Wang, Z. Quan, J. Lin, *Inorganic Chemistry* 46 (2007) 5237-5242.
- [7] S. Kitano, N. Murakami, T. Ohno, Y. Mitani, Y. Nosaka, H. Asakura, K. Teramura, T. Tanaka, H. Tada, K. Hashimoto, H. Kominami, *The Journal of Physical Chemistry C* 117 (2013) 11008-11016.
- [8] C. Paun, O.V. Safonova, J. Szlachetko, P.M. Abdala, M. Nachtegaal, J. Sa, E. Kleymentov, A. Cervellino, F. Krumeich, J.A. van Bokhoven, *The Journal of Physical Chemistry C* 116 (2012) 7312-7317.
- [9] M. Jobbágy, F. Mariño, B. Schönbrod, G. Baronetti, M. Laborde, *Chemistry of Materials* 18 (2006) 1945-1950.
- [10] H. Xiao, Z. Ai, L. Zhang, *The Journal of Physical Chemistry C* 113 (2009) 16625-16630.
- [11] F. Dvořák, O. Stetsovych, M. Steger, E. Cherradi, I. Matolínová, N. Tsud, M. Škoda, T. Skála, J. Mysliveček, V. Matolín, *The Journal of Physical Chemistry C* 115 (2011) 7496-7503.
- [12] B.Xu, Q.Zhang, S. Yuan, M. Zhang, T. Ohno, *Chemical Engineering Journal*, 260 (2015) 126-132.
- [13] B.Xu, Q.Zhang, S. Yuan, M. Zhang, T. Ohno, *Applied Catalysis B:Environmental* 164 (2015) 120-127.

- [14] Z. Yang, D. Han, D. Ma, H. Liang, L. Liu, Y. Yang, *Crystal Growth & Design* 10 (2009) 291-295.
- [15] L.-W. Qian, X. Wang, H.-G. Zheng, *Crystal Growth & Design* 12 (2011) 271-280.
- [16] S.L. Mitchell, J. Guzman, *Materials Chemistry and Physics* 114 (2009) 462-466.
- [17] L.-S. Zhong, J.-S. Hu, A.-M. Cao, Q. Liu, W.-G. Song, L.-J. Wan, *Chemistry of Materials* 19 (2007) 1648-1655.
- [18] Z.-Y. Pu, X.-S. Liu, A.-P. Jia, Y.-L. Xie, J.-Q. Lu, M.-F. Luo, *The Journal of Physical Chemistry C* 112 (2008) 15045-15051.
- [19] A.E. Baranchikov, O.S. Polezhaeva, V.K. Ivanov, Y.D. Tretyakov, *CrystEngComm* 12 (2010) 3531.
- [20] C.-Y. Cao, Z.-M. Cui, C.-Q. Chen, W.-G. Song, W. Cai, *The Journal of Physical Chemistry C* 114 (2010) 9865-9870.
- [21] F. Zhang, S.-W. Chan, J.E. Spanier, E. Apak, Q. Jin, R.D. Robinson, I.P. Herman, *Cerium oxide nanoparticles: Size-selective formation and structure analysis*, *Applied Physics Letters*, 80 (2002) 127.
- [22] X.D. Zhou, W. Huebner, *Applied Physics Letters*, 79 (2001) 3512.
- [23] Y. Lee, G. He, A.J. Akey, R. Si, M. Flytzani-Stephanopoulos, I.P. Herman, *Journal of the American Chemical Society* 133 (2011) 12952-12955.
- [24] S. Chang, M. Li, Q. Hua, L. Zhang, Y. Ma, B. Ye, W. Huang, *Journal of Catalysis* 293 (2012) 195-204.
- [25] Z.D. Dohčević-Mitrovi, M. Grujić-Brojčin, M. Šćepanović, Z.V. Popović, S. Bošković, B. Matović, M. Zinkevich, F. Aldinger, *Condensed Matter*, 18 (2006)

S2061-S2068.

[26] K.C.H. J. R. McBride, B. D. Poindexter, and W. H. Weber, *Journal of Applied Physics*, 76 (1994) 2435.

[27] Y. Lee, G. He, A.J. Akey, R. Si, M. Flytzani-Stephanopoulos, I.P. Herman, *Journal of the American Chemical Society*, 133 (2011) 12952-12955.

[28] S. Chang, M. Li, Q. Hua, L. Zhang, Y. Ma, B. Ye, W. Huang, *Journal of Catalysis*, 293 (2012) 195-204.

[29] L. Ma, D. Wang, J. Li, B. Bai, L. Fu, Y. Li, *Applied catalysis B: environmental* 148-149(2014) 36-43.

[30] Y.V.f. Holger Borchert, Vasiliy V.Kaichev, Igor P.Prosvirin, *J.phys. chem.B*, 109 (2005) 5728-5738.

[31] Benjaram M. Reddy, Atallah Khan, *J. Phys. Chem. B*, 106(2002) 10964-10972.

[32] C.Ho, J. Yu, T.Kwong, A. Mak, S.Lai, *Chem. Mater*, 17(2005), 4514-4522.

[33] Karl Sohlberg, Sokrates T. Pantelides, Stephen J. Pennycook, *J. Am. Chem. Soc*, 123(2001) 6609-6611.

[34] M.Jobba'gy, F.Marin'õ, B.Scho'nbrod, G.Baronetti, M. Laborde, *Chem. Mater*, 18 (2006) 1945-1950.

[35] G. Avgouropoulos, T. Ioannides, *Journal of Molecular Catalysis A: Chemical*, 296 (2008) 47-53.

[36] M. Li, Z. Wu, S.H. Overbury, *Journal of Catalysis*, 306 (2013) 164-176.

[37] Sanjaya D. Senanayake and David R. Mullins, *J. Phys. Chem. C*, 112(2008), 9744-9752.

- [38] Matthew B. Boucher, Nan Yi, Forrest Gittleson, Branko Zujic, Howard Saltsburg, Maria Flytzani-Stephanopoulos, *J. Phys. Chem. C*, 115(2011), 1261–1268.
- [39] Tana, M.zhang, J.li, H.Li, Y.li, W. Shen, *Catalysis Today*, 148(2009)179-183.
- [40] Bilms S A, Mandelbaum P, Alvarez F, *Journal of Physical Chemistry B*, 104(2000) 9851-9858.
- [41] I. Ait-Ichou, M. Formenti, B. Pommier, S.J. Teichner, *Journal of Catalysis*, 91(1985) 293-307.

Chapter 3

Morphology Control and Photocatalytic Characterization of Yttrium-doped Hedgehog-like CeO₂

1. Introduction

Cerium dioxide, an important rare-earth oxide, has attracted much attention due to its significant fluorite-type structure, remarkable redox properties [1] and prominent oxygen storage and release capacity (OSC) via facile conversion between Ce^{4+} and Ce^{3+} oxidation states [2]. It has been extensively utilized in many practical applications such as polishing materials [3], solar cells[4], ultraviolet blocking materials [5, 6] and photocatalytic materials. Pure CeO_2 , an n-type semiconductor, has a band gap (3.2eV) similar to those of other commonly utilized semiconductor-based photocatalyst such as TiO_2 [7] and possesses potential as a suitable photocatalyst. Recently, CeO_2 materials with different morphologies have been synthesized by various methods including thermal evaporation [8], coprecipitation [9], and the sol-gel technique [10]. Previous studies have indicated that excellent catalytical performance and easy functionalization of CeO_2 materials can be achieved by controlling their structural properties [11]. For instance, our group successfully fabricated sesame ball-like $\text{CeO}_2 : \text{Y}^{3+}/\text{P}(\text{St-AA})$ composite microspheres [12]. Compared with conventional nanowires, nanorods and nanocubes as well as nanoparticles with other shapes, newly constructed CeO_2 with a hierarchical architecture will acquire some special properties that single morphology CeO_2 does not possess [10, 13, 14]. Although some progress has been made in the fabrication of hierarchical architectures composed of 1D nanostructures, the methods usually need special templates through a complex experimental course. For example, Sam L. Mitchell et al. had fabricated coral-like mesostructured CeO_2 using an amino acid as

template [15]. Zhong et al. reported the preparation of 3D flowerlike ceria at 180 °C with TBAB as a surfactant and EG as a solvent [16].

The use for morphology and size-controlled metal and metal oxide composites and different ionic doping are the three most commonly utilized methods for enhancing the photocatalytic properties of CeO₂-based materials. The keypoint in these approaches is changing the oxygen vacancy concentrations of products, because oxygen vacancies can act as electron or hole capture centers and can trap the photogenerated electrons or holes excited by ultraviolet or visible light. Further oxygen vacancies can effectively restrain the recombination of electron-hole pairs, resulting in improvement of photocatalytic activities [17]. Application of more than two or all of the above methods to the preparation of a 3D hierarchical structure of CeO₂ with a high concentration of oxygen vacancies would be a huge challenge. To the best of our knowledge, there has been no report about yttrium-doped hedgehog-like CeO₂ obtained by facile controlled synthesis.

Herein, we report for the first time a facile and feasible approach to prepare CeO₂ with a yttrium-doped hedgehog-like hierarchical structure by a simple template-free hydrothermal technique using the simple inorganic salts Ce(NO₃)₃, Y(NO₃)₃ and Na₃PO₄ as original materials. The morphology of as-fabricated samples can be controlled by tuning the reaction temperature and reactant concentration.

2. Experimental section

2.1 Preparation.

CeO₂ with yttrium-doped hedgehog-like hierarchical structure was fabricated through the traditional hydrothermal process. All original analytical grade materials were purchased from Wako Co., Ltd and were used without any further purification. Cerium nitrate (Ce(NO₃)₃·6H₂O) 0.87 g and yttrium nitrate (Y(NO₃)₃·6H₂O) 0.07 g were dissolved in 100 ml of deionized water with vigorous magnetic stirring for 30 minutes at room temperature. Then 7.7 mg sodium phosphate (Na₃PO₄) was added to the aqueous solution. The mixture was stirred continuously for one hour. The mixed solution was then sealed in a Teflon-lined autoclave and heated at 100~250 °C for 12-96 hours. After cooling to room temperature, a light yellow precipitate was collected by centrifugation and washed several times with deionized water and ethanol. Target products were obtained after dried in the air at 60 °C for one day.

2.2 Characterizations.

An X-Ray diffractometer (XRD) (Bruker-AXS, D8 sss) with Cu Ka radiation ($\lambda=1.5406\text{\AA}$) and monochromator was used to identify the crystalline phase. The crystallite parameters and size were calculated by the Rietveld method (TOPAS 4.0). N₂ adsorption and desorption isotherms were recorded at 77 K using a Nova 4200e instrument. The samples were precisely weighted and degased at 373 K for 3 h. The specific surface area was calculated by the 5 points Brunauer-Emmit-Teller theory. Raman analysis (Renishaw, In via) was performed using a 532 nm excitation laser with 5 mW and an air-cooled CCD detector. Raman peak shifts were determined by fitting with the Lorentzian and Gaussian composite function. Morphology and size of

as-fabricated products were examined by using a field emission scanning electron microscope (FESEM) (Hitachi, S-4800, 15KV), high-resolution transmission electron

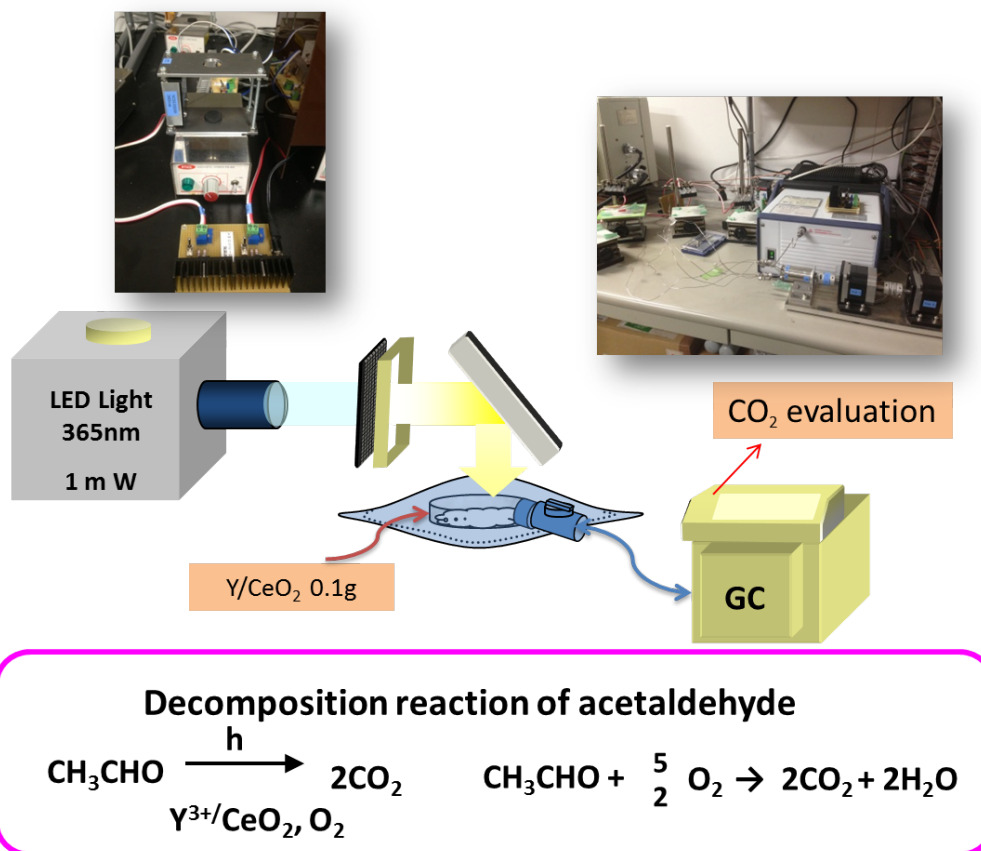


Fig 1: Photocatalytic measurement instrument Schematic diagram

microscope (HRTEM) and HADDF-STEM (FEI, Tecnai G2 F30 S-TWIN, 300KV).

Inductively coupled plasma atomic emission spectrum (ICP-AES) (Shimadzu, ICPS-8000) was used to identify the yttrium's stability in the solution.

2.3 Photocatalytic Evaluations.

UV lighter using black light (UVP, XX-15BLB) can be used in order to remove possible organic materials adsorbed on the surface of samples more than one week

before evaluation of photocatalytic activity. The photocatalytic activity of as-fabricated samples was assessed by ability for decomposition of acetaldehyde. And the analytic instruments are show in the Fig 1. Twenty milligrams of powder was spread on the bottom of a glass dish, and the glass dish was placed in a Tedlar bag (AS ONE Co. Ltd.). Five hundred ppm of acetaldehyde was injected into the bag together with 125 cm³ of artificial air. Then the bag, which was fabricated above, was put into a dark place at room temperature for 2 hours for the purpose of reaching an adsorption equilibrium. A light-emitting diode (LED; Epitex, L365), which emitted light at wavelengths of ca. 365 nm, was used as a light source, and its intensity was controlled at 0.9 mW cm⁻². The concentration of generated CO₂ as a function of irradiation time was monitored by a gas chromatography (Shimadzu GC-8A, FID detector) equipped with a Porapak N-packed column and a methanizer (GL Science, MT-221).

3. Results and discussion

3.1 Structure characterization

Typical X-ray diffractometer (XRD) patterns of samples obtained under different conditions are shown in Fig. 2 (A)-(D). All of the diffraction lines could be indexed to the phase of ceria with a cubic fluorite structure (JCPDS No. 43-1002). The sharp diffraction peaks from all samples suggest a high degree of crystallinity of fabricated samples, and no impurity peaks appeared, indicating that reaction time, amount of the mineralizer (Na₃PO₄) and concentration of the dopant (yttrium nitrate)

have no effect on crystalline phase purity of products. The relative intensity of each peak does not change, suggesting that there is no preferred orientation. A weak peak at $2\theta=31.38^\circ$ assigned to $\text{Ce}(\text{PO}_4)$ (111) can be seen in the pattern shown in the Fig. 1(D). The results show that part of Ce^{3+} reacted directly with PO_4^{3-} in the solution,

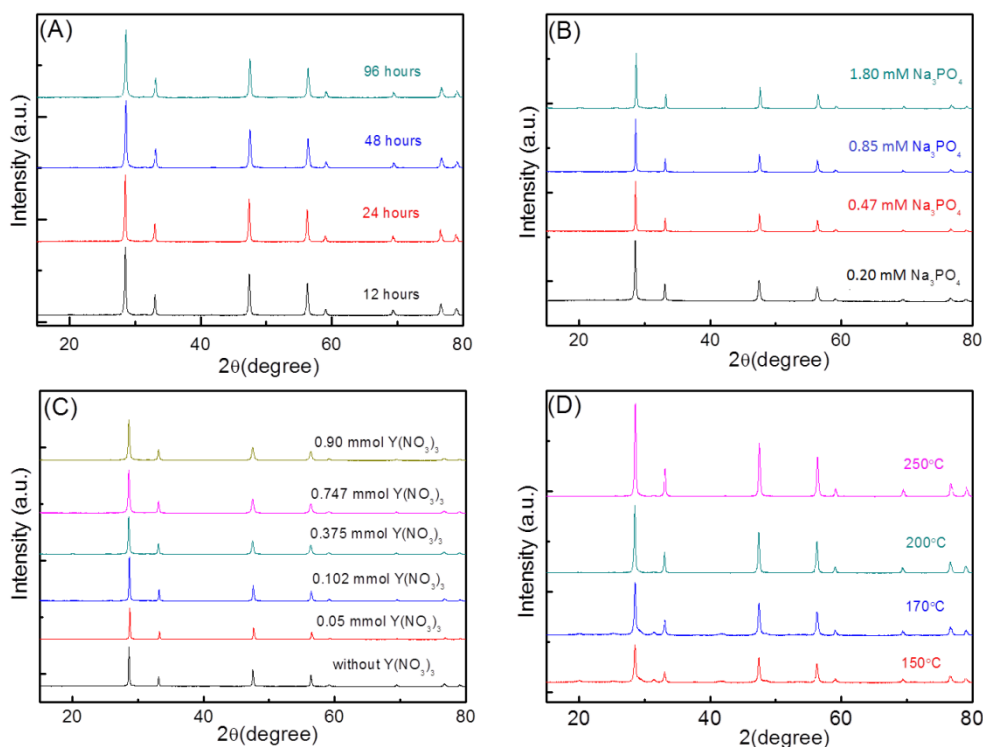


Fig. 2. XRD patterns of as-fabricated samples (A) different reaction time, (B) different concentration of Na_3PO_4 , (C) different concentration of dopant and (D) different reaction temperature.

resulting in CePO_4 precipitation, instead of occur oxidation to form CeO_2 owing to the low reaction temperature (below 170°C). With increase in temperature, impurity crystal phase cerium phosphate disappeared. This phenomenon occurs because a high temperature is beneficial for Ce^{3+} to Ce^{4+} oxidation reaction.

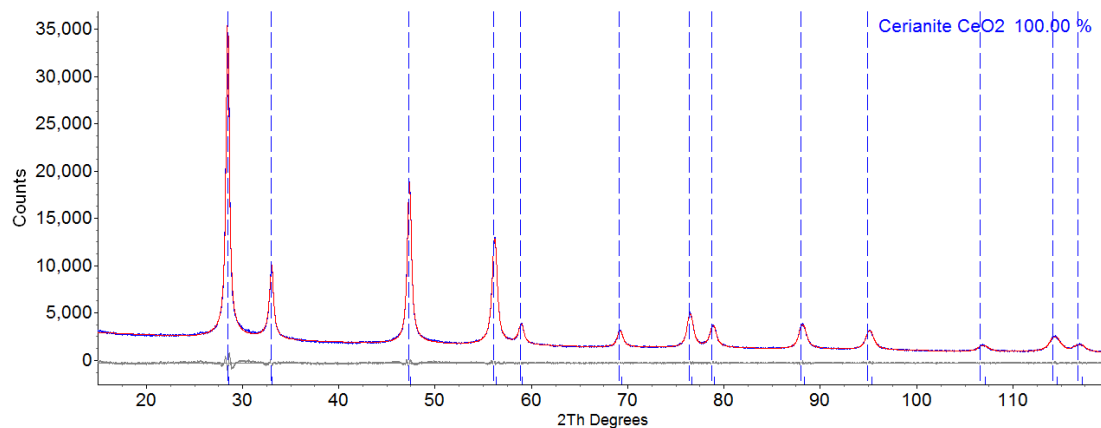


Fig. 3. Rietveld refined spectra with TOPAS 4.0

Rietveld refinements were also carried out according to the diffraction lines by varying parameters such as background (Fig. 3), unit cell, and isotropic thermal parameters. When the reaction temperature and time were changed while maintaining the amount of the dopant, the variations of lattice value ($a=5.3300\pm 0.0060$ Å) were smaller. However, the lattice parameter showed significant variation for as-fabricated samples with change in dopant stoichiometry. The unit cell value a changed from 5.33052 to 5.27510 Å (see the Table 1). It can be clearly seen that the lattice value (a)

sample	Lattice value a (Å)	Particles size D (nm)	$R_{\text{dopant}}/F2g$ (%)	S_{BET} (m^2/g)
Pure CeO_2	5.41001	55.987	0	8.132
$\text{CeO}_2+\text{Y}/$ octahedral	5.33052	48.162	4.16	23.594
$\text{CeO}_2+\text{Y}/$ octahedral+nanrod	5.31606	28.831	4.93	70.405
$\text{CeO}_2+\text{Y}/$ nanorod	5.27510	32.833	3.62	49.082

Table 1. Relevant data of as-fabricated samples used in the work.

after doping is smaller than the bulk CeO_2 lattice parameter value $a=5.41048$ Å even though the space group is still Fm-3m before and after doping. This indicates that

yttrium has partially substituted cerium ions and introduced into the interior lattice, maintaining the ceria cubic fluorite structure instead of forming a Y_2O_3 - CeO_2 composite. In addition, a linear relationship could be drawn between the lattice value and amount of doping. In other words, the amount of dopant plays a definitive role in determining ceria lattice parameters. Yttrium enters the crystal lattice and substitute cerium ions of the crystal lattice. Consequently, the crystal lattice would contract due to an increase in oxygen vacancy concentration with increase in yttrium content, despite of the fact that the ionic radius of yttrium is larger than that of cerium (1.019 and 0.97 Å, respectively). Particles sizes (D) of as-fabricated samples are also be obtained by Whole Pattern Profile fitting instead of single peak refinement (Scherrer formula). D values are randomly distributed between the 20 and 60 nm. A comparison of our results with those of previous studies [8, 18, 19] were reached the following conclusions. Although changes of particles size resulted in the crystal lattice expansion or contraction of CeO_2 , the effects would become weaker after yttrium doping.

Raman technology is considered to be a very efficient and nondestructive technique for characterization of ceria nanoparticles and their derivatives. Raman spectra of as-fabricated samples under various experimental conditions are shown in Fig. 4 (A)-(D). A strong Raman shift at $\sim 460\text{ cm}^{-1}$ and a relatively weak shift at $\sim 600\text{ cm}^{-1}$ can be detected. The shift at $\sim 460\text{ cm}^{-1}$ can be assigned to F2g vibration of the fluorite-type structure and it can be considered as the symmetric stretching mode of oxygen atoms around cerium ions, and the molecule retains its tetrahedral symmetry

throughout. Based on the results of previous studies [20-22] and our own studies, a weak and less prominent band near $\sim 600\text{ cm}^{-1}$ can be attributed to a nondegenerate longitudinal optical mode caused by a local Ce-O ($R_{\text{Ce-O}}$) bond symmetry stretch. According to previous reports that not all cerium ions show Ce^{4+} chemical valence in the lattice; small cerium ions show Ce^{3+} tervalence. In order to maintain the particles in an electrically neutral state, the lattice oxygen would escape from the structure and

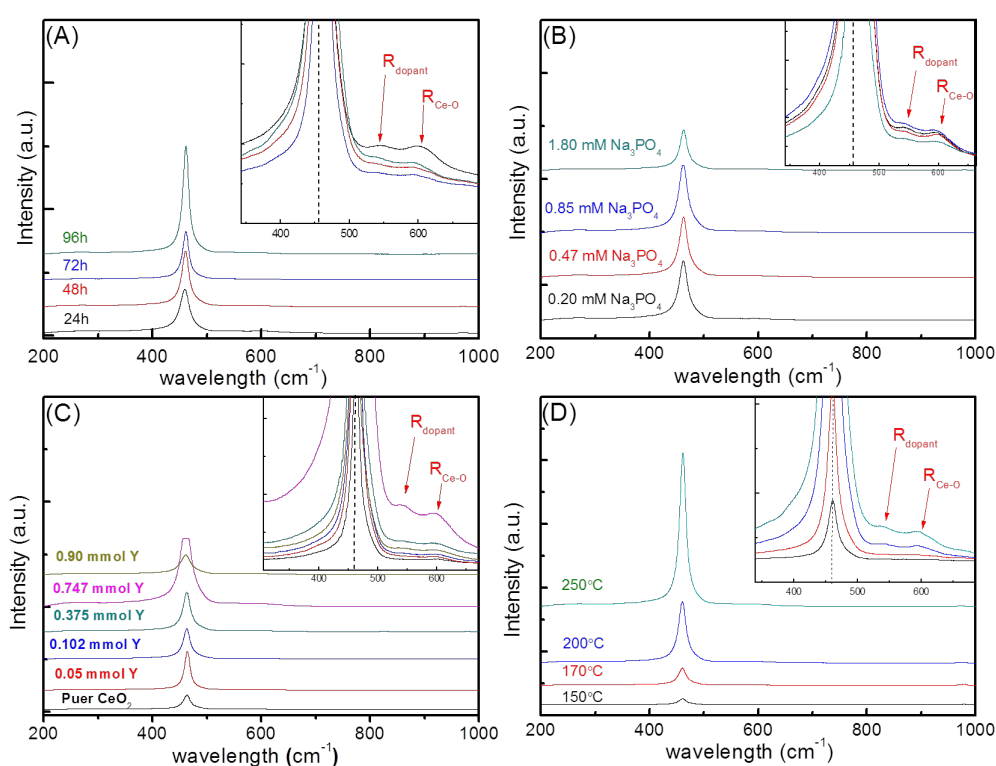


Fig. 4. Raman spectra of as-fabricated samples (A) different reaction time, (B) different concentration of Na_3PO_4 , (C) different concentration of dopant and (D) different reaction temperature.

finally result in the formation of intrinsic oxygen vacancies. Oxygen vacancies perturb the local Ce-O bond symmetry. A new and weak Raman shift at $\sim 530\text{ cm}^{-1}$, which cannot be detected in Raman spectra of pure CeO_2 , can be seen in the inset of Fig. 4 (C). It is attributed to extrinsic oxygen vacancies caused by doping (R_{dopant}). As

a dopant, yttrium enters the cubic fluorite lattice of CeO_2 and substituted cerium. In order to maintain electronic neutrality, doping cations showing different valence states with Ce^{4+} and part of the oxygen would also escape from lattice to form extrinsic oxygen vacancies. The relativity intensities of Raman shifts (F2g and R_{dopant}) were calculated and are shown in the Table1, It can be seen that the value of $R_{\text{dopant}}/\text{F2g}$ rapidly increased at first and then reached an approximate balance with further increase in dopant content. The trend for change in the value can be attributed to amount of dopant. At the first yttrium was introduced into the bulk CeO_2 , and more extrinsic oxygen vacancies were obtained. Therefore, the value of $R_{\text{dopant}}/\text{F2g}$ ratio rapidly increased. When excessive dopants were added, the oxygen vacancy concentration increased and eventually reached a steady plateau level in order to maintain electron neutrality of the system. This result of Raman analysis is consistent with the following activity evaluation.

3.2 Morphology characterization

The morphology and evolution process of as-fabricated products were investigated by FE-SEM and HR-TEM. Fig. 5 (a) shows a panoramic FE-SEM image of yttrium-doped CeO_2 particles. It can be seen that the particles are uniform octahedral particles with diameters of approximately 200 nm. The lattice spacing of the parallel fringes in the inset graph is 0.32 nm, corresponding to the (111) plane of FCC CeO_2 . In addition, the composition of elements and distribution of the as-fabricated products obtained under different experimental conditions were

analyzed by STEM-HAADF images and EDS mapping images. Fig. 6 shows the existence of not only cerium but also yttrium, with yttrium ions being dispersed evenly on the CeO₂ octahedral structure surface and in the bulk. Herein we can draw a conclusion that yttrium enters the lattice and dopes the parts of cerium successfully. The results for composition of elements and distribution are well consistent with the results of the XRD and Raman analysis. Fig. 5 (b) shows that with increase in the amount of Na₃PO₄, a small number of nanorods with length of 50 nm and diameters

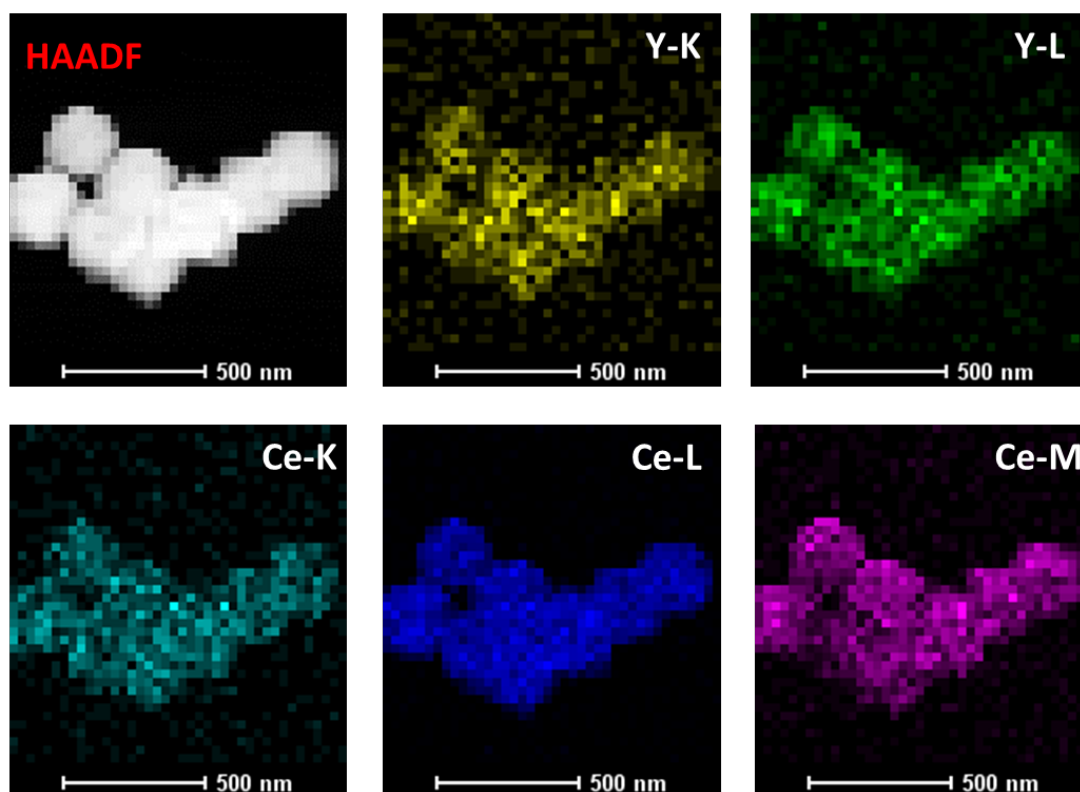


Fig. 6. HAADF-STEM and EDS mapping images of as-fabricated sample (0.47 mM Na₃PO₄ and 0.747 mmol Y(NO₃)₃ as original materials and reaction at 200 °C for 2 hours).

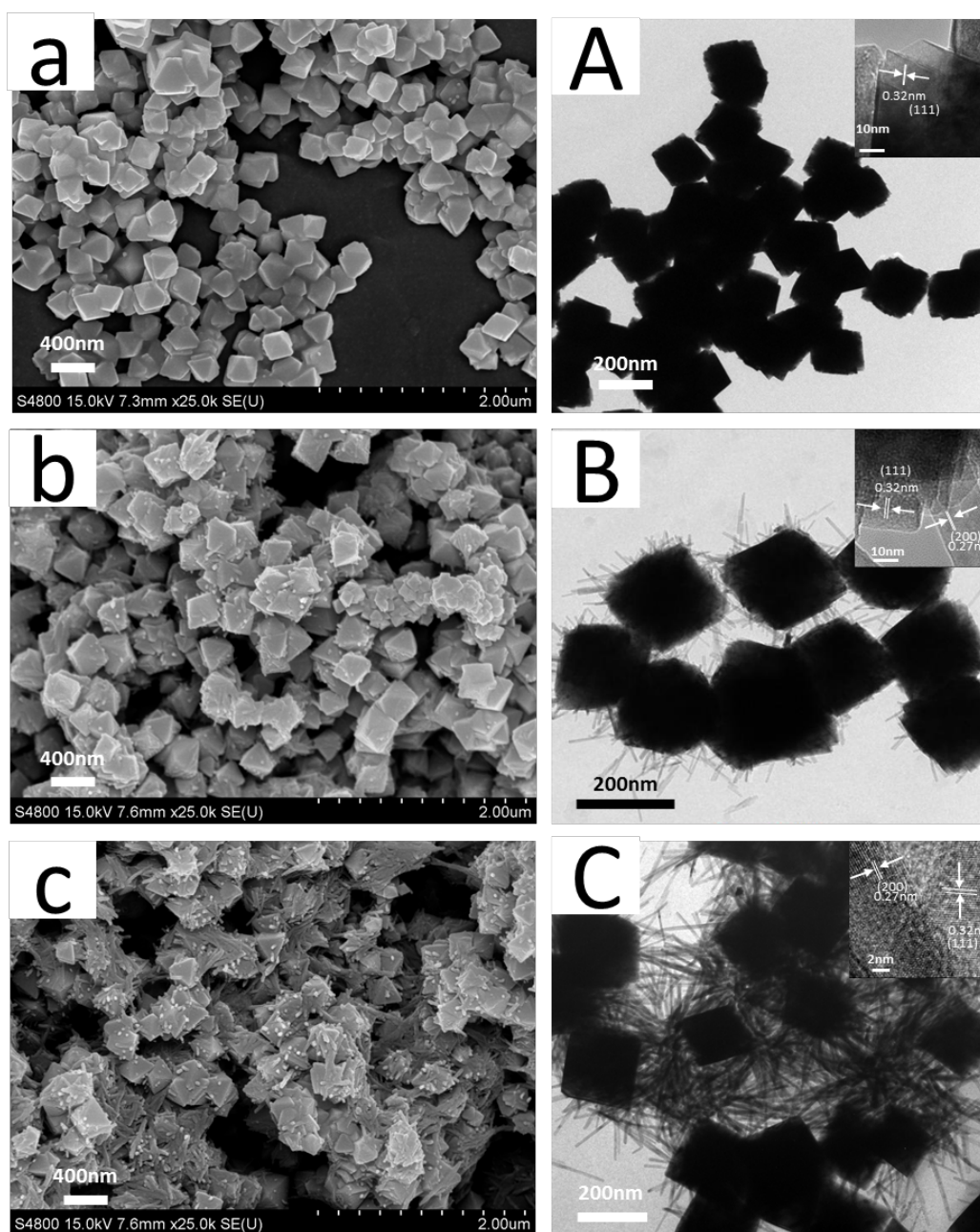


Fig. 5. FE-SEM and HR-TEM images of as-fabricated samples at different concentrations of Na_3PO_4 : (a)-(A) 0.20 mM, (b)-(B) 0.47 mM and (c)-(C) 0.85mM.

of 10 nm grew on the eight octahedral surfaces. The lattice spacing of the parallel fringes in the inset graph are 0.32 nm and 0.27 nm, respectively, corresponding to the (111) plane and (200) plane of FCC CeO_2 . The inset images demonstrates that the nanorod mainly exposed the (200) planes as well as the octahedral exposed the (111)

planes. Fig. 5(c) reveals that with further increase in the amount of Na_3PO_4 , many more nanorods appeared and the octahedral size decreased rapidly as the nanorods become longer. The nanorod length reached about 100 nm with the diameter remaining constant at 10 nm, while the octahedral size decreased to 100 nm. The morphology evolution can also be illustrated by the HR-TEM images (see the Fig. 5(A)-(C)), and the results are consistent with the FE-SEM observation.

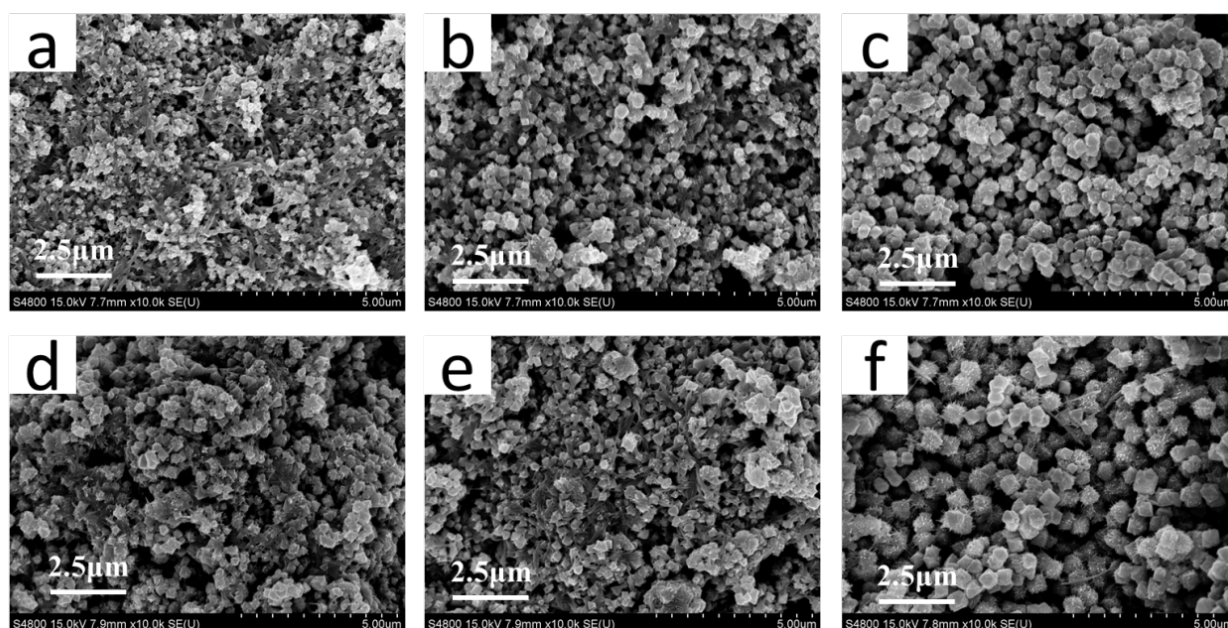


Fig. 7. FE-SEM images of as-fabricated samples at different dopant contents: (a) 0.05 mmol, (b) 0.102 mmol, (c) 0.375 mmol, (d) 0.747 mmol, (e) 0.91 mmol and (f) 1.2 mmol.

The effects of different amounts of doping and different reaction temperatures on morphology were also analyzed by FE-SEM images. Fig. 7 shows that the morphology alters with variation of dopant content. With increase in the amount of $\text{Y}(\text{NO}_3)_3$, the shape of as-fabricated samples did not change noticeably. The morphology and size of products maintain the hedgehog-like hierarchical structure. In other words, the amount of dopant has no effect on the morphology and size control. On the other hand, the morphology clearly changed with change in the reaction

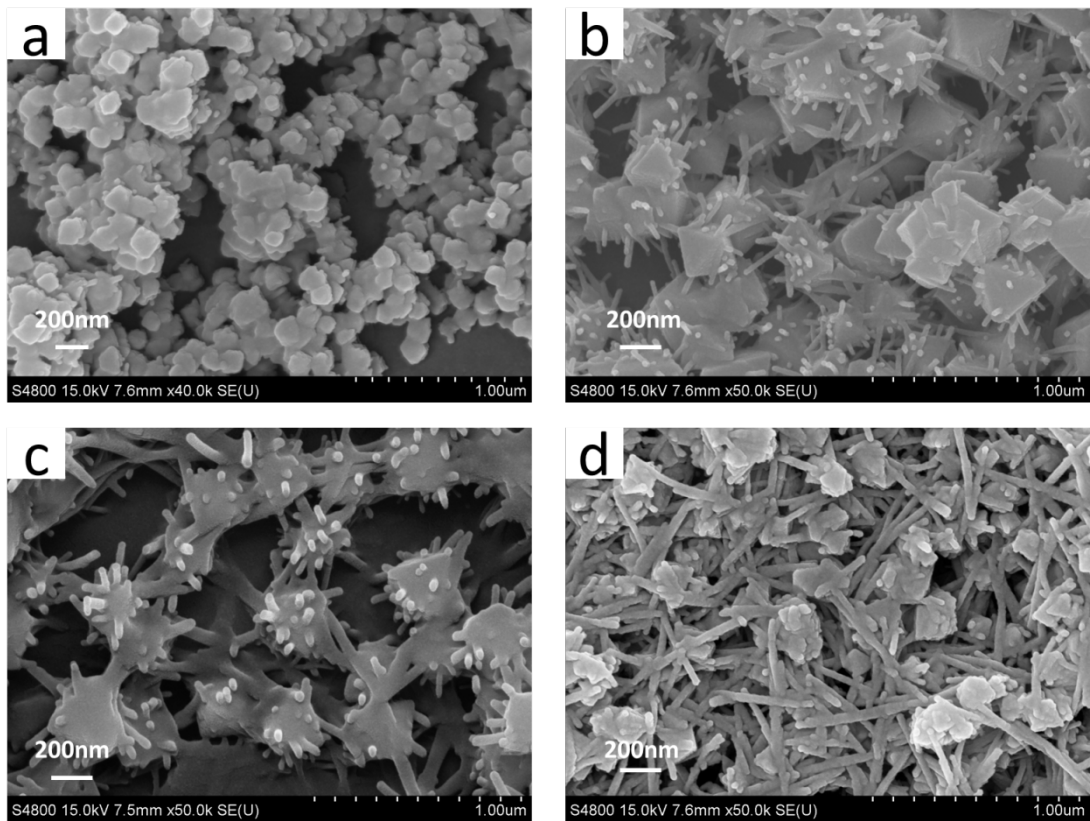


Fig. 8. FE-SEM images of as-fabricated samples at different reaction temperature: (a) 150 °C, (b) 170 °C, (c) 200 °C and (d) 250 °C.

temperature. Fig. 8 (a) demonstrates that only octahedral particles existed at 150 °C and these particles aggregated due to no addition of a surfactant. When the reaction temperature was below 150 °C, there was no precipitation from the solution. With increase in the reaction temperature, some short nanorods appeared on the octahedral surfaces (see Fig. 8 (b)) and the nanorods were not evenly distributed on the surface. There were some rods on one plane, while there was no nanorod on another plane. When the reaction temperature reached 200 °C, many more nanorods emerged, while the octahedral size decreased dramatically and the rods became longer. Fig. 8 (d) indicates that with further increased temperature only the nanorods can be obtained at

the cost of consuming CeO₂ octahedral completely.

Through systematic experiments, it was shown that the hydrothermal temperature and amount of original sodium phosphate play a vital role in control of CeO₂ nanostructures. The as-fabricated samples mainly showed octahedral morphology when PO₄³⁺ concentration was below 0.02 mM and hydrothermal temperature was under 150 °C due to phosphate group might control the morphology by affect the surface electrostatics potential and energy of octahedral CeO₂. A high concentration of PO₄³⁺ will provide more electrostatic potential [23] and a high temperature will supply surface energy on CeO₂ surfaces, resulting in the formation of hedgehog-like hierarchical structure [24, 25]. When the phosphate concentration exceed 0.85 mM and the temperature was higher than 250 °C, we could easily obtain a nanorod CeO₂ morphology which could be ascribed the following two reasons. First, excessive phosphate groups may restrict the formation of octahedral by steric influence [26]; The second, high temperature will conducive to the formation of nanorods.

3.3 UV-vis diffuse reflectance spectra and band gap energy

The UV-vis diffuse reflectance spectra of as-fabricated samples are shown in Fig. 9 (a). The optical band gap energy (E_g) can be calculated from the plot between $E = 1240/\lambda(\text{nm})$ [27, 28], where λ is the wavelength corresponding to the absorption, and $[F(R)hv]^{1/2}$ [29, 30] as shown in Fig. 9 (b). CeO₂ without doping has absorption at ~380 nm and band gap energy at 3.20 eV, which originate from the charge-transfer

between O_{2p} and Ce_{4f} states in O^{2-} and Ce^{4+} . Compared with pure CeO_2 , the ym

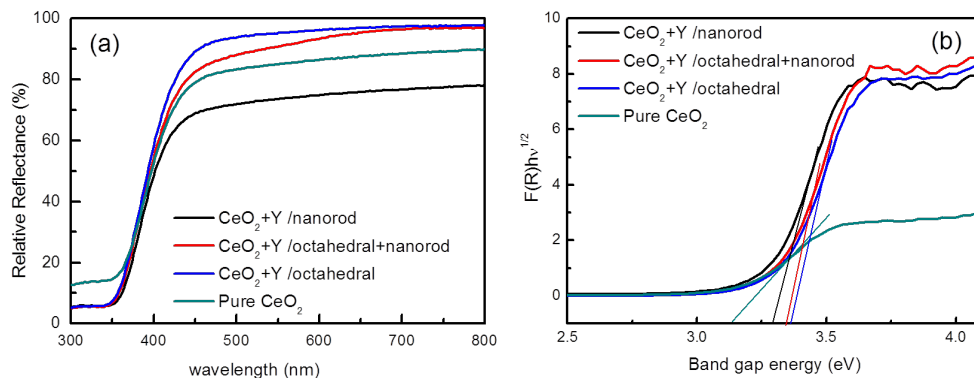


Fig.9. Uv-vis diffuse reflectance spectra of samples with different morphology.

reflectance decreases and absorption red-shifts after the lattice cerium ions have been substituted by yttrium, indicating that the oxygen vacancies increased due to a charge compensation mechanism [31]. Fig. 5 (b) clearly reveals that pure CeO_2 exhibits low band gap energy compared to that of yttrium-doped ceria, and the E_g values are 3.20 eV and \sim 3.35 eV, respectively. Subtle differences of band gap between various morphologies of yttrium-doped ceria were detected from the plot of K-M curves. Fig. 5(b) indicates that the octahedral morphology has a higher E_g value than the values of other shapes of ceria doped by yttrium. This result is consisted with the results of Raman analysis, and this optical property is very important for good photocatalytic performance.

3.4 Photocatalytic activity for acetaldehyde decomposition

The photocatalytic activities of as-fabricated products were evaluated by measuring CO_2 evolution form the photocatalytic decomposition of acetaldehyde.

Fig. 6 (a) shows the time course of CO₂ liberation of samples with different amounts of original materials Na₃PO₄. Photocatalytic activities were enhanced by increasing the amount of Na₃PO₄ at a low concentration, and photocatalytic activity at 0.47 mM Na₃PO₄ was higher than that of other concentrations. Further increase in the amount of Na₃PO₄, the photocatalytic activities decreased. Change in photocatalytic activities with change in the amount of Na₃PO₄ can be attributed to the change in morphology. Only the sample with a hedgehog-like morphology had a higher concentration of oxygen vacancies than those of other morphology products.

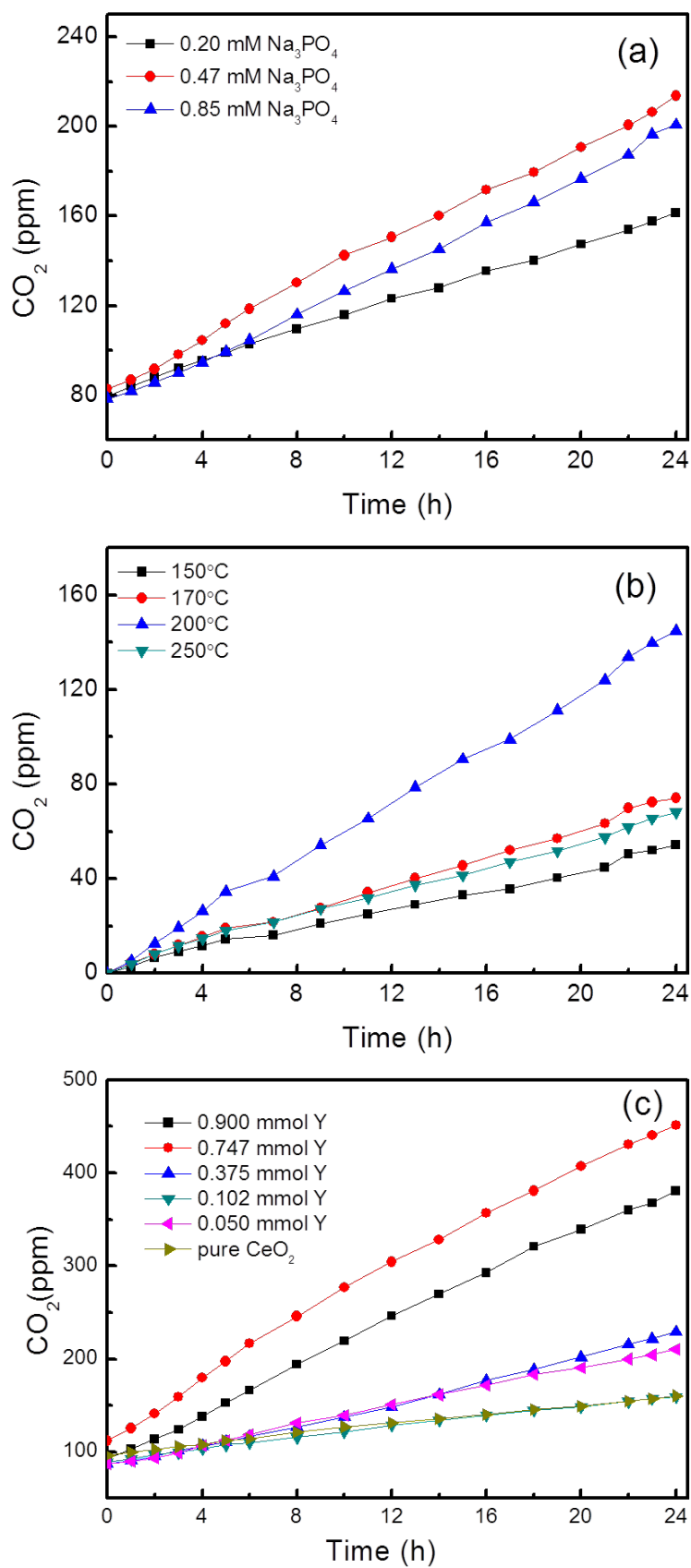


Fig.10. Time course of CO_2 liberation from acetaldehyde decomposition of as-fabricated samples.

owing to the hedgehog-like three dimensional hierarchical structure has a larger specific surface area (see the Table 1), and more activity oxygen exists on higher specific surface area.

Fig. 10 (b) shows the time course of CO₂ liberation of samples with different reaction temperatures. The sample as-fabricated at 200 °C exhibited the highest photocatalytic activities. Photocatalytic activities change trend with reaction temperature is similar to the influence of content Na₃PO₄ which is attributed to morphology evolution. That means at higher (>250 °C) and lower (<170 °C) reaction temperatures purely 1D structure, such as octahedral and nanorod, can be obtained. Compared with the photocatalytic activities of samples with a hedgehog-like 3D hierarchical structure, these samples with 1D morphology shown low photocatalytic activities owing to the lower concentration of oxygen vacancies and smaller S_{BET}.

Fig. 10 (c) shows the time course of CO₂ liberation of samples with different of dopant concentrations. When dopant concentration is low (<0.375 mmol), the as-fabricated samples show a low CO₂ liberation rate as in the case of pure CeO₂. However, with increase in the concentration of the dopant, the CO₂ liberation rate rapidly improved, which demonstrated that a high content dopant is beneficial for enhancement of photocatalytic activities. When the content of dopant reached 0.747 mmol, the fabricated sample showed the highest CO₂ liberation rate, and with further increase in concentration of the dopant, the CO₂ liberation rate decreased.

In order to investigate the photocatalytic reusability and stability of as-fabricated yttrium-doped hedgehog-like CeO₂, a periodic photocatalytic decomposition

experiments were performed. Fig.11 illustrates cycling runs of photocatalytic activity evaluation. The photocatalytic performance of sample has no detectable loss after four recycles and the CO₂ generation rate does not change obviously. Meanwhile, ICP-AES measurement indicated that yttrium doped on CeO₂ can hardly be leached out in suspensions even by 48 hours vigorous stirred (see the Fig.12). Therefore, we can draw a conclusion that yttrium doped CeO₂ with 3D hedgehog-like hierarchical structure possess good photocatalytic reusability as well as excellent stability.

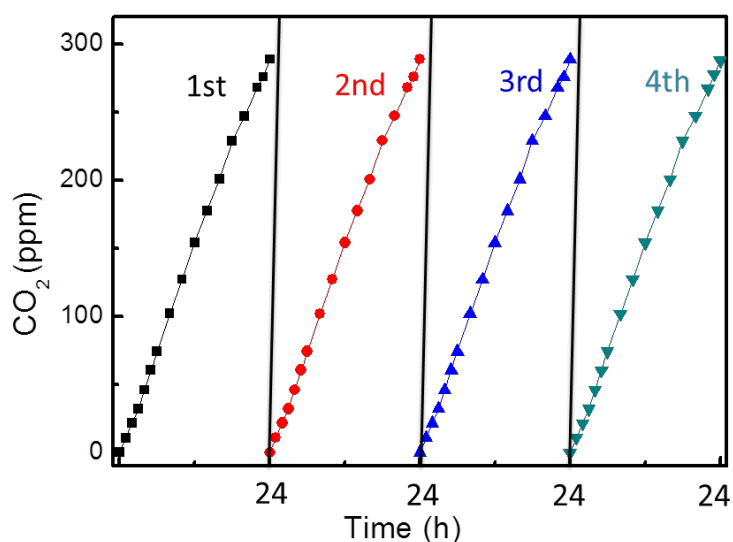


Fig. 11 Cycling runs of the as-fabricated samples in photocatalytic generation of CO₂

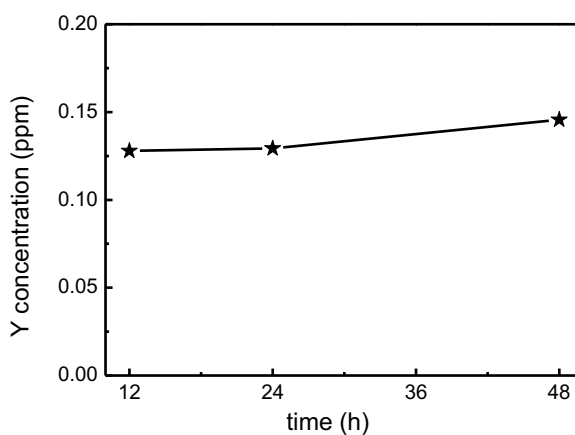
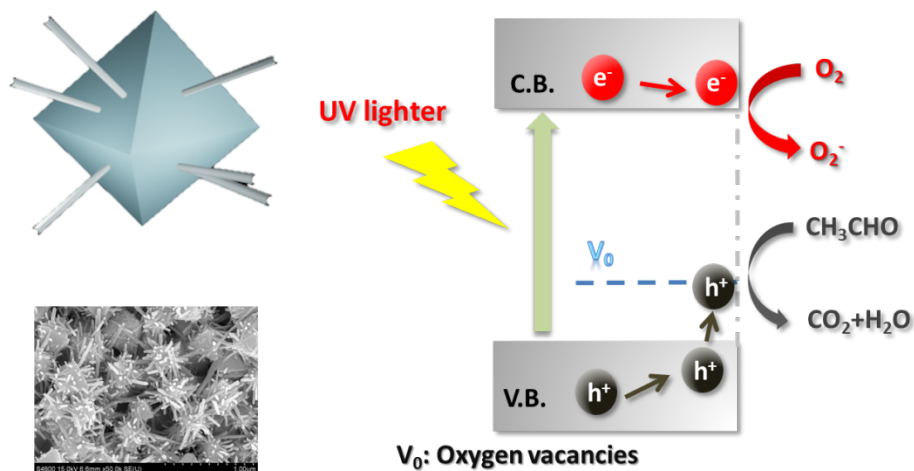


Fig.12. the yttrium elution variation curve of yttrium doped CeO₂ with 3D hedgehog-like hierarchical structure

Oxygen vacancy concentrations of the products play the predominant role in governing the trend of photocatalytic activities. Regardless of the 1D octahedral, nanorod or 3D hedgehog-like hierarchical structure and regardless of the amount of the dopant, the ultimate goal is to control the oxygen vacancy concentrations in the samples. When fabricated samples are irradiated under UV light, electrons are excited from the O_{2p} valence band to the conduction band (Ce_{4f}) resulting in the formation of hole and electron pairs [32], and the holes easily get trapped on the oxygen ions [33, 34](see the Scheme 1). When the number of oxygen vacancies is higher, the oxygen ion mobility becomes higher [35]. Transportation mobility of lattice oxygen ions is beneficial for the separation of photogenerated electrons and holes. Overall, the photogenerated electron and holes recombination will be restricted in higher oxygen vacancies concentration. At the same time, different exposed crystal plane also influence the photocatalytic activity. Traditional CeO_2 with octahedral morphology are enclosed by eight (111) planes as well as the nanorod shape are enclosed by the (200) and (110) planes. Combined with previous studies [36, 37], CeO_2 with nanorod morphology predominantly exposed (200) plane shows higher photocatalytic activity than CeO_2 with octahedral exposed stable (111) plane attributed to the (200) plane are unstable and showing higher surface energy. Hence, 3D hedgehog-like hierarchical structure is beneficial for the formation of a high concentration of oxygen vacancies and has been shown to possess the best photocatalytic activity.



Scheme 1: Schematic illustration of CO_2 evolution from the photocatalytic decomposition of acetaldehyde

4. Conclusion

In summary, CeO_2 with yttrium-doped hedgehog-like hierarchical architectures was prepared successfully by a simple hydrothermal method. The optimum experimental conditions for synthesis of octahedral plus nanorod CeO_2 were found to be 0.47 mM Na_3PO_4 and 0.747 mmol $\text{Y}(\text{NO}_3)_3$ as original materials and reaction at 200 $^\circ\text{C}$ for 24 hours. The method of synthetic is effective and reproducible and can be further expanded to fabricate other rare-earth-doped morphology-controlled inorganic nanoparticle materials. Hedgehog-like yttrium-doped CeO_2 exhibits an advantage of photocatalytic activity. The results of activity evaluation are consistent with the results of Raman, UV-vis DRS, XRD and SEM analyses. The trend for changes in photocatalytic activities was explained by the oxygen vacancies derived from changes in morphology and yttrium doping. Consequently, yttrium-doped hedgehog-like hierarchical CeO_2 is a promising material

for practical application in photocatalytic materials and SOFCs as well as other novel environmental friendly materials.

References:

- [1] K. Zhou, Z. Yang, S. Yang, *Chemistry of Materials* 19 (2007) 1215-1217.
- [2] H. Imagawa, A. Suda, K. Yamamura, S. Sun, *The Journal of Physical Chemistry C* 115 (2011) 1740-1745.
- [3] L. Yan, R. Yu, J. Chen, X. Xing, *Crystal Growth & Design* 8 (2008) 1474-1477.
- [4] R.K. Pati, I.C. Lee, K.J. Gaskell, S.H. Ehrman, *Langmuir* 25 (2008) 67-70.
- [5] Z.-L. Wang, G.-R. Li, Y.-N. Ou, Z.-P. Feng, D.-L. Qu, Y.-X. Tong, *The Journal of Physical Chemistry C* 115 (2010) 351-356.
- [6] Z. Wang, Z. Quan, J. Lin, *Inorganic Chemistry* 46 (2007) 5237-5242.
- [7] S. Kitano, N. Murakami, T. Ohno, Y. Mitani, Y. Nosaka, H. Asakura, K. Teramura, T. Tanaka, H. Tada, K. Hashimoto, H. Kominami, *The Journal of Physical Chemistry C* 117 (2013) 11008-11016.
- [8] C. Paun, O.V. Safonova, J. Szlachetko, P.M. Abdala, M. Nachtegaal, J. Sa, E. Kleymenov, A. Cervellino, F. Krumeich, J.A. van Bokhoven, *The Journal of Physical Chemistry C* 116 (2012) 7312-7317.
- [9] M. Jobbágy, F. Mariño, B. Schönbrod, G. Baronetti, M. Laborde, *Chemistry of Materials* 18 (2006) 1945-1950.
- [10] H. Xiao, Z. Ai, L. Zhang, *The Journal of Physical Chemistry C* 113 (2009) 16625-16630.

- [11]F. Dvořák, O. Stetsovych, M. Steger, E. Cherradi, I. Matolínová, N. Tsud, M. Škoda, T. Skála, J. Mysliveček, V. Matolín, *The Journal of Physical Chemistry C* 115 (2011) 7496-7503.
- [12]Q. Zhang, B. Xu, S. Yuan, M. Zhang, T. Ohno, *Materials Letters* 121 (2014) 109-112.
- [13]Z. Yang, D. Han, D. Ma, H. Liang, L. Liu, Y. Yang, *Crystal Growth & Design* 10 (2009) 291-295.
- [14]L.-W. Qian, X. Wang, H.-G. Zheng, *Crystal Growth & Design* 12 (2011) 271-280.
- [15]S.L. Mitchell, J. Guzman, *Materials Chemistry and Physics* 114 (2009) 462-466.
- [16]L.-S. Zhong, J.-S. Hu, A.-M. Cao, Q. Liu, W.-G. Song, L.-J. Wan, *Chemistry of Materials* 19 (2007) 1648-1655.
- [17]Z.-Y. Pu, X.-S. Liu, A.-P. Jia, Y.-L. Xie, J.-Q. Lu, M.-F. Luo, *The Journal of Physical Chemistry C* 112 (2008) 15045-15051.
- [18]A.E. Baranchikov, O.S. Polezhaeva, V.K. Ivanov, Y.D. Tretyakov, *CrystEngComm* 12 (2010) 3531.
- [19]C.-Y. Cao, Z.-M. Cui, C.-Q. Chen, W.-G. Song, W. Cai, *The Journal of Physical Chemistry C* 114 (2010) 9865-9870.
- [20]Y. Lee, G. He, A.J. Akey, R. Si, M. Flytzani-Stephanopoulos, I.P. Herman, *Journal of the American Chemical Society* 133 (2011) 12952-12955.
- [21]S. Chang, M. Li, Q. Hua, L. Zhang, Y. Ma, B. Ye, W. Huang, *Journal of Catalysis* 293 (2012) 195-204.
- [22]B.M. Reddy, A. Khan, Y. Yamada, T. Kobayashi, S. Loridant, J.-C. Volta,

Langmuir 19 (2003) 3025-3030.

[23]G. Cornelis, B. Ryan, M.J. McLaughlin, J.K. Kirby, D. Beak, D. Chittleborough, Environmental Science & Technology 45 (2011) 2777-2782.

[24]D.R. Mullins, P.M. Albrecht, T.-L. Chen, F.C. Calaza, M.D. Biegalski, H.M. Christen, S.H. Overbury, The Journal of Physical Chemistry C 116 (2012) 19419-19428.

[25]Z.L. Wang, X. Feng, The Journal of Physical Chemistry B 107 (2003) 13563-13566.

[26]M. Lin, Z.Y. Fu, H.R. Tan, J.P.Y. Tan, S.C. Ng, E. Teo, Crystal Growth & Design 12 (2012) 3296-3303.

[27]P. Ji, J. Zhang, F. Chen, M. Anpo, The Journal of Physical Chemistry C 112 (2008) 17809-17813.

[28]J. Li, G. Lu, H. Li, Y. Wang, Y. Guo, Y. Guo, Journal of Colloid and Interface Science 360 (2011) 93-99.

[29]Y. Park, S.K. Kim, D. Pradhan, Y. Sohn, Chemical Engineering Journal 250 (2014) 25-34.

[30]C. Karunakaran, P. Gomathisankar, ACS Sustainable Chemistry & Engineering 1 (2013) 1555-1563.

[31]J. Wang, D.N. Tafen, J.P. Lewis, Z. Hong, A. Manivannan, M. Zhi, M. Li, N. Wu, Journal of the American Chemical Society 131 (2009) 12290-12297.

[32]M.a.D. Hernández-Alonso, A.B. Hungría, A. Martínez-Arias, M. Fernández-García, J.M. Coronado, J.C. Conesa, J. Soria, Applied Catalysis B:

Environmental 50 (2004) 167-175.

[33]P. Bera, A. Gayen, M.S. Hegde, N.P. Lalla, L. Spadaro, F. Frusteri, F. Arena, The Journal of Physical Chemistry B 107 (2003) 6122-6130.

[34]M.B. Watkins, A.S. Foster, A.L. Shluger, The Journal of Physical Chemistry C 111 (2007) 15337-15341.

[35]B. Murugan, A.V. Ramaswamy, The Journal of Physical Chemistry C 112 (2008) 20429-20442.

[36]K. Zhou, X. Wang, X. Sun, Q. Peng, Y. Li, Journal of Catalysis 229 (2005) 206-212.

[37]Tana, M. Zhang, J. Li, H. Li, Y. Li, W. Shen, Catalysis Today 148 (2009) 179-183.

Chapter 4

Synthesis and photocatalytic Characterization of Yttrium-doped CeO₂ with a sphere structure

1. Introduction

Cerium dioxide has been extensively utilized in many practical applications such as polishing materials[1-3], solar cells[4], ultraviolet blocking materials[5-6] and photocatalytic materials. Ceria has attracted much attention due to its significant controlled morphology, fluorite-type structure[7-8], remarkable redox properties and prominent oxygen storage[9-10] and release capacity (OSC) via facile conversion between Ce^{4+} and Ce^{3+} oxidation states[11-12].

Recently, CeO_2 materials with different morphologies have been synthesized by various methods including thermal evaporation [13], coprecipitation [14], and the sol-gel technique [15-17]. Previous studies have indicated that excellent catalytical performance and easy functionalization of CeO_2 materials can be achieved by controlling their structural properties [18-22]. The use for morphology and size-controlled [23-25] metal and metal oxide composites [26-27] and different ionic doping [28-30] are the three most commonly utilized methods for enhancing the photocatalytic properties of CeO_2 -based materials. The keypoint in these approaches is changing the oxygen vacancy concentrations of products, because oxygen vacancies can act as electron or hole capture centers and can trap the photogenerated electrons or holes excited by ultraviolet or visible light. Further oxygen vacancies can effectively restrain the recombination of electron-hole pairs, resulting in improvement of photocatalytic activities[31-32].

Currently, the main morphology is nanoparticles[5,33-35], nanorods[36-37], nanotube[38-39] and nanofiber[40], as well as the other special morphologies. And

the main fabrication methods are hydrothermal with some surfactant and modify agents. For example, ceria with sphere structure possess high oxygen storage ability, high thermal stability[41-42], well conductivity and other electrochemical performance which are attribute to application in Lithium-ion batteries. While, cerium dioxide with nanotube structure exhibits high catalysis ability and oxidation capacity due to its high special surface[43-44].

Herein, we report that a facile and feasible approach to prepare yttrium-doped CeO_2 with hollow sphere structure by hydrothermal technique using the simple inorganic salts $\text{Ce}(\text{NO}_3)_3$ and $\text{Y}(\text{NO}_3)_3$ as original materials and polystyrene as a soft-template. The morphology of as-fabricated samples can be controlled by tuning the reaction temperature and reactant concentration. The photocatalytic performance of these products with different morphology is compared through the systematic experiments of acetaldehyde Photocatalytic oxidation.

2. Experimental section

2.1 Materials

Yttrium nitrate hexahydrate ($\text{Y}(\text{NO}_3)_3 \cdot 6\text{H}_2\text{O}$) and cerium nitrate hexahydrate ($\text{Ce}(\text{NO}_3)_3 \cdot 6\text{H}_2\text{O}$) were of analytical grade and used without any further purification. All of the above original materials were purchased from Wako Co., Ltd. Polystyrene (PS) (230nm) microsphere aqueous solution was prepared in our laboratory which was prepared with normal hydrothermal according with previous report. And the size and surface electrical properties of the microsphere were analysis by the zeta

potential.

2.2 Preparation:

CeO₂ with yttrium-doped with a hollow-sphere structure was fabricated through the traditional hydrothermal process. All original analytical grade materials were used without any further purification. Cerium nitrate (Ce(NO₃)₃·6H₂O) 0.87 g and yttrium nitrate (Y(NO₃)₃·6H₂O) 0.07 g were dissolved in 100 ml of deionized water with vigorous magnetic stirring for 30 minutes at room temperature. The optimum dopant concentration was discussed in the previous studies, so we take the optimal mole ratio value 1:0.1 of Cerium nitrate and yttrium nitrate. Then, 0.5 ml~2 ml polystyrene (PS) (230nm) aqueous solution was added to the aqueous solution. The mixture was stirred continuously for one hour. The mixed solution was then sealed in a Teflon-lined autoclave and heated at 150 °C for 24 hours. After cooling to room temperature, a light yellow precipitate was collected by centrifugation and washed several times with deionized water and ethanol. Target products were obtained after dried in the air at 60 °C for one day. Yttrium doped ceria with hollow structure was obtained by calcination of the as-prepared precursor in air at 400 °C for 4 h.

2.3 Characterizations.

An X-Ray diffractometer (XRD) (Bruker-AXS, D8 sss) with Cu Ka radiation ($\lambda=1.5406\text{\AA}$) and monochromator was used to identify the crystalline phase. The crystallite parameters and size were calculated by the Rietveld method (TOPAS 4.0).

N₂ adsorption and desorption isotherms were recorded at 77 K using a Nova 4200e instrument. The samples were precisely weighted and degased at 373 K for 3 h. The specific surface area was calculated by the 5 points Brunauer-Emmit-Teller theory. Raman analysis (Renishaw, In via) was performed using a 532 nm excitation laser with 5 mW and an air-cooled CCD detector. Raman peak shifts were determined by fitting with the Lorentzian and Gaussian composite function. Morphology and size of as-fabricated products were examined by using a field emission scanning electron microscope (FESEM) (Hitachi, S-4800, 15KV), high-resolution transmission electron

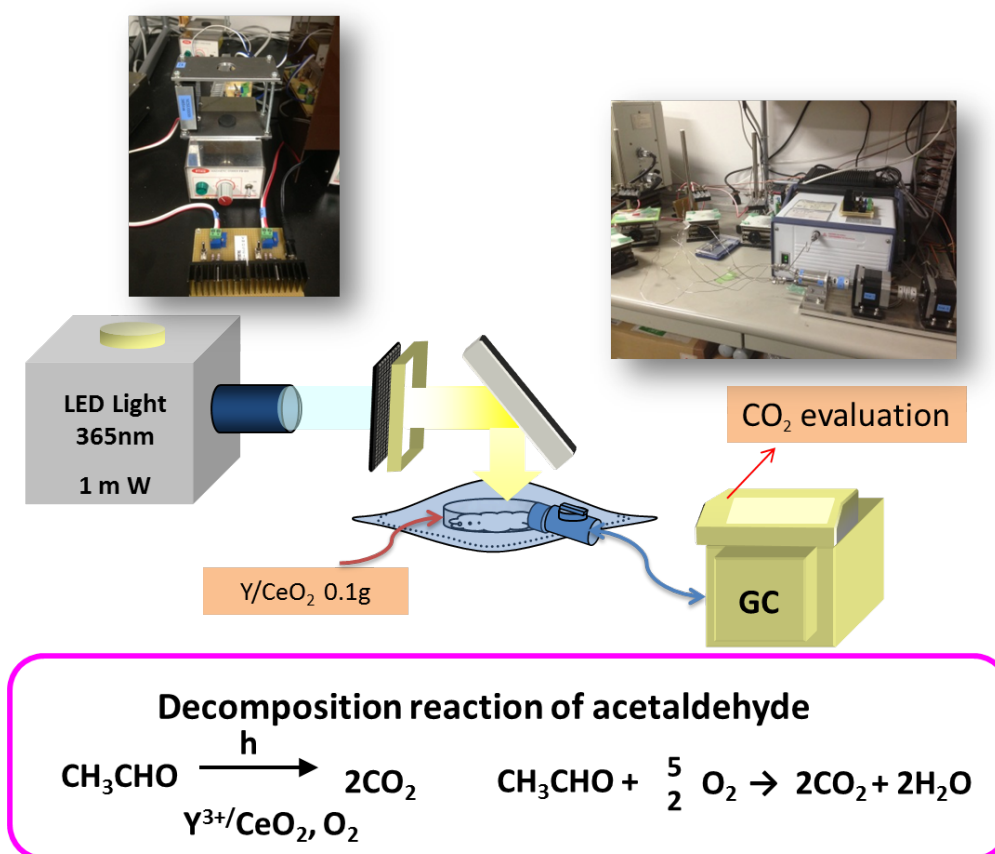


Fig 1: Photocatalytic measurement instrument Schematic diagram

microscope (HRTEM) and HADDF-STEM (FEI, Tecnai G2 F30 S-TWIN, 300KV).

Inductively coupled plasma atomic emission spectrum (ICP-AES) (Shimadzu, ICPS-8000) was used to identify the yttrium's stability in the solution.

2.4 Photocatalytic Evaluations.

UV lighter using black light (UVP, XX-15BLB) can be used in order to remove possible organic materials adsorbed on the surface of samples more than one week before evaluation of photocatalytic activity. The photocatalytic activity of as-fabricated samples was assessed by ability for decomposition of acetaldehyde. And the analytic instruments are show in the Fig 1. Twenty milligrams of powder was spread on the bottom of a glass dish, and the glass dish was placed in a Tedlar bag (AS ONE Co. Ltd.). Five hundred ppm of acetaldehyde was injected into the bag together with 125 cm³ of artificial air. Then the bag, which was fabricated above, was put into a dark place at room temperature for 2 hours for the purpose of reaching an adsorption equilibrium. A light-emitting diode (LED; Epitex, L365), which emitted light at wavelengths of ca. 365 nm, was used as a light source, and its intensity was controlled at 0.9 mW cm⁻². The concentration of generated CO₂ as a function of irradiation time was monitored by a gas chromatography (Shimadzu GC-8A, FID detector) equipped with a Porapak N-packed column and a methanizer (GL Science, MT-221).

3.Results and discussion:

3.1 morphology characterization

Fig. 2 and Fig. 3 show panoramic FE-SEM images and HR-TEM of fabricated particles. It can be seen that the particles are uniform octahedral particles with diameters of approximately 200 nm (Fig. 2(a)). The lattice spacing of the parallel fringes is 0.313 nm, corresponding to the (111) plane of FCC CeO_2 (inset image of Fig. 3(a)). After yttrium doping, morphology of products did not change obviously and octahedral structure and monodispersity are well maintained (Fig. 2(b)).

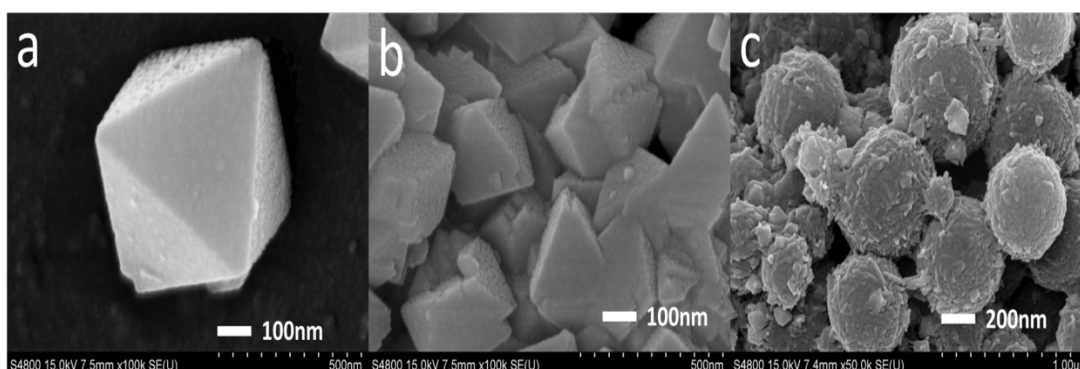


Fig 2. FE-SEM images of the products (a) pure CeO_2 with octahedral structure, (b) yttrium doped CeO_2 with octahedral structure and (c) yttrium doped CeO_2 with sphere structure

The exposed crystal plane is still (111). In addition, the composition of elements and distribution of the as-fabricated products obtained under different experimental conditions were analyzed by STEM-HAADF images and EDS mapping images. Fig. 4 image shows the existence of not only cerium but also yttrium, with yttrium ions being dispersed evenly on the CeO_2 octahedral structure surface and in the bulk. Herein we can draw a conclusion that yttrium enters the lattice and dopes the parts of cerium successfully. The results for composition of elements and distribution are well consistent with the results of the XRD and Raman analysis. Fig. 2 (c) shows that, through adding PS sphere, morphology of products are sphere structure with

diameters of approximately 400 nm. Fig. 3(c) shows that octahedral CeO_2 particles covered PS sphere surface through electrostatic adsorption. Compared with pure CeO_2

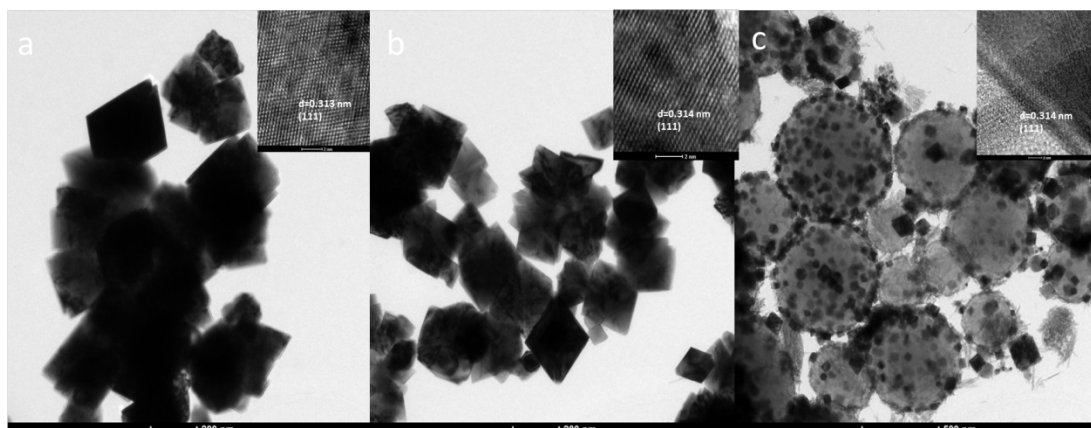


Fig. 3 HR-SEM images of the products (a) pure CeO_2 with octahedral structure, (b) yttrium doped CeO_2 with octahedral structure and (c) yttrium doped CeO_2 with sphere structure

or yttrium doped CeO_2 , the diameter of these particles covered surface are smaller. Separate yttrium-doped CeO_2 particles scarcely observed from the image, illustrated that cerium oxide precursor nucleated and growth on the PS microsphere surface instead of in the aqueous solution. Meanwhile EDS mapping images (see the Fig.4) shows not only yttrium and cerium but also carbon can be detected, and yttrium and cerium elements are well distributed on the surface of PS.

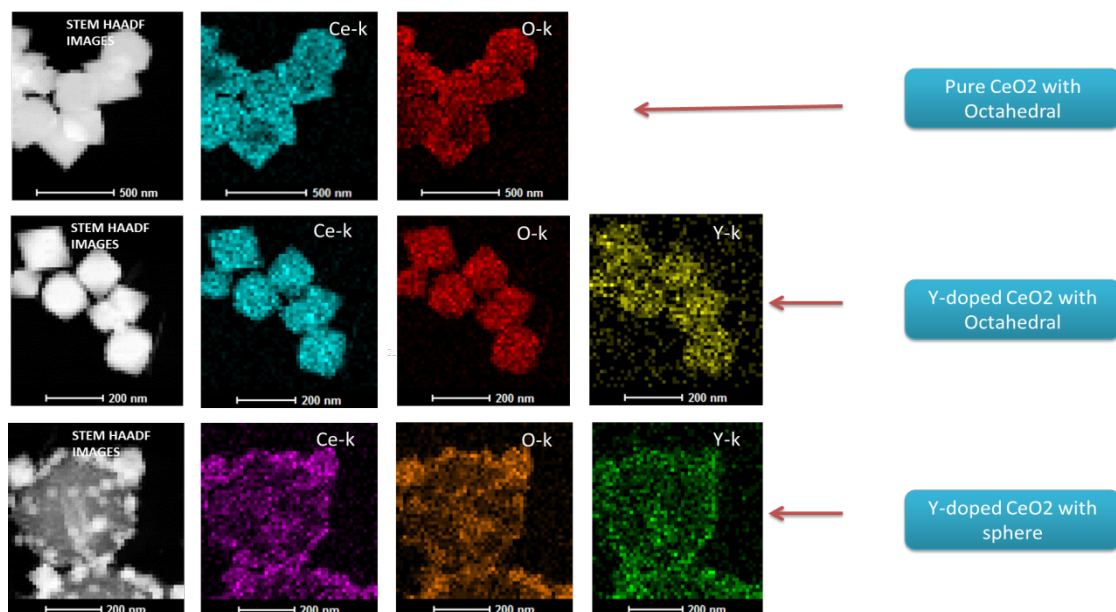


Fig.4 HAADF images and distribution of element maps of the products before and after doped with different morphology.

3.2 Structure characterization

Typical X-ray diffractometer (XRD) patterns of samples obtained under different conditions are shown in Fig. 5. Characteristic peaks at 28.5, 33.0 47.4 and 56.3 2θ are attributed to pure cerium oxide with a cubic fluorite structure (JCPDS No. 34-0394) and are assigned to the crystal planes (111), (200), (220) and (311), respectively.. The sharp diffraction peaks from all samples suggest a high degree of crystallinity of fabricated samples, and no impurity peaks appeared. The relative intensity of each peak does not change, suggesting that there is no preferred orientation. The elaborated XRD pattern of the highest peak reveals that, compared with pure ceria, the highest peak position (111) of the products exhibited an obvious shift to a lower angle after yttrium doping and reached about 28.43⁰ (2θ), indicating that crystal lattice has expanded conspicuously due to the entry of yttrium into the crystal structure. At the same time, PS amorphous peak around 20⁰ (2θ) can be

detected from the diffraction pattern of yttrium doped ceria/ps. Rietveld refinements were also carried out according to the diffraction lines by varying parameters in order to investigate the actual doping quantity and location (Fig. 6). As we known that each cerium is arranged in the face-centered cubic surrounded by eight oxygen elements in the cubic fluorite structure of cerium dioxide. Meanwhile, oxygen elements occupied all of the tetrahedral positions and each oxygen element has four ligancy of cerium cations. When the amount of the dopant was changed without changing the other experimental conditions, there were significant changes in the lattice parameters. The lattice parameter value (a) changed to 5.4221 Å. It can be clearly seen that the lattice parameter value (a) after doping is larger than the bulk CeO₂ lattice parameter value a=5.4178 Å even though the space group is still Fm-3m before and after doping. This indicates that yttrium has partially substituted cerium ions and has been introduced into the interior lattice, maintaining the ceria cubic fluorite structure instead of forming Y₂O₃-CeO₂ composite.

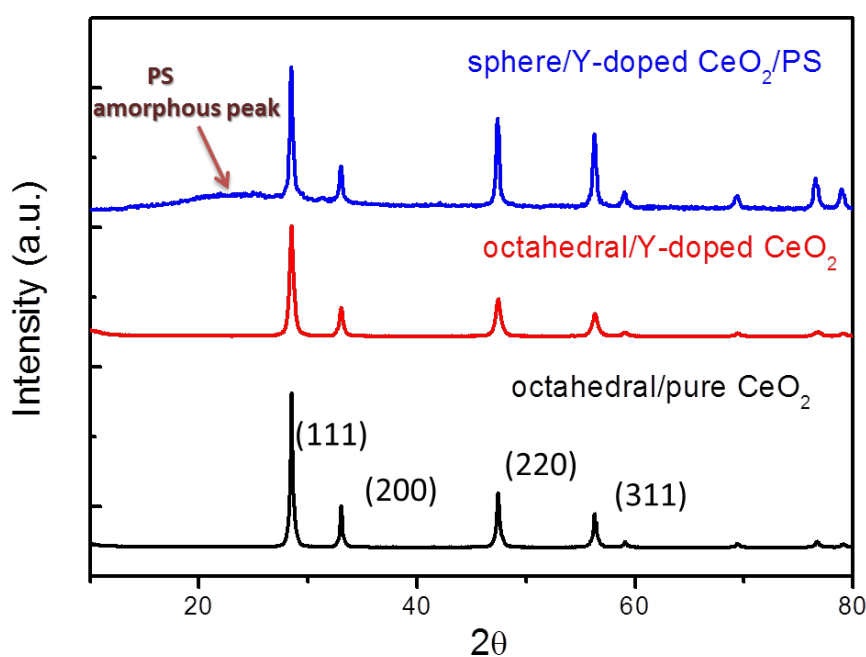


Fig. 5 XRD pattern of as-fabricated samples

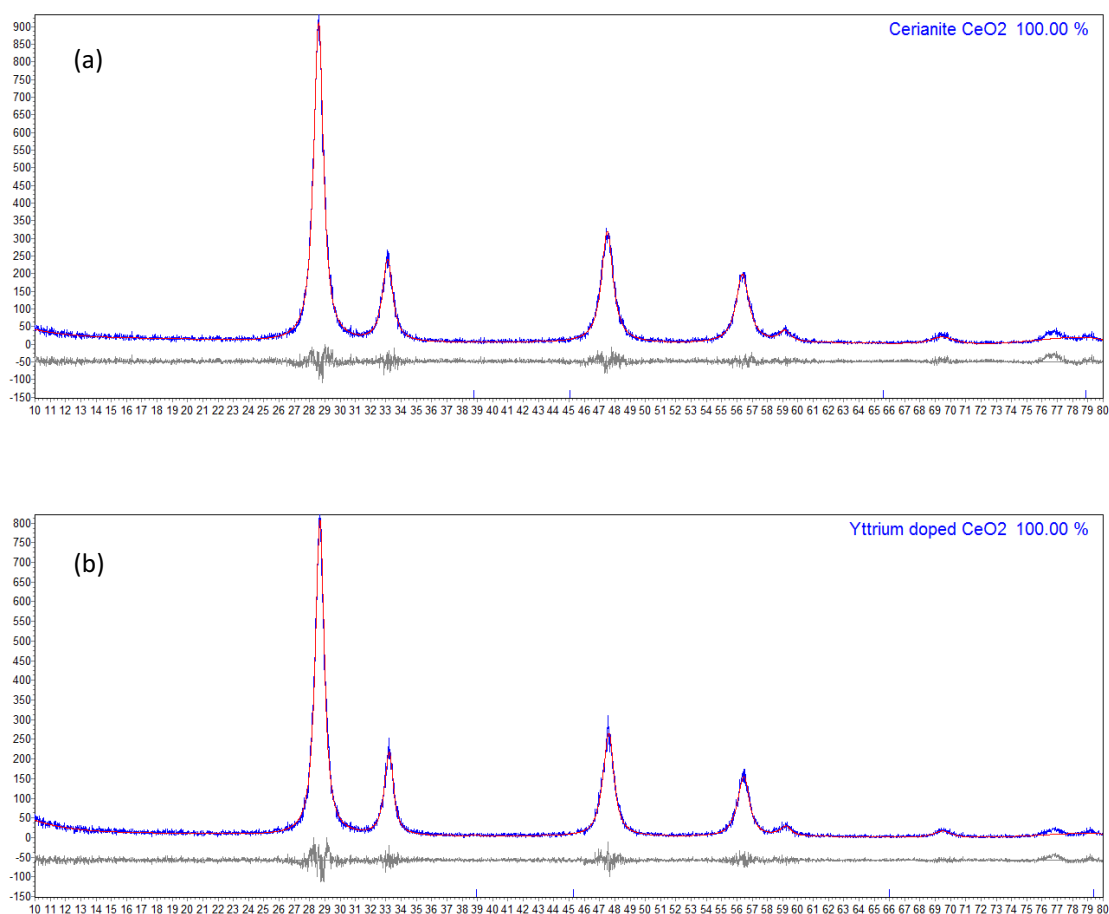


Fig. 6 Ritevld refined spectral of products (a)before doped and (b)after doped

Raman spectra of as-fabricated samples under various experimental conditions are shown in Fig. 7. A strong Raman shift at $\sim 460\text{ cm}^{-1}$ and a relatively weak shift at $\sim 610\text{ cm}^{-1}$ can be detected. The shift at $\sim 460\text{ cm}^{-1}$ can be assigned to F_{2g} vibration of the fluorite-type structure and it can be considered as the symmetric stretching mode of oxygen atoms around cerium ions, and the molecule retains its tetrahedral symmetry throughout. Based on the results of previous studies and our own studies, a weak and less prominent band near $\sim 600\text{ cm}^{-1}$ can be attributed to a nondegenerate

longitudinal optical mode caused by a local Ce-O ($R_{\text{Ce-O}}$) bond symmetry stretch. According to previous reports that not all cerium ions show Ce^{4+} chemical valence in the lattice; small cerium ions show Ce^{3+} tervalence. In order to maintain the particles in an electrically neutral state, the lattice oxygen would escape from the structure and finally result in the formation of intrinsic oxygen vacancies. Oxygen vacancies perturb the local Ce-O bond symmetry. A new and weak Raman shift at $\sim 530 \text{ cm}^{-1}$, which cannot be detected in Raman spectra of pure CeO_2 , can be detected. It is attributed to extrinsic oxygen vacancies caused by doping. As a dopant, yttrium enters the cubic fluorite lattice of CeO_2 and substituted cerium. In order to maintain electronic neutrality, doping cations showing different valence states with Ce^{4+} and part of the oxygen would also escape from lattice to form extrinsic oxygen vacancies.

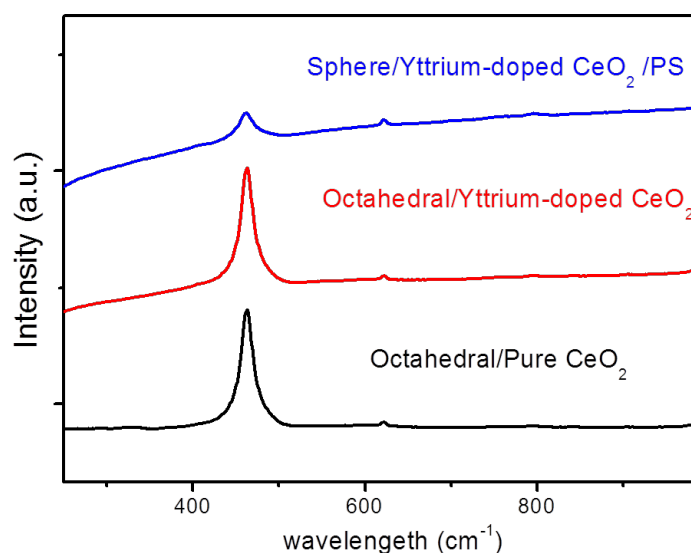


Fig. 7 Raman spectra of as-fabricated samples

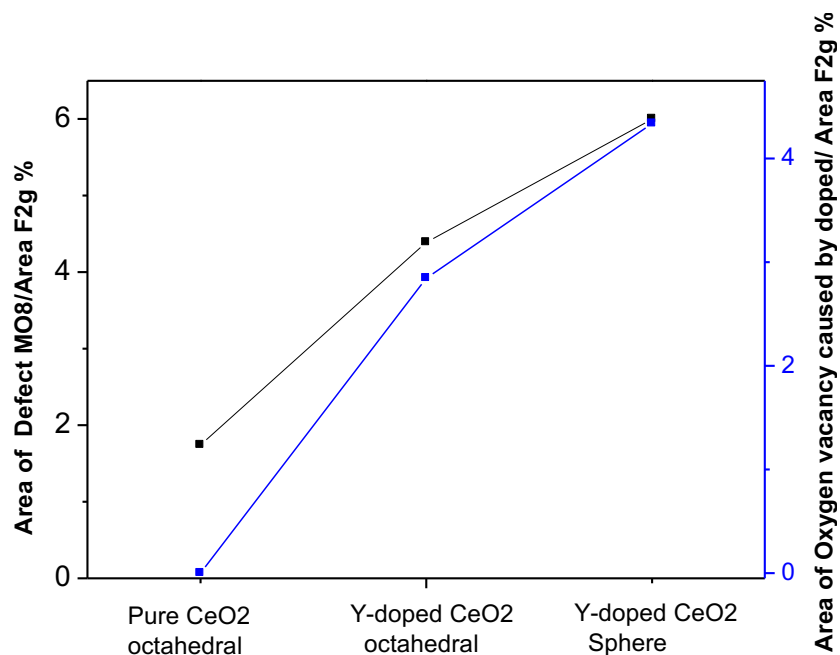


Fig. 8 calculate oxygen vacancies of as-fabricated samples from the Raman spectral

From the Fig. 8 we can see that yttrium doped ceria with sphere structure possess higher oxygen vacancy than doped ceria with octahedral structure and without doped. So, we can predict that yttrium doped ceria with sphere structure should have higher photocatalytic activities because high concentration of oxygen vacancy provide high activity spot and improve the ability of restrict recombination of photon-generated electrons and holes.

3.3 X-ray photoelectron spectroscopy characterization

XPS characterization was applied to determine the CeO₂ nanoparticles before and after yttrium doping. Wide scanning XPS spectra of the product is illustrated in Fig. 9. The elements Ce, O, and C can be detected from Fig. 9(a), and they are assigned to Ce3d, O1s and C1s binding energies, respectively. Not only above

elements but also yttrium element can be detected from the spectra, and it is assigned to Y3d binding energy, indicating that doping was successful (Fig. 9(b)). The elaborated Y3d XPS spectra of the products after doping are shown in Fig. 10. After deconvolution and separation, two peaks located at 156.1ev and 158.2ev, assigned to Y3d5/2 binding energy, can be founded from XPS profiles.

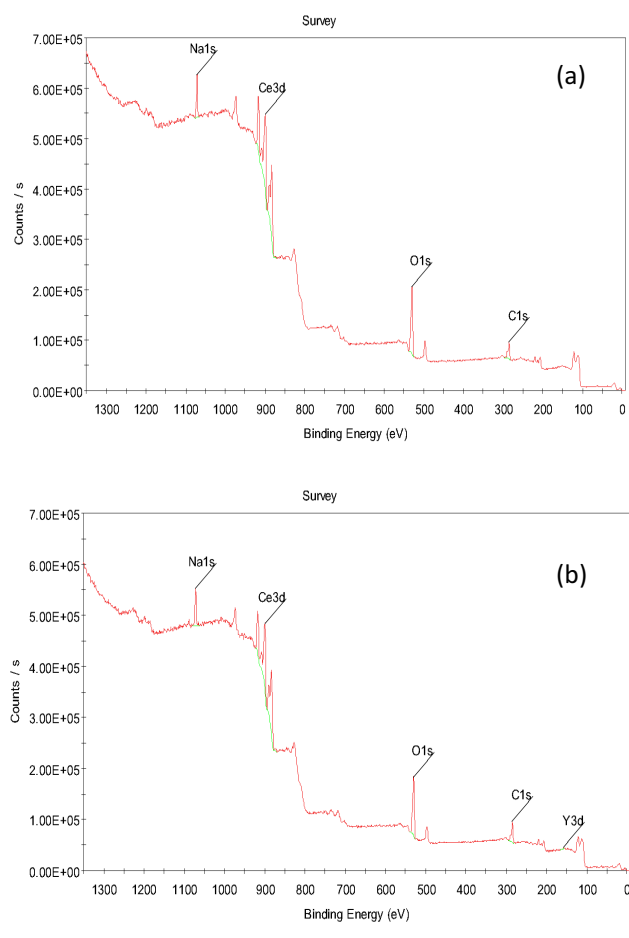


Fig. 10: Wide scanning XPS spectra of products (a) before doping and (b) after doping.

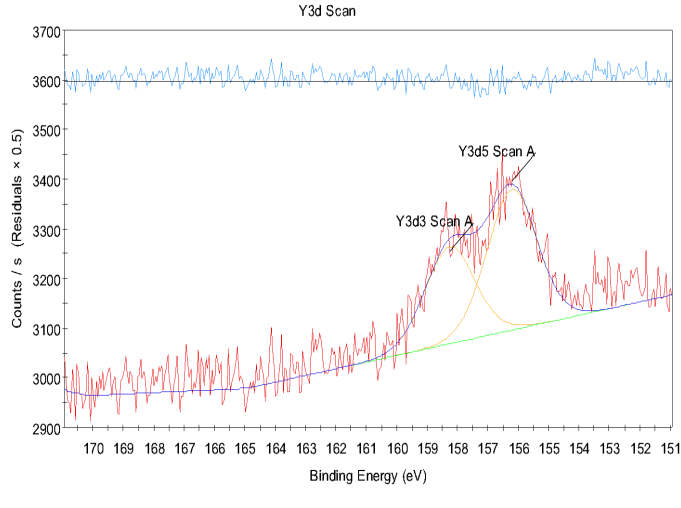


Fig. 10: High-resolution XPS spectra of Y3d separated peak curve

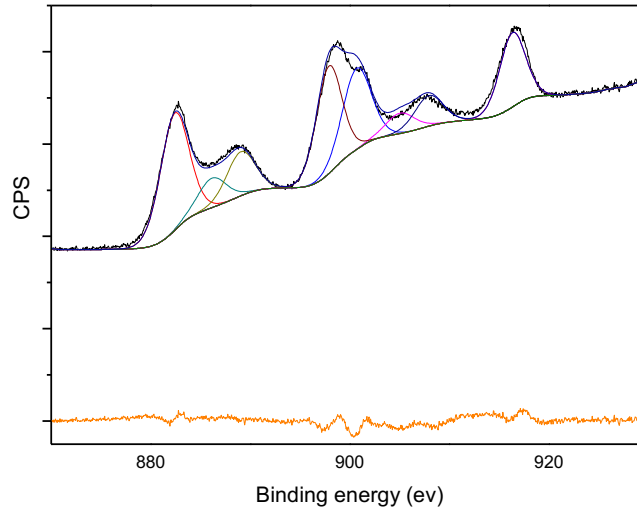


Fig. 11: High-resolution XPS spectra of Ce3d separated peak curve

Fig. 11 shows Ce 3d electron core level XPS spectra for as-fabricated samples and the changes in Ce 3d_{3/2} and Ce 3d_{5/2} components depending on the Ce³⁺ and Ce⁴⁺ oxidation states. Five pairs of doublets, (u, v), (u₁, v₁), (u₂, v₂), (u₃, v₃) and (u₀, v₀), can be decomposed from the origin region, where u and v come from Ce 3d_{3/2} and Ce 3d_{5/2} states, respectively. We observed that (u, v), (u₂, v₂) and (u₃, v₃), which were attributed to Ce 3d₉ 4f₂ O 2p₄, Ce 3d₉ 4f₁ O 2p₅ and Ce 3d₉ 4f₀ O 2p₆ final states, respectively, all belonged to the Ce⁴⁺ oxidation state. The two pairs doublets as (u₁, v₁) and (u₀, v₀) originated from the Ce 3d₉ 4f₁ O 2p₄ and Ce 3d₉ 4f₁ O 2p₅

final states, respectively, which correspond to the Ce^{3+} oxidation state. The relative amount of cerium in the trivalent oxidation state can be calculated from equation (2):

$$\frac{[Ce^{3+}]}{[Ce^{3+}+Ce^{4+}]} = \frac{\text{area}(V_0, V_1, U_0, U_1)}{\text{total area}}. \quad (2)$$

The fitting data demonstrated that the as-fabricated samples exhibit variation of $[Ce^{3+}]$ concentration. The $[Ce^{3+}]$ concentration after doping was larger than that without doping.

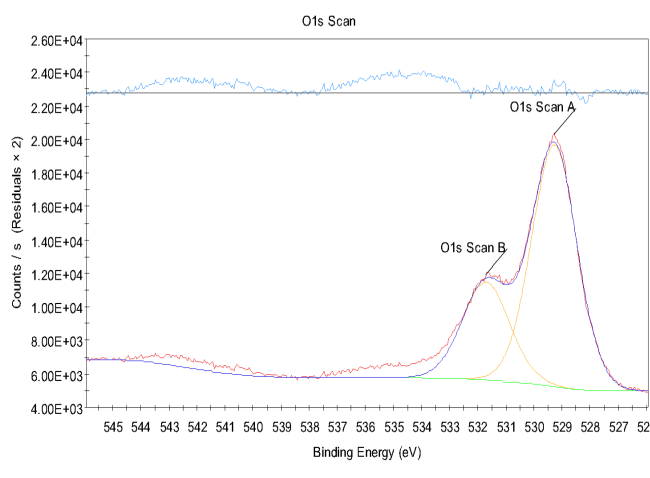


Fig. 12: High-resolution XPS spectra of O1s separated peak curve .

Fig. 12 shows O1s electron core level XPS spectra. One peak around 529.0 eV with a shoulder around 531.5 eV can be clearly seen, and they can be attributed to lattice oxygen (O_{lat}) and surface active oxygen (O_{sur}), respectively. After doping, the O_{lat} and O_{sur} binding energy obviously shifted to a high energy, while the effects on O_{lat} and O_{sur} are different. The O_{sur} 's binding energy value shows a change of 0.8 eV. However, the O_{lat} 's binding energy value shows a change of 0.2 eV only. Therefore, doping of yttrium mainly affects the ceria's surface oxygen binding energy, improving the surface oxygen binding energy and enhancing the activity of surface oxygen. After

deconvolution and multiple-peak separation, we could obtain the surface oxygen ratio from the equation (3):

$$\frac{[O_{\text{sur}}]}{[O_{\text{sur}}+O_{\text{lat}}]} = \frac{\text{area}(O_{\text{sur}})}{\text{total area}} \quad (3)$$

The $[O_{\text{sur}}]$ concentration after doping is larger than that without doping, and the maximum value of surface oxygen ratio is approximately 40.6%. The $[Ce^{3+}]$ and $[O_{\text{sur}}]$ concentrations value of the products can directly reflect the amount and active of oxygen vacancies and suggest that yttrium-doped CeO_2 with a hollow structure should have higher catalytic activity.

3.4. Photocatalytic activity for acetaldehyde decomposition:

The photocatalytic activities of the prepared samples were evaluated by CO_2 liberation from photocatalytic degradation of acetaldehyde. Fig. 13 shows liberation from acetaldehyde decomposition of as-fabricated samples. Compared with pure CeO_2 , the amount and liberation rate are significantly improved after yttrium doped, illustrating photocatalytic activities were enhanced. These results are attributed to that more oxygen vacancies and trivalent cerium produced in order to keep the balance of chemical valence are settled in the ceria crystal structure. The higher concentration of oxygen vacancies and trivalent cerium, the higher photocatalytic activities of products.

At the same time, Fig.13 shows that yttrium doped CeO_2 with different morphology exhibit different photocatalytic activities. Yttrium doped CeO_2 with a sphere structure possess higher photocatalytic activities than CeO_2 with octahedral structure, attributed to that small particles were fabricated in spherical structure and

higher specific surface area obtained. Therefore, yttrium doped CeO₂ with spherical structure exhibit higher photocatalytic activities than ceria with other traditional 1D or 2D structure.

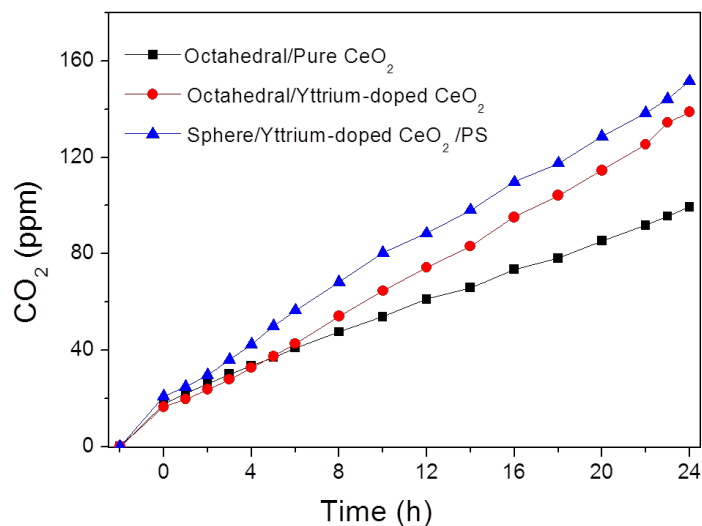


Fig. 13 Time course of CO₂ liberation from acetaldehyde decomposition of as-fabricated samples.

4. Conclusion:

Yttrium doped CeO₂ with hollow sphere hierarchical structure was successfully prepared by a simple hydrothermal method with PS as soft template. The method of synthetic is effective and reproducible and can be expanded to fabrication of other rare-earth-doped morphology-controlled inorganic nanoparticle materials. High-resolution TEM showed that yttrium-doped CeO₂ with hollow sphere hierarchical structure is comprised of many small particles with a crystallite size of 50 nm covered on the surface of PS microsphere. The present work showed that yttrium-doped CeO₂ with sphere structure exhibits an advantage of photocatalytic activity. The trend for changes in photocatalytic activity was explained by the oxygen vacancies and surface active oxygen species derived from changing yttrium doping.

Compared with octahedral structure CeO₂ with yttrium-doped CeO₂ or without doped, y-doped CeO₂ with sphere structure exhibits an advantage of photocatalytic activity, attribute to its higher specific surface area and smaller particle size. The existence of the dopant yttrium provides a higher concentration of oxygen vacancy, and can also improve photocatalytic activities of products.

Reference:

- [1] C.-Y. Cao, Z.-M. Cui, C.-Q. Chen, W.-G. Song, W. Cai, *The Journal of Physical Chemistry C* 114 (2010) 9865-9870.
- [2] Y. Chen, T. Liu, C. Chen, W. Guo, R. Sun, S. Lv, M. Saito, S. Tsukimoto, Z. Wang, *Ceramics International* 39 (2013) 6607-6610.
- [3] F. Dang, K. Kato, H. Imai, S. Wada, H. Haneda, M. Kuwabara, *Crystal Growth & Design* 10 (2010) 4537-4541.
- [4] H. Imagawa, A. Suda, K. Yamamura, S. Sun, *The Journal of Physical Chemistry C* 115 (2011) 1740-1745.
- [5] G.-R. Li, D.-L. Qu, L. Arurault, Y.-X. Tong, *The Journal of Physical Chemistry C* 113 (2009) 1235-1241.
- [6] L. Li, H.K. Yang, B.K. Moon, Z. Fu, C. Guo, J.H. Jeong, S.S. Yi, K. Jang, H.S. Lee, *The Journal of Physical Chemistry C* 113 (2008) 610-617.
- [7] M. Lin, Z.Y. Fu, H.R. Tan, J.P.Y. Tan, S.C. Ng, E. Teo, *Crystal Growth & Design* 12 (2012) 3296-3303.
- [8] T. Mokkelbost, I. Kaus, T. Grande, M.-A. Einarsrud, *Chemistry of Materials* 16

(2004) 5489-5494.

[9] C. Paun, O.V. Safonova, J. Szlachetko, P.M. Abdala, M. Nachtegaal, J. Sa, E. Kleymenov, A. Cervellino, F. Krumeich, J.A. van Bokhoven, *The Journal of Physical Chemistry C* 116 (2012) 7312-7317.

[10] J.C. Qian, F. Chen, F. Wang, X.B. Zhao, Z.G. Chen, *Materials Research Bulletin* 47 (2012) 1845-1848.

[11] W. Shan, H. Guo, C. Liu, X. Wang, *Journal of Rare Earths* 30 (2012) 665-669.

[12] G. Shen, Q. Wang, Z. Wang, Y. Chen, *Materials Letters* 65 (2011) 1211-1214.

[13] Z. Wang, Z. Quan, J. Lin, *Inorganic Chemistry* 46 (2007) 5237-5242.

[14] Z.-L. Wang, G.-R. Li, Y.-N. Ou, Z.-P. Feng, D.-L. Qu, Y.-X. Tong, *The Journal of Physical Chemistry C* 115 (2010) 351-356.

[15] Q. Wu, F. Zhang, P. Xiao, H. Tao, X. Wang, Z. Hu, Y. Lü, *The Journal of Physical Chemistry C* 112 (2008) 17076-17080.

[16] J. Xu, J. Harmer, G. Li, T. Chapman, P. Collier, S. Longworth, S.C. Tsang, *Chemical communications* 46 (2010) 1887-1889.

[17] L. Yan, R. Yu, J. Chen, X. Xing, *Crystal Growth & Design* 8 (2008) 1474-1477.

[18] S. Yang, L. Gao, *Journal of the American Chemical Society* 128 (2006) 9330-9331.

[19] R. Yu, L. Yan, P. Zheng, J. Chen, X. Xing, *The Journal of Physical Chemistry C* 112 (2008) 19896-19900.

[20] D. Zhang, H. Fu, L. Shi, C. Pan, Q. Li, Y. Chu, W. Yu, *Inorganic Chemistry* 46 (2007) 2446-2451.

- [21] R.B. Rakhi, W. Chen, D. Cha, H.N. Alshareef, *Nano letters* 12 (2012) 2559-2567.
- [22] F. Wang, H. Dai, J. Deng, G. Bai, K. Ji, Y. Liu, *Environ Sci Technol* 46 (2012) 4034-4041.
- [23] L. Wang, L.-F. Zhang, S.-L. Zhong, A.-W. Xu, *Applied Surface Science* 263 (2012) 769-776.
- [24] H. Wu, L. Wang, *Catalysis Communications* 12 (2011) 1374-1379.
- [25] Z. Wu, M. Li, S.H. Overbury, *Journal of Catalysis* 285 (2012) 61-73.
- [26] D.-E. Zhang, X.-M. Ni, H.-G. Zheng, X.-J. Zhang, J.-M. Song, *Solid State Sciences* 8 (2006) 1290-1293.
- [27] F. Zhou, X. Ni, Y. Zhang, H. Zheng, *Journal of colloid and interface science* 307 (2007) 135-138.
- [28] K. Zhou, X. Wang, X. Sun, Q. Peng, Y. Li, *Journal of Catalysis* 229 (2005) 206-212.
- [29] H. Hojo, T. Mizoguchi, H. Ohta, S.D. Findlay, N. Shibata, T. Yamamoto, Y. Ikuhara, *Nano letters* 10 (2010) 4668-4672.
- [30] R. Kostić, S. Aškrabić, Z. Dohčević-Mitrović, Z.V. Popović, *Applied Physics A* 90 (2007) 679-683.
- [31] Y. Lee, G. He, A.J. Akey, R. Si, M. Flytzani-Stephanopoulos, I.P. Herman, *Journal of the American Chemical Society* 133 (2011) 12952-12955.
- [32] D.R. Mullins, P.M. Albrecht, T.-L. Chen, F.C. Calaza, M.D. Biegalski, H.M. Christen, S.H. Overbury, *The Journal of Physical Chemistry C* 116 (2012) 19419-19428.

- [33]Z. Wu, M. Li, J. Howe, H.M. Meyer, 3rd, S.H. Overbury, Langmuir : the ACS journal of surfaces and colloids 26 (2010) 16595-16606.
- [34]S.C. Yan, Z.S. Li, Z.G. Zou, Langmuir : the ACS journal of surfaces and colloids 26 (2010) 3894-3901.
- [35]F. Zhang, Journal of Applied Physics 95 (2004) 4319.
- [36]Y. Ma, X. Wang, S. Li, M.S. Toprak, B. Zhu, M. Muhammed, Advanced materials 22 (2010) 1640-1644.
- [37]R. Srinivasan, A. Chandra Bose, Materials Letters 64 (2010) 1954-1956.
- [38]N. Wetchakun, S. Chaiwichain, B. Inceesungvorn, K. Pingmuang, S. Phanichphant, A.I. Minett, J. Chen, ACS applied materials & interfaces (2012).
- [39]S. Yang, Y. Guo, H. Chang, L. Ma, Y. Peng, Z. Qu, N. Yan, C. Wang, J. Li, Applied Catalysis B: Environmental 136-137 (2013) 19-28.
- [40]Z.-X. Li, L.-L. Li, Q. Yuan, W. Feng, J. Xu, L.-D. Sun, W.-G. Song, C.-H. Yan, The Journal of Physical Chemistry C 112 (2008) 18405-18411.
- [41]M. Machida, Y. Murata, K. Kishikawa, D. Zhang, K. Ikeue, Chemistry of Materials 20 (2008) 4489-4494.
- [42]E.W. McFarland, H. Metiu, Chemical Reviews (2013).
- [43]H. Xie, Y. Li, S. Jin, J. Han, X. Zhao, The Journal of Physical Chemistry C 114 (2010) 9706-9712.
- [44]H. Zhang, X. He, Z. Zhang, P. Zhang, Y. Li, Y. Ma, Y. Kuang, Y. Zhao, Z. Chai, Environmental Science & Technology 45 (2011) 3725-3730.

General Conclusion:

A broom-like porous CeO₂ hierarchical architecture was successfully prepared by a simple hydrothermal method. The Ostwald ripening theory could explain the morphology evolution process. The optimum reaction time and temperature for the synthesis of porous broom-like CeO₂ was found to be 39 hours and 120 °C, respectively.

CeO₂ with an yttrium-doped porous broom-like hierarchical architecture was successfully prepared by a simple hydrothermal method. The method of synthetic is effective and reproducible and can be expanded to fabrication of other rare-earth-doped morphology-controlled inorganic nanoparticle materials. The optimum doping concentration for products were found to be amole ratio of Ce(NO₃)₃ and Y(NO₃)₃ of 1:0.1. High-resolution TEM showed that yttrium-doped CeO₂ with a broom-like shape is comprised of many small particles with a crystallite size of 10 nm and porous construction can be discovered among the small particles. The present work showed that porous broom-like yttrium-doped CeO₂ exhibits an advantage of photocatalytic activity. The trend for changes in photocatalytic activity was explained by the oxygen vacancies and surface active oxygen species derived from changing yttrium doping.

CeO₂ with yttrium-doped hedgehog-like hierarchical architectures was prepared successfully by a simple hydrothermal method. The optimum experimental conditions for synthesis of octahedral plus nanorod CeO₂ were found to be 0.47 mM Na₃PO₄ and 0.747 mmol Y(NO₃)₃ as original materials and reaction at 200 °C for 24 hours.

Hedgehog-like yttrium-doped CeO₂ exhibits an advantage of photocatalytic activity. The trend for changes in photocatalytic activities was explained by the oxygen vacancies derived from changes in morphology and yttrium doping.

Yttrium-doped CeO₂ with sphere architectures was prepared successfully by a simple hydrothermal method utilizing PS as a soft template. Compared with octahedral structure CeO₂ with yttrium-doped CeO₂ or without doped, y-doped CeO₂ with sphere structure exhibits an advantage of photocatalytic activity, attribute to its higher specific surface area and smaller particle size. The existence of the dopant yttrium provides a higher concentration of oxygen vacancy, and can also improve photocatalytic activities of products.

List of publication

Morphology control and characterization of broom-like porous CeO₂.

[Bin Xu](#), Qitao Zhang, Saisai Yuan, Ming Zhang, Teruhisa Ohno

Chemical Engineering Journal, Vol.260, PP.126-132.

Morphology control and photocatalytic characterization of yttrium-doped hedgehog-like CeO₂.

[Bin Xu](#), Qitao Zhang, Saisai Yuan, Ming Zhang, Teruhisa Ohno

Applied Catalysis B: Environmental, Vol.164, PP.120-127.

Synthesis and Photocatalytic Performance of Yttrium-doped CeO₂ with a Porous Broom-like Hierarchical Structure

[Bin Xu](#), Qitao Zhang, Saisai Yuan, Ming Zhang, Teruhisa Ohno

Applied Catalysis B: Environmental, Vol.183, PP.361-370.

Methods for Determining Relative Crystallinity of Plant Starch X-ray Powder Diffraction Spectra.

[Bin Xu](#), Jianming Man, Cunxu Wei

Chinese Bulletin of Botany, Vol. 47, PP.278-285

Acknowledgements:

The present thesis is the summary of the results of the author's work during 2013-2016. And now please let me express my thanks to all those people who have supported and encouraged me throughout the course of my study.

First of all, I would like to express my sincere gratitude to my advisors Professor Teruhisa Ohno and Professor Ming Zhang (YangZhou University, China) for their valuable advice, guidance and support throughout my research work. I feel very fortunate to have learned all that I have from them. The research work done under them is one of the most important and formative experiences of my life and I am forever indebted to them for that. Special thanks are also given to Professor Naoya Murakami, Associate Professor Sunao Kamimura (Kyushu Institute of Technology, Japan), Professor Aiping Zhu, Professor Defeng Wu, Associate Professor Changhao Yan and Junliang Liu (YangZhou University, China) for their valuable suggestion and helpful advice. Special thanks go to Dr. Qitao Zhang, Dr. Saisai Yuan and Dr. Zhengyuan Jin for their valuable suggestions at every stage of my work. I would also like to express my gratitude to Dr. Shuhei Yamada and Dr. Zhiguo Ma for their technical help.

Next, I am grateful to all my friends at Kyushu Institute of Technology and YangZhou University for giving me some of the most memorable experiences of my life. Names that I have left out, you all are not forgotten, your encouragements and faith has enlighten me through the goodtimes and the bad and has helped me to pull on when I was lost and pondering for adirection.

Finally I would like to express my deepest gratitude to my wife Mrs. Dongmei Tian, my daughter princess CICI and my parents for their love, support and encouragement throughout my life.

Bin Xu

January 2016